Role of polythiophene- based interlayers from electrochemical processes on organic light-emitting diodes

DISSERTATION

zur Erlangung des akademischen Grades

**Doctor rerum naturalium
(Dr. rer. nat.)**

vorgelegt

der Fakultät Mathematik und Naturwissenschaften
der Technischen Universität Dresden

von

M.S.   Zhang,   Fapei

geboren am 24.07.1969 in Anhui, P. R. China

Gutachter: 1. Prof. Dr. Jörg Fink

2. Prof. Dr. Waldfried Plieth

3. Prof. Dr. Wolfgang Brütting

Eingereicht am: 11.09.2003

Tag der Verteidigung: 22.01.2004

Contents

5. Electrochemical treatment of PEDT:PSS for OLED

6. Summary and outlook

List of the publication in this work

Acknowledgement

1. Overview and motivation

Electroluminescence (EL), the generation of light by electrical excitation, has been found in a wide range of semiconductors. Conventional EL devices are made of inorganic direct-band gap semiconductors such as GaAs and InGaAs, which have been commercialized for more than 40 years. For organic semiconductors, the EL was first demonstrated on anthracene crystal in 1960s[1, 2]. However, due to the high operating voltage (> 100 V) and the low efficiency, such EL devices did not attract much attention. The breakthrough was made by the work of Tang and van Slyke at Kodak[3], who found efficient electroluminescence in two-layer sublimed molecular film devices. EL had also been reported on single-layer conjugated polymer PPV by Burroghes *et al.* at Cambridge University[4]. Since then, a large number of other molecular and polymeric materials were used to prepare such light emitting diodes (LED), and much activity and progress has been made in the development of organic LEDs from both academia and industry in the past 15 years. In this chapter, the author will give a brief introduction into the structure and physics of organic LEDs, as well as the activities on the enhancement of device performance.

1.1 Device structure and materials

The basic structure of organic LED is simple (see Fig. 1.1): A sequence of organic layers is deposited between two electrodes, an anode for hole and a cathode for electron injection, respectively. One of the electrodes is transparent to allow the generated light to leave the
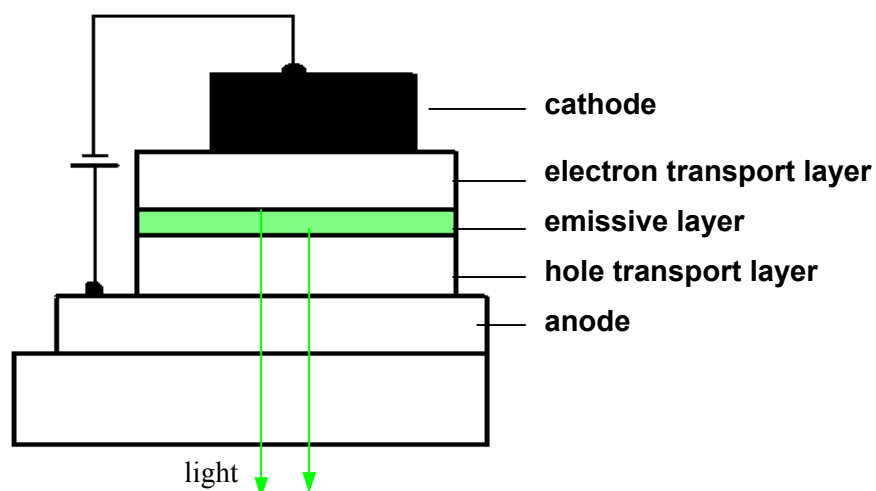
Fig. 1.1. Schematic structure of an organic LED.

device. Under a sufficient forward bias, holes are injected from the anode and electrons from the cathode into organic layer. The charge carriers travel in the applied field until they meet in the emissive layer and form the excitons (neutral excited state). The excitons can decay radiatively which results in photon emission. The thickness of organic layers ranges from several tens of nanometers to 200 nm.
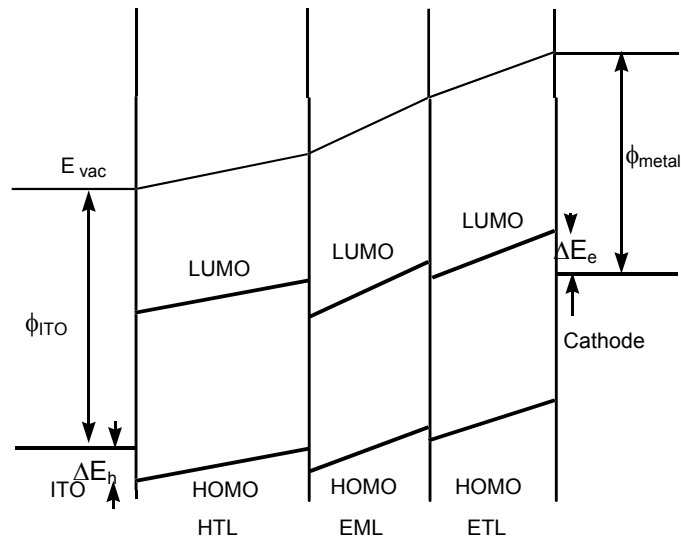
Fig. 1.2. Schematic energy level diagram of an OLED under forward bias. Also shown are the work function of ITO and cathode (ϕ_{ITO} and ϕ_{metal}) and the barriers for injection of holes (ΔE_h) and electrons (ΔE_e). (HTL: hole transport layer, ETL: electron transport layer, EML: emissive layer, and HOMO: highest occupied molecular orbital, LUMO: lowest unoccupied molecular orbital).

In order to achieve a high performance, the organic layer should fulfil certain requirements. The hole transport layer (HTL) should have a high hole mobility. Its energetic level of the highest occupied molecular orbital (HOMO) has to be relatively low to reduce the energy barrier to hole injection (ΔE_h, shown in Fig. 1.2). Furthermore, the HTL should hinder electrons coming from the cathode from reaching the anode. The properties of the electron transport layer (ETL) should be complementary to those of the HTL (i.e. high lowest unoccupied molecular orbital (LUMO) level and high electron mobility). The anode should have a high work function (ϕ) to ease the hole injection into the HOMO of the HTL. Indium-tin oxide (ITO) has a relatively high ϕ and excellent transparency for visible light and thus is suitable for the use as anode. Accordingly, the cathode should be a low work function metal like magnesium or calcium. For the emissive layer, the HOMO and LUMO should allow hole and electron to be injected from neighboring layers. Additionally, the photoluminescence (PL) quantum efficiency (corresponding to the ratio of radiative recombinating excitons to created

singlet excitons) should be high. The schematic energy level under forward bias is shown in Fig. 1.2.

Since some organic materials can combine several of the properties mentioned above in one layer, fewer layers are used in most of OLEDs. In typical Kodak-type (i.e. a combination of molecular HTL and ETL) bilayer OLED of ITO/NPB/Alq$_3$/Mg:Ag[3], NPB serves as a hole transport and electron block layer whereas Alq$_3$ is an ETL and an emissive layer. In many cases of polymeric OLEDs, a single-layer fulfills all necessary tasks. However, an unbalanced charge injection tends to occur easily which leads to low efficiency of the OLED. On the other hand, an additional hole or electron injection layer will be introduced in some cases to facilitate the charge carrier injection from the electrode. The HOMO (or LUMO level) of the material has to be in between HOMO of the HTL (or LUMO of ETL) and the Fermi level of electrode.

1.2 Physical process and device model

Apparently, organic EL devices behave similarly to conventional inorganic LEDs and thus they have received the label 'organic LED'. However, the detailed behavior of them is quite different. The difference originates from two intrinsically different electronic and optical characteristics of inorganic LEDs and organic counterparts.

The key difference is the way by which charge carriers are injected and transported. In the inorganic LEDs, the charge carriers originate from the dopants in the p-n junction and the charges are injected very easily through the quasi-ohmic Schottky contact between the electrode and heavily doped semiconductors. In the organic case, the organic molecular material behaves nearly as an insulator with very high resistivity (10^{15}-10^{16} $\Omega\cdot$cm at zero bias). The density of free carriers is very low and the carriers need to be injected from the electrode. Additionally, the mobility of charge carriers in the organic layer is low ($<10^{-1}$ cm²/Vs) due to relatively weak intermolecular van-der-Waals force. Therefore, a space charge region is formed within the organic LED. Secondary, for organic materials the optical emission originates from exciton states in contrast to the case for inorganic semiconductors, where direct transitions between valence and conduction states are the dominant process. These differences relative to inorganic LED lead to a special spatial distribution of the internal electric field and the density of electrons and holes in the organic LED and thus to a special opto-electronic feature.

The physical process of OLED devices operation consists of charge injection, charge transport as well as recombination and radiative decay of excitons. A brief overview is given in the following.

a. Charge carrier injection

In organic LEDs, the charge carriers are injected from the electrode into the disordered organic layers. There are two limiting regimes of device operation, namely the space-charge limitation and the injection limitation of the current. Both have been realized experimentally in the OLED. The occurrence of space charge limited current (SCLC) requires that the density of net space charges near the injection contact is high enough that the electric field at the injection electrode vanishes. The electrode is then called 'ohmic' because it provides an inexhaustible carrier reservoir. In contrast, the injection limitation occurs if the injection barrier is so large that the injection current from the contact is inefficient to deliver the maximum possible SCLC in the organic layer. However, even for a given system, there is still an ongoing debate which mechanism prevails. It is found that the electrode- organic contact is nearly ohmic for a very efficient OLED under the voltage used to generate electro-luminescence, otherwise the device would exhibit a poor efficiency. Therefore an effective carrier injection is crucial for achieving high device efficiency. The proper description of the injection process is necessary, which is carried out by the fitting of the current-voltage (I-V) curve of a real unipolar (single type of charge carrier) device using the known models or numerical models.

In the early stages of OLED research, the injection process had been considered to be best described in the term of Fowler-Nordheim tunneling[5-7]. Nowadays, it is shown that thermionic emission with an imaging force barrier lowering (see Section 1.3 in detail) is the correct description[8], at least for the modest barrier height and most voltages of interest. In this model, the number of injected charge carriers is reduced by surface recombination in which a charge in the organic layer recombines with the image charge in the electrode. The image potential forces most of the carriers to jump back into the electrode after entering the organic layer, only by an external field the charges can overcome the image potential.

b. Charge carrier transport

In organic semiconductors, the charge carrier transport is a stochastic process of hopping between isolated molecular sites rather than a coherent motion in a well-defined band. This results in a low carrier mobility, which is typically between 10^{-3} and 10^{-7} cm²/Vs at room temperature and in many cases strongly depends on the temperature and the applied electric field[9]. A description of temperature (T) and field (F) dependence of the mobility associated

with hopping transport is the Poole-Frenkel form[10], derived from the assumption of a decreased hopping energy with increasing local internal field:

$$\mu(F) = \mu_o \exp(\beta \sqrt{F}) \qquad \text{at constant temperature} \qquad (1.1)$$

$$\ln \mu \propto -(T_1 / T)^2 \qquad \text{at constant field} \qquad (1.2)$$

μ_o is zero field mobility. Based on a model for carrier hopping in a Gaussian distribution of states. Bässler et $al.$[11] proposed a similar expression of mobility $\mu(F) \propto exp\ (\beta\sqrt{F})$ but with a more complicated dependence of the temperature. The results from the transient and steady SCLC measurement of hole- or electron-only devices confirmed that the mobility is thermally activated and has the field dependence shown as Eq. (1.1), and the mobility $\mu(T, F)$ in organic semiconductor is described more appropriately by the Bässler model[12-14].

In most of the organic semiconductors, there are significant charge traps in the gap between the HOMO and the LUMO level. Sources for the traps can be the residual impurities from the material synthesis, but also structural traps due to the disorder of molecular conformation[15]. The trapped charges do not contribute to the transport. In the low voltage regime, where a small amount of charges is injected, traps drastically reduce the carrier mobility. This is called the trap charge limited (TCL) transport. Increasing the forward bias leads to more injected carriers and hence more filled traps. At a certain voltage, all traps are filled (trap filled limited). In this case, the device behavior resembles the SCL[16]. The effect of TCL transport is more pronounced in multilayer OLEDs. The energetic depth of the dominant trap E_t and its density N_t can be derived from thermally stimulated current (TSC) experiment[17]. In Alq_3, a trap energy E_t for the electron of 0.6 eV and the density N_t of 2 x 10^{17} cm^{-3} were found[18].

Additionally, it is found that the diffusion current due to the distribution of the space charge is negligible in the field range of interest for most OLEDs[19, 20]. Hence, for the unipolar device, the device current equals approximately the drift current of the carriers

$$I = eF\mu n \qquad (1.3)$$

where n is the density of holes or electrons.

c. Recombination and radiative decay

It has been demonstrated that recombination in organic LEDs is a bimolecular process following the Langevin theory[21- 24] because of a short mean-free path of the carriers and the low carrier mobility of amorphous organic materials. The electrons and holes approach each other with a distance in which their mutual Coulomb binding energy exceeds the thermal energy k_BT, and inevitably recombine (electron-hole capture). The recombination process is diffusion- controlled, the recombination constant R is proportional to the carrier mobility

$$R = \frac{q(\mu_h + \mu_e)}{\varepsilon_o \varepsilon} \qquad (1.4)$$

and the generation rate for excitons G_e

$$G_e = qRnp \qquad (1.5)$$

where n(p) is the density of electrons and holes, ε_o is vacuum permittivity and ε is relative dielectric constant. The total current density in OLEDs therefore includes the double-carrier drift current and the contribution from the recombination; the latter is manifested in the continuity equation

$$\frac{dj_e}{dx} = -\frac{dj_n}{dx} = qRnp \qquad (1.6)$$

The light emission is determined by the competition between the radiative and nonradiative decay channel as shown in Fig. 1.3. Simple spin statistics argument predicts that the ratio of production of triplet to singlet excitons is 3:1, since the triplet state is threefold degenerate. For the common organic molecules with a weak spin-orbit coupling, only the radiative decay of singlet excitons is allowed, triplet excitons will decay nonradiatively.
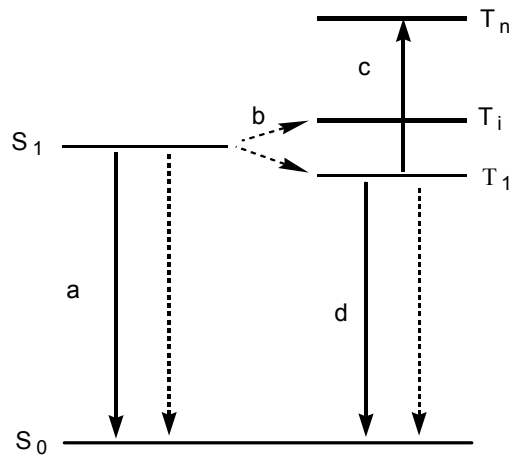
Fig. 1.3. Schematic representation of pathways for singlet decay as well as triplet excitation and decay. Solid arrows represent radiative processes, corresponding to emission of light; dashed line denotes non-radiative processes. Fluorescence (a), intersystem crossing (b), photoinduced triplet- triplet absorption (c), and phosphorescence (d) are represented. S_0 is the ground (singlet) state, S_1 is the first excited singlet, T_1 the fist excited triplet, and T_i and T_n are higher triplet states.

If the singlet excitons diffuse without quenching, they inevitably decay. The internal light emission S is

$$S \propto \int_0^L \frac{s(x)}{\tau_s} dx \qquad (1.7)$$

where s(x) is the density of singlet excitons and τ_s is its lifetime. There are several prominent quenching mechanisms: (1) quenching at or near the injection contact. (2) quenching due to chemical doping by impurities. (3) quenching by free charge carriers, which limits the efficiency at very high operating voltage.

In order to enhance the quantum efficiency of OLEDs, emitter dopants are often used[25, 26]. A certain amount of dopant molecules (guest) is evaporated together with host molecules. They have a much higher PL efficiency compared with host molecules and act as traps for free charge carriers. If an energy transfer from a singlet exciton of the host to the exciton of the guest is favourable or free charge carriers can recombine directly on guest molecule, almost all light emission originates from the guest molecule.

There are two ways in which the exciton can be created at an emitter dopant: (1) The recombination of a trapped hole (or electron) with another free charge carrier and (2) the energy transfer from a host molecule to a guest molecule. Process (2) is called Förster energy transfer between molecules. The energy transfer rate has been investigated extensively by several groups.

d. Device model

One will expect that device models for OLEDs will be developed to describe current-voltage-luminance behavior and to carry out the performance optimization based on the material parameters and the processes considered above. However, in general, there is no analytic solution for the bipolar current behavior relevant to complete OLED structure. Only when both electron and hole mobilities are field-independent, when the diffusion and trapping can be completely ignored, and when both anode and cathode provide ohmic contacts a complete solution can be obtained[27, 28]. Furthermore, many of important properties of organic materials are poorly known at present. This makes it difficult to evaluate the measured I-V features of such devices. The most realistic way is to set up a numerical model based on some properly- determined material parameters, which has been made by a number of groups[18, 19, 29, 30]. However, none of the models can give a complete and detailed description for the device operation. Most of them can only describe the behavior of the device with special materials and configurations.

1.3 Simple models for I-V curves

In the following, we consider some models that describe the process of charge carrier injection and transport in the semiconductors. These models are appropriate for inorganic semiconductors with an extended band state and under the condition of unipolar devices in

which predominantly one type of charge carrier is involved. For the materials used for organic LEDs, only localized disorder states exist and the carrier mobility is low. However, these models provide a good starting point for analysing and understanding the carrier injection and transport behavior in organic semiconductors and even in OLED devices.

(a)   (b)
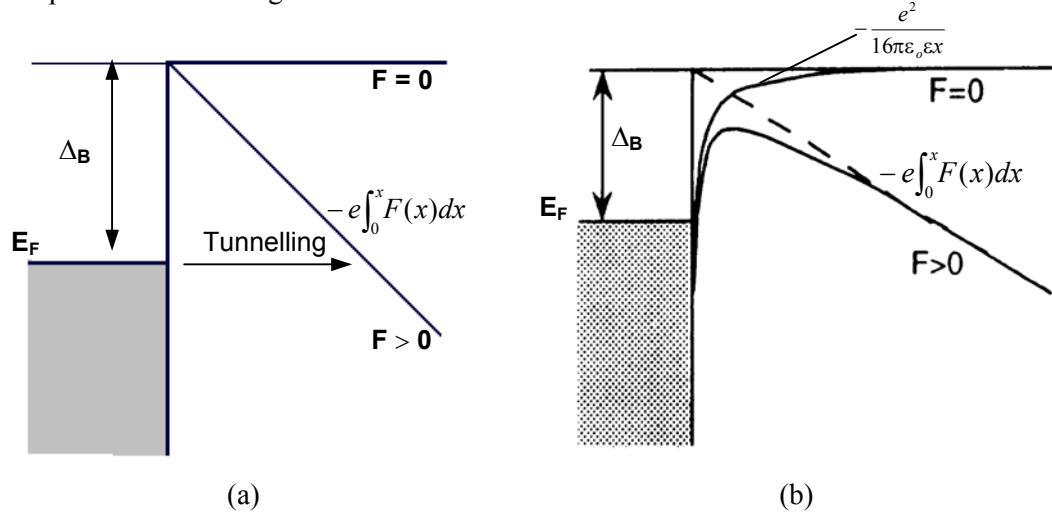
Fig. 1.4. Schematic diagram of two models for the injection process: (a) Fowler-Nordheim (FN) tunneling model, (b) Richardson-Schottky (RS) thermionic emission model.

 Carrier injection into a semiconductor is usually treated in terms of Fowler-Nordheim (FN) tunnelling or Richardson-Schottky (RS) thermionic emission. The FN model ignores the image charge effect and considers merely the tunnelling from the metal through a triangular barrier into an unbound continuum state (see Fig. 1.4 (a))[31]. It predicts a temperature independent injection current density

$$j_{FN} = BF^2 \exp(-\frac{2\alpha\Delta_B^{3/2}}{3qF}) \tag{1.8}$$

with $B = \dfrac{q^3}{8\pi h\Delta_B}$ and $\alpha = \dfrac{4\pi\sqrt{2m^*}}{h}$. m* is the effective mass of the charge carriers, and

ϕ_B the potential barrier for carrier injection. The FN model can give the reasonable value for the injection barrier in the high field case.

 The RS model is based on the image force lowering of the barrier height (see Fig. 1.4 (b))[31, 32]. The carriers are injected when they acquire a sufficient thermal energy across the potential maximum that results from the superposition of the external and the image charge potential

$$j(F) = A^*T^2 \exp(-\frac{\Delta_B - \beta_{RS}\sqrt{F}}{k_B T}) \tag{1.9}$$

with the Richardson constant $A^* = 4\pi m^* k_B^2 / h^3$ (= 120 A/(cm²K²) for m* = m$_o$) and

$\beta_{RS} = \sqrt{q^3 / 4\pi\varepsilon\varepsilon_o}$. This model neglects the inelastic backscattering of the hot carriers during

the injection. In the disordered organic semiconductor, the injected carriers have to overcome the random energy barrier caused by disorder, which leads to an enhanced backflow of injected carriers into the electrode. This process of the injection into a disordered hopping system has been studied analytically[33] and by Monto-Carlo simulation[34, 35]. For example, the simulation by Wolf et al.[35] showed that although the injection mechanism resembles the RS model, a quantitative difference exists concerning the absolute values of the current, which is found by orders of magnitude lower than that predicted by the RS constant. Additionally, some work to overcome the shortcomings of the two models considers the inclusion of the tunnelling contribution into the RS model[36].

When the carrier injection into the transport layer is efficient enough, so that the injection contact is able to provide a higher carrier density than the material has in thermal equilibrium state without carrier injection, the SCL current can be observed.

In the case of a perfect insulator without intrinsic carriers and traps and for the carrier mobility independent of the electric field, the SCL current density obeys the Mott-Gurney equation[37]

$$j_{SCLC} = \frac{9}{8}\varepsilon\varepsilon_o\mu\frac{V^2}{d^3}$$ (1.10)

where d is the thickness of the layer and μ is the carrier mobility. The importance of the trap-free SCLC is that it is the maximum possible unipolar current a sample can sustain at a given applied potential.

In the presence of traps, the current is in general lower. At very low voltages, one expects an ohmic conduction via thermally generated free charges in the bulk. The current density is described by

$$j = e\mu n_o V / d$$ (1.11)

where n$_o$ is the density of the thermally-generated background free charges. Increasing the voltage leads to the filling of traps gradually. This reduces the density of empty trap states and thus increases successively the effective carrier mobility $\mu_{eff} = \mu(n_{inj}/n_t)$. Here n$_t$ is the total trapped charge density and n$_{inj}$ is the injected charge density. Therefore, a higher power-law dependence of the current on the voltage is observed. In the case of an exponential trap

distribution in the gap, the TCL current density derived from the trap distribution is given by[16, 31]

$$j_{TCLC} = N_{LUMO} \mu q \left(\frac{\varepsilon \varepsilon_o l}{N_t q(l+1)} \right)^l \left(\frac{2l+1}{l+1} \right)^{l+1} \frac{V^{l+1}}{d^{2l+1}} \tag{1.12}$$

where l is given by $l = E_t / k_B T$ and N_{LUMO} is the density of states at the LUMO level. The value of l can be experimentally obtained from the slope of $\ln j$ versus $\ln V$. From Eqs. (1.11) and (1.12), the transition from ohmic to trap-limited conduction occurs at the voltage $V_{\Omega\text{-}T}$

$$V_{\Omega-T} = \left(\frac{n_o}{N_{LUMO}} \right)^{1/m} \frac{\left(q N_t d^2 / m\varepsilon \right)(m+1)^{(2+1/m)}}{(2m+1)^{1+1/m}} \tag{1.13}$$

At sufficiently high injection level, traps are completely filled and therefore they do no longer influence the transport of electrons. An ideal SCL behavior is expected.

1.4 Electroluminescent efficiency

The internal quantum efficiency η_{int} of organic LEDs, defined as the ratio of the number of photons produced within the device to the number of electrons flowing in the external circuit is given by[38]

$$\eta_{int} = \gamma \eta_s \eta_{PL} \tag{1.14}$$

where η_{PL} is the PL quantum efficiency (the efficiency of radiative decay of all singlet excitons) and η_s is the efficiency of the production of singlet excitons. γ is the charge balance factor which represents the ratio of the number of excitons within the device to the number of electrons flowing

$$\gamma = j_r / j \tag{1.15}$$

with the recombination current

$$j_r = j_h - j_h' = j_e - j_e' \tag{1.16}$$

and the total current in external circuit

$$j = j_h + j_e' = j_e + j_h' \tag{1.17}$$

where $j_{e,h}$ is the injected electron and hole current, respectively and $j'_{e,h}$ denotes the respective fraction reaching the counter electrode without recombination. In order to achieve an efficient EL it is therefore necessary to have a good balance of the electron and hole current and an efficient electron-hole capture within the emissive layer, the obtainment of the γ up to one is desirable. One can discuss the recombination current j_γ based on the examination of charge

recombination region. When a narrow recombination region is located within an emissive layer, the local charge density will be sufficiently high to ensure that each charge carrier passes within a collision capture radius of at least one other carrier. An efficient capture can thus be obtained. In the molecular OLEDs, the two-layer structure provides the necessary energetic barrier for the carrier transport at the heterojunction between two semiconductor layers, which effectively localizes the recombination at or near the interface so that the current balance can be achieved.

The maximum value for the efficiency of singlet exciton production η_s is 1/4 due to spin statistics for the production of singlet and triplet excitons. This sets an upper limit of 25% for the conversion efficiency of injected carriers into photons via the singlet excitons. It has been demonstrated recently that by choosing a material with a high yield of short-lifetime phosphorescence, the triplet emission can be harvested for making very efficient organic LED devices[39, 40]. The PL efficiency η_{PL} is mainly governed by the intrinsic electronic nature of the molecular materials used. The appropriate emissive centers should be selected carefully and the quenching process of singlet exciton, which may decrease the PL efficiency, should be hindered.

Due to the losses of light emission by total internal reflection and wave-guide within the device, the internal quantum efficiency η_{int} is connected to the external quantum efficiency η_{ext} by a factor η_{out}[41]

$$\eta_{ext} = \eta_{int}\eta_{out} \tag{1.13}$$

where η_{ext} is defined by the ratio of the number of emitted photons outside the device to the number of charges injected into the device and η_{out} is approximately evaluated by using the refractive index of emissive medium n

$$\eta_{out} = 1/2n^2 \tag{1.14}$$

1.5 The development of organic LEDs

The first prototype OLED by Tang et al[3] consisted of an aromatic diamine as hole transport layer, a highly efficient electron transport and emissive layer of Alq_3, and a magnesium-silver alloy as electron injection contact. The OLED needed a voltage of 5.5V to reach a luminance of 100 cd/m² and had a current efficiency of 2 cd/A. Since then, intensive effort has been made to improve the device performance, i.e. the reduction of operating voltage and the enhancement of the EL efficiency (the definition of several types of 'efficiencies' for the OLED is given in chapter 2). The OLED optimization can be done by utilizing new molecular

layers with appropriate properties as well as new device structures, which includes two main aspects: (1) the enhancement of injection and transport of holes and electrons; (2) the progress regarding the EL emissive layers. Here, the aspect on the material synthesis and characterization is not the focus. Its status has been reviewed in refs [42-44].

a. Electrode interfaces

The nature of the interface between the electrode and the organic layer is of paramount importance in determining the charge carrier injection and thus the device performance. The control of the interface may be one of the most important factors in the success of OLEDs[45]. A combined experiment-theory approach is applied to a wide range of π-conjugated polymers and molecules as well as to the early stages of metal/organic interface formation[45, 46]. Two important factors will be considered: (1) chemical interaction at the interface; (2) the cleanliness of the materials and atmosphere (vacuum system) under which the interface is formed.

Interfacial chemical reaction may lead to the diffusion (e.g. molecules or metallic atoms) and doping (e.g. by dopants or impurities) at the interface region as well as the formation of an interfacial layer. Salaneck *et al.* have studied the interaction between the polymer surface and the submonlayer of various metals by XPS and UPS. For the case of the alkali- and alkaline earth metals sodium and calcium deposited in situ upon a clean surface in ultrahigh vacuum (UHV), the interaction with PPV leads to the occurrence of Na^+ and Ca^{+2} cations accompanied with a n-doping of PPV[47, 48], which stores charges in the bipolaron band within the LUMO-HOMO gap. In contrast, when there is a large amount of oxygen-containing species at the PPV surface (as a result of exposure of the sample in air), an interfacial layer of calcium oxide is formed with a thickness of 2-3 nm during the deposition of calcium in UHV[49]. Only then the metallic calcium is deposited. Such a thin layer of calcium oxide is observed to increase EL efficiency and device lifetime[50]. On the other hand, the deposition of aluminium on clean PPV (or a substituted PPV) surface leads to the diffusion of Al atoms into the near-surface region and to the formation of covalent bonds with the PPV that is localized within a characteristic length scale of 2-3 nm[51].

Additionally, a dipole layer may be formed at the metal-organic interface due to a charge transfer, a redistribution of the electron cloud, and an interfacial chemical reaction[52, 53]. As observed by Seki et al[54, 55], the deposition of molecular TPD on a clean Au or ITO surface leads to the interfacial dipole with a magnitude $\Delta = -0.3 - -0.5$ eV which indicates a downward shift of the vacuum level of TPD side relative to the metal side. The dipole effect is more pronounced at some metal-on-organic interfaces such as Al or Au on an Alq_3 layer. The

values of Δ are bigger than 1 eV[55, 56]. For the interface with a dipole layer, the carrier injection barrier will be modified by -Δ from the simple case in which the vacuum level is aligned at the interface. The modification is critically important for the carrier injection property.

While the clear evidence for strong chemical interactions at metal-organic interfaces, the size of the energy barrier for electron and hole injection still scales with the electrode work function[57]. In absence of doping, interfacial dipole and other interfacial effects, and assuming a vacuum level alignment, the energy barrier for carrier injection is given by the energetic offset between work function of the used metal and the energy level (HOMO or LUMO) of the organic materials (see Fig. 1.2)

b. Hole injection and transport

ITO commonly serves as the anode of OLEDs. Although its properties such as the work function and the surface morphology vary drastically on the preparation condition, ITO offers a combination of high transmission (> 90% at 550 nm) and a low resistivity that is hard to replace. It has been found that an oxygen plasma treatment[58, 59] or an UV-ozone cleaning[60] of ITO can enhance the work function and remove the surface contamination so that the hole injection and the device efficiency can be improved. On the other hand, the introduction of a hole-injection layer will be more favorable in many cases. Their purposes are to enhance the hole injection, meanwhile to improve the contact at the ITO/organic interface as well as to hinder the release of indium and oxygen into the emissive layer and thus to increase the device stability.

Small molecular copper phthalocynanine (CuPc) [61, 62] and star- burst m-MTDATA layers[63, 64] have been used as such interfacial layer. The interposing of thin CuPc (12-15 nm) or m-MTDATA lowers the operating voltage and enhances drastically the device stability of molecular OLEDs. The ionization potential (corresponding to the HOMO level) is 5.1-5.3 eV for CuPc[65] and 5.1 eV for m-MTDATA[66], in between the HOMO of HTL and the Fermi level of the ITO, and therefore lowers the energetic barrier for the hole injection. The ITO/m-MTDATA contact is believed to be nearly ideal ohmic at higher fields. High device stability is attributed to the favorable feature for forming amorphous films. However, their glass transition temperature (T_g) is relatively low, which will lead to the crystallization and thus to an interfacial roughening upon thermal stress and will be disadvantageous to the long-term stability.

Some of the chemically doped conducting polymers have been used as buffer layer on polymeric LEDs. These p-doped conjugated polymers, including polyaniline and polythiophene derivative PEDT (see Chapter 5), show a good environmental stability and a

high transparency. Upon cast on ITO by a solution process they behave as a modified anode due to their metallic properties. Several groups have reported that the polymer anodes improve the hole-injection and device efficiency[67-71]. Furthermore, these polymeric layers planarize the anode surface and thus reduce the probability of electrical shorts and additionally hinder the diffusion of indium and oxygen from ITO into the emissive layer, which results in an improved device uniformity and longevity. These doped polymeric anodes have a high work function of 4.8-5.0 eV[7, 72], providing a low barrier for hole injection. It is also likely that there is some diffusion of dopant of the polymeric anode into the semiconducting layer, leading to a dopant profile within this layer. Such a diffusion process must be restricted close to the interface to provide a stable operating over a long time. It was indeed found that the devices with polymeric dopant show a longer operating time relative to those with small molecular dopant. The polymeric dopant is expected to be relatively immobile[68].

Due to large surface energy mismatch at the hydrophobic arylamine HTL-hydrophilic ITO anode interface, physical dehesion/dewetting will undergo for the HTL especially for the low-T_g TPD, which leads to a poor hole-injection contact and a thermal instability of OLED. Cui et al have modified the ITO-HTL contact by the introduction of an ultrathin tricholorsilyl-functionalised triarylamine (TAA) and TPD (TPD-Si$_2$) from a self-assembly process[73, 74]. Due to the structural similarity to a HTL such as TPD, TAA or TPD-Si$_2$ moderates effectively the surface energy mismatch at the anode-TPD interface so that TPD completely wets the ITO/TAA (TPD-Si$_2$) surface even upon thermal stress. This promotion of the interfacial contact/adhesion significantly enhances the hole-injection efficiency which originates from the reduced interfacial contact resistance. Furthermore, the OLEDs with the anode-adhesion layer exhibit excellent thermal stability, as a consequence of the suppressing of dehesion and crystallization of the hole transport TPD layer.

Nanoscale layers (in a range of several Å to several nanometers) of inorganic insulating oxides have also been utilized as hole-injection contact for molecular OLEDs. The insertion of an ultrathin SiO$_2$ layer can improve the EL efficiency[75], which is attributed to a decrease of the barrier height for hole-injection due to the existence of a dipolar layer at the interfacial contact[76]. A thin CuO$_x$ interlayer prepared by the oxidation of a deposited Cu layer, plays a similar role on enhancing the hole injection[77]. However, its disadvantage is the reduced transmission of the ITO anode even for a thickness in the nanometer range. Recently, studies on the effect of a Nickel oxide (NiO) layer on the OLED performance have been reported[78]. NiO is a p-type transparent conducting oxide with a high work function of 5.0 eV. Thin NiO

sandwiched between the ITO anode and the HTL results in a much more efficient hole-injection relative to other oxide buffers. Additionally, an ultrathin layer of the high-work function Pt metal has been deposited on ITO to constitute a modified ITO anode[79]. The modified anode enhances drastically the hole-injection efficiency and the contact between the ITO and the TPD layer became nearly ohmic, which reduces remarkably the operating voltage of the TPD/Alq$_3$ device. However, such devices show a lower breakdown threshold compared to those without a Pt layer.

On the other hand, much effort has been made to develop novel hole-transport layers that exhibit good hole injection/transport properties and the feature of forming a stable glassy film with high T_g. Some examples are PPD and ISB[80] (the amine- constituents of TPD family), tetramer and pentamer of triphenylamine TPTE and TPPE with high T_g[81], as well as the star-shaped molecules[63]. The p-type doping of hole transport layers is another effective approach to enhance the hole injection and transport of the HTL. It results in two important effects: (1) remarkably enhanced bulk conductivity of the HTL and thus a reduced series resistance of the device. (2) a thin space charge layer in the HTL near the anode/HTL contact which enables more efficient tunnelling injection of holes similar to the behavior of a Schottky contact. Chemical doping of conjugated polymers by various dopants (FeCl$_3$, I$_2$ and SbCl$_3$, etc) from the solution process is a simple way[82- 84], and OLED devices with 650 nm thick HTL have been prepared with a low operating voltage[82]. Leo and collaborators have doped a molecular HTL with F$_4$-TCNQ by coevaporation of the HTL and the dopant in high vacuum[85]. Using a p-i-n LED structure (i.e. p-doped HTL/intrinsic emitter layer/n-doped ETL)[86] and a thin block layer between the HTL and the emissive layer[87], they have realized a very low operating voltage of 2.55V together with a high EL efficiency.

In the present work, we will utilize the semiconducting and conducting polythiophenes from an electrochemical process as hole-injection contact. The attempt is made to improve and optimize the hole-injection by adjusting the doping level of polythiophene interlayers, in order to enhance the performance of small molecular OLEDs.

b. Electron injection and transport

In order to achieve an efficient electron injection, low-work function metals such as magnesium or calcium should be used as cathode. However, these reactive metals are unstable under ambient conditions. Aluminium and the alloy of magnesium and silver provide more stable cathodes. Unfortunately they show an inefficient electron injection. The alloys of Al

and low-work function metals (e.g. Al:Li) are better choice. An even better approach is the introduction of a thin insulating lithium-fluoride (LiF) layer between the electron transport layer (ETL) and Al cathode[88, 89], which enhances dramatically the electron injection and the device efficiency although the mechanism is not completely clear yet. A similar effect was observed for utilizing alkali- or alkaline earth metal fluoride layers[88, 90], as well as organic complexes such as alkali metal benzoate (C_6H_5COOLi)[84] and lithium quinolate (Liq)[91]. It is generally believed that free lithium is released from the thin interlayer into the ETL leading to an n-type doping, which is supported by the work of Kido et al.[92]. By direct mixing of Li atoms into the ETL near the cathode the same effect was observed. Recently, it was also observed that a thin NaCl layer can act as an effective electron injection medium[93]. At the side of the ETL, some materials with higher electron transport capability than Alq_3 have been utilized, such as tri(4-methyl-8-quinolinolato)aluminium $(Almq_3)$[62], 4,7-diphenyl-1,10-phenanthroline (Bphen)[86] and oxadiazoles[94].

c. Light emission

One approach for improving the EL efficiency is to search for new emissive materials, for example chelate metal complexes[95] or other emissive molecules in the Alq_3 family (e.g. $Almq_3$)[62]. However, a more successful way was the use of emitter dopants. Organic dopant molecules with excellent PL properties are blended by an amount of 1-3 % into the host layer. With doping the energy is transferred from the host molecule to the guest, or excitons are directly created on the guest molecules. The typical efficiency of OLEDs with pure Alq_3 as an emitter, which is up to 5 cd/A[88, 92, 96], can be increased to more than 10 cd/A[26, 62].

In order to achieve higher efficiencies, one has to overcome the limitation by the spin statistics. As shown in the preceding sections, in the common organic emitter molecules, only the singlet state can decay radiatively, and 75% triplet excitons decay nonradiatively. One approach is to introduce species that will allow efficient triplet luminescenece (phosphorescence). This can be provided by high-atomic-number elements with strong spin-orbit coupling. The platinum porphyrin or the Ir (ppy)$_3$ complex has been successfully used as dopant in both molecular[39, 40, 97, 98] and polymeric[99] hosts. Both singlet and triplet excitons generated in the host material are collected in the phosphors which show efficient phosphorescence. Excellent current efficiency up to 67 cd/A and luminous efficiency of 55-65 lm/W has been achieved recently[100], i.e. nearly 100 % internal phosphorescence quantum efficiency is reached. Such type of emitter molecules shows a much narrower emission than the singlet emitters. However, since the lifetime of phosphorescent state is long, the

probability of energy back-transfer and triplet- triplet annihilation is increased which results in a reduced efficiency at higher voltages.

1.6 Differences between small molecular LED and polymeric LED

The preceding sections have placed an emphasis on those OLEDs deposited by vacuum sublimation of low-molecular-weight organic semiconducting materials. The counterpart to the molecular LED is the polymeric LED (PLED) with conjugated polymers, which is prepared by spin-coating from solution.

In principle, the device physics and EL mechanism is quite similar for both types of OLEDs. Although PLEDs may be multilayered, they can be distinguished from small molecular devices by combining more than one feature (charge injection and transport, emission) in a single layer. The early-stage PLED device showed a very low efficiency of

Table 1.1 The performance data of representative polymer OLEDs.

Color	Efficiency[a] (lm/W)	Brightness[b] (cd/m²)	Lifetime[c] (h)
Red	2.15	2000	> 40,000
Green	18	10^4	>10^4
Blue	1.5	10^3	2500
Yellow	21	10^5	14,000
White	1.37	400	7000

Source: from **ref**. 104.
a. At 100 cd/m²
b. At 5.5 V
c. Room temperature data

0.3% and a short lifetime[4]. However, in the past decade new EL polymer materials and chemical purification processes have been developed extensively, also the multilayer structure, e.g. an additional hole injection layer, is introduced. The present PLED devices made from e.g. the derivatives of PPV and polyfluorene have high efficiency and long lifetime comparable to the small molecular counterpart[101-103]. Table 1.1 shows the representative data of a range of PLEDs recently achieved. Furthermore, the operating voltage of PLEDs (2.5-3.5 V) is usually lower compared to small molecular OLEDs (4.5-6 V). The underlying reasons are given as follow: (1) thinner organic layer for PLED (60-100 nm); (2) occurrence of band bending at the metal contact, which eases the charge carrier injection. The behavior may be caused by the unintentional doping from intrinsic impurities[105].

From a technological point of view, the differences between molecular LEDs and polymeric LEDs lie in two aspects. One aspect is involved with the difference of preparation processing. The organic materials for small molecular LEDs can be cleaned repeatedly by train sublimation

until the purity reaches the desired level and the evaporation in the HV conserves the purity, which will increase the EL efficiency. Furthermore, the deposition of layers as many as needed (also including the dispersion of emitter dopants) can be easily done by consequent evaporation (or coevaporation) in vacuum to obtain high EL efficiency. In contrast, the polymer layers from solution processing sometimes suffer from the impurities originating from their synthesis or remainder of solvents. Furthermore, the number of polymer layers is usually restricted to two, because the solvent of every new cast layer must not dissolve the underlying layer. Thus it is not easy to maintain balanced charge injection and transport over a reasonable voltage range in single-layer device. The imbalance results in the loss of EL efficiency. To overcome this limitation, mixed layers of a matrix polymer and several transport molecules are sometime used but they suffer from a decreased mobility[106]. However, the fabrication of polymer devices from solution processes is relatively simple and cheap especially for recent solution-patterning techniques such as ink-jet printing[107].

The second difference between molecular OLEDs and PLEDs lies in the thermal and mechanical durability for both types of OLEDs. The amorphous layer for small molecules undergoes crystallization during the device operation especially upon thermal stress, which results in a device instability. Moreover, such OLEDs usually are lack of mechanical durability. In contrast, PLEDs based on polymer layers can avoid the problem of thermal instability, and show a good mechanical durability so that such devices can be fabricated on the flexible substrates.

At present, it is not clear which process technology succeeds or if both will coexist. Both exhibit some advantages and comparable device performance. Hence the choice of the material system should depend on the application. Both types of the OLEDs have been developed worldwide, with more intensive activities for molecular OLEDs in Japan.

1.7 Status towards applications

The performance of the present organic LEDs has met many of the targets necessary for the application in displays. In 1997, Pioneer commercialised the OLED in a 256 x 64 pixels green monochrome display[108]. Soon after they started to produce the car stereos with a multicolour dot matrix display based on small molecular OLEDs[109]. Backlightings and segmented displays were available by Philips based on polymer LEDs. In 2002, a novel 17-inch full-color XGA display (1280 x 768 pixels) had been exhibited by Toshiba[110]. Today, many companies are performing the development of OLED displays, and OLED sales are forecasted to reach 5.8% of the total worldwide flat-panel revenue by 2007[42].

The organic EL display is an emissive display, providing certain fundamental advantages over liquid-crystal display (LCD) for high-quality and high-information-content video application. The advantages include wide view angle ($> 170^{\circ}$), fast display response time (microseconds), broad color range and high dark contrast. It is now viewed as an important competitor with LCD for a variety of displays. The first application will focus on mobile phones, personal digital assistants (PDA), digital cameras, camcorders and car electronics. However, high-information-content displays for computers and TVs will likely not be targeted in the next several years. This market will explode with the development of the more effective technology for producing large-area flat panel display, and with the availability of the OLEDs that are more stable and consume very little energy.

There are two types of OLED display architectures: passive matrix and active matrix. A passive matrix-addressed display has a relatively simple construction. However, it requires that the pixels are driven row-by-row under pulsed condition. Both resistance loss in the conductive track and efficiency reduction for the diode at high current densities limit the pixel number and thus the display size and the resolution. In an active-matrix display, each individual pixel can be switched on or off within a frame time by the underlying polysilicon transistor drive circuit. Therefore the drive does not suffer from the limitation occurring in passive matrix display, which makes it suitable for large-area and high- resolution displays. Demonstrators for such a display have been made[101].

1.8 Previous effort to utilize electrochemical process in OLED fabrication

Most of the conducting conjugated polymers employed as carrier injection contact in OLEDs, such as polyaniline and PEDT, are prepared by chemical polymerization, i.e. oxidative polymerization using the catalysts from which solution possible polymers are available. Another approach for polymer synthesis is the electrochemical polymerization (see detailed in Chapter 2). Electropolymerization proceeds by a succession of electrochemical reactions based on the coupling of radical cations produced from the electroxidation of monomers on the anode surface[111]. Compared to chemical polymerization, it presents several advantages such as rapidity, absence of catalyst and thus high chemical purity, control of film thickness by the deposition charge, and obtainment of the polymer in the oxidized conducting form. In particular, the oxidation state (i.e. doping level) of the polymer can be adjusted conveniently in successive electrochemical redox (reduction-oxidation) processes. Since the doping level corresponds to the energy levels such as the work function of the polymer (see

details in Chapter 5), one can actively influence the opto-electrical and carrier injection/transport properties of the polymer by an electrochemical treatment.

One of the attempts for utilizing the electrochemical process in the OLED preparation is light-emitting electrochemical cell (LEC). Pei et al.[112] have shown that with the addition of a salt and ion transport material such as poly(ethylence oxide) to the conjugated polymer, very low barriers for the charge injection are found. They attributed it to the formation of a p-doped region near the positive electrode and an n-doped region near the negative electrode in the polymer, with the doping arising from electrochemical reaction under drive condition. However, the phase separation in the polymer is a significant problem. Recently, Destri et al. utilized a carboxy-substituted polyalkylthiophene as an EL emission layer in PLED[113]. Gross *et al.* introduced poly (4,4'-dimethoxy-bithiophene) (PDBT) from the electropolymerization as the hole-injection interlayer for polymer LED[114] and showed that the energy barrier for hole injection can be continuously tuned with the doping level of PDBT by an electrochemical doping process. However, the microstructure of the layers from the electro-polymerization is often not fully dense-packed and a large surface roughness may exist so that it is disadvantageous to such electronic application as in OLEDs. In the case of PDBT layer a very large thickness (*ca.* 550 nm) of the polymeric emissive layer is necessary to avoid the operating instability due to the inhomogeneity of PDBT, which results in a high operating voltage and a low luminous efficiency of PLED.

The morphology and electrical properties of electrochemically prepared polymer films depend strongly on the electrosynthesis conditions such as the nature of monomer and dopant, film thickness as well as anode[111]. The growth mode also plays an important role on the film morphology[115, 116]. It was found that in many cases 2D layer-by-layer growth takes place at least for the initial stage of the growth[116]. With the optimization of the parameters for the electropolymerization, homogenous ultrathin (lower than several tens of nanometers) layers with a low surface roughness can be prepared which fulfills the requirement for EL devices even for small molecular OLEDs. An alternative approach to the purpose is the electrochemical modification of polymer films cast from solution. For example, solution-cast poly(phenylensulfidephenyleneamine) (PPSA) has been electrochemically doped by Li et al.[117] which allowed a continuous variation of electroptical properties as a function of the doping level. By electrochemical doping/depoping processes such kind of well-defined polymer with a controllable and stable doping level can be expected to serve effectively as a carrier injection contact in OLEDs, which will be the main subject of the present work.

1.9 Aim of this work

This work will focus on polythiophene (PT) and its derivatives prepared from electrochemical processes. The polythiophene family has a prominent position in various conjugated polymers due to the high environmental stability of its neutral and in many cases doped conducting state as well as its structural versatility to allow the synthesis of new derivatives by the substitution of side chains. These derivatives can show tailored features for the use in PLEDs[113, 118] and organic field effect transistors[119, 120]. The electropolymerization is a common and preferred method to prepare PT layers even though the solution-processible PTs are available now. Generally, PT materials have a high hole mobility. Moreover, most of them show the HOMO level (for the undoped semiconducting state) or the Fermi level E_F (for the doped state) in between E_F of ITO and the HOMO level of HTL (e.g. NPB, TPD) of OLEDs which make it possible to serve as hole injection interlayer. Several investigations have been made on the injection and transport properties of several PTs in single-layer sandwiched devices[121- 123]. The water-soluble PEDT doped with PSS is the most well known among a few of PT materials acting as carrier injection layer.

In this work a more detailed and comprehensive insight of PT materials with respect to their carrier injection and transport properties will be given in the following aspects:

(1) The improved approach and growth condition of the electropolymerization is developed to fabricate well- defined ultrathin PT films favorable for the use in molecular EL devices. The film will be employed as hole-injection contact in order to reduce the large barrier for hole injection from the ITO anode into the hole transport layer. The device stability could be enhanced considering the possible improvement of the ITO/organic contact, as well as the high thermal and chemical stability of the PT materials.

(2) By the possibility to adjust the doping level of the polymer by electrochemical oxidation/reduction process, we intend to tune the electrical properties and energy levels of the highly electroactive PTs on ITO, which serve as the hole injection contact. Especially, our investigation will be focused on the cast layers with a smooth morphology since a well-defined morphology of organic layers is crucial for OLED fabrication. Our goal is to modify the energy barrier for hole-injection therefore to achieve an ideal hole-injection feature as well as improve the performance of OLEDs.

2. Main experimental methods

2.1 Determination of optical parameters of OLEDs

Since most applications of OLEDs will be related to the visible light emission, the optical characteristics of OLEDs are given in photometric and not in radiometric units. The four photometric fundamental quantities (luminous flux (in lumen (lm)), luminous intensity (in lm/sr (cd)), illuminance (in lm/m² (lux)) and luminance (in cd/m²)) are connected with the radiometric equivalents (radiant flux (in W), radiant intensity (in W/sr), irradiance (in W/m²) and radiance (in W/m²·sr)) by the 1931 CIE Standard Observer function (photopic function) $V(\lambda)$. For example, the luminous flux ψ_V is defined as radiant flux ψ_e weighted by $V(\lambda)$ in the following equation

$$\psi_V = K_m \int_{380nm}^{780nm} \psi_e(\lambda) V(\lambda) d\lambda \qquad (2.1)$$

where $K_m = 683$ lm/W is the conversion constant and $d\lambda$ is the wavelength increment (nm).
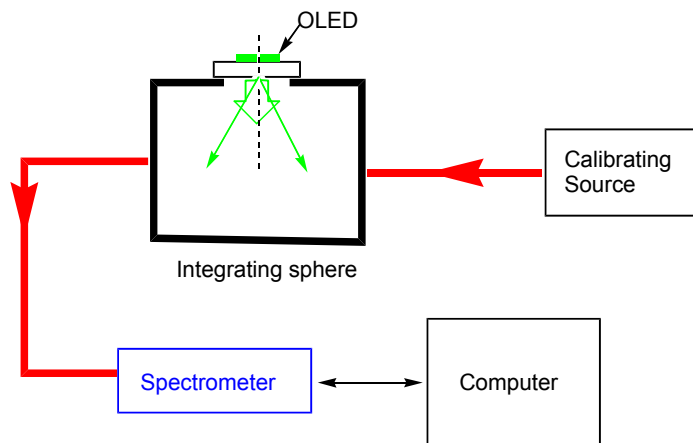

Fig. 2.1 Scheme of the optical characterization using an integrating sphere.

The most important characteristic for the OLED devices is luminance that is usually measured by a calibrated photodiode. In our case, the luminance (cd/m²) is determined in an integrating sphere connected with a photo-spectrometer, which is calibrated by a known halogen lamp source. Figure 2.1 shows the scheme for the measurement system. The integrating sphere is a cell, which collects all of light radiance from the emitter. Its inner wall is a nearly ideal light-scatterer and thus an even illumination can be obtained. The light radiance in forward direction from OLED is collected by the upper exit (about 10 mm in

diameter) of the integrating sphere and then the homogeneously scattered light is transported from a small exit on the wall to the spectrometer through a fiber system. The EL spectra of the device are obtained and the spectral intensity $I(\lambda)$ is proportional to the radiant flux ψ_e of the OLED. At a given wavelength λ_i, the spectral intensity $I(\lambda)$ is
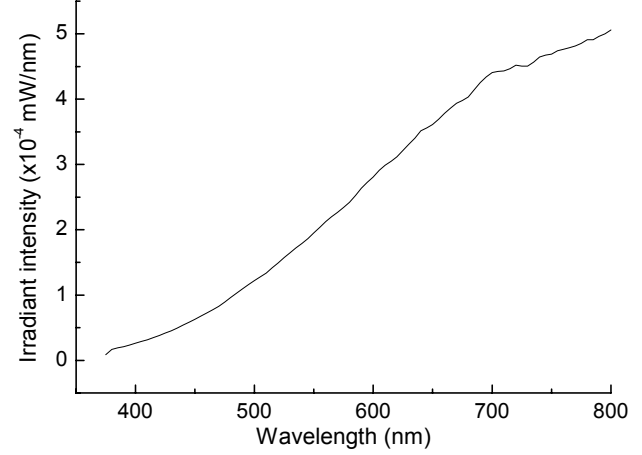

Fig. 2.2 Irradiant intensity of a halogen lamp source. Wavelength step is 5 nm.

$$I(\lambda_i) = AS(\lambda_i)\psi_e(\lambda_i). \tag{2.2}$$

A is the conversion factor and $S(\lambda_i)$ is the response of the spectrometer.

We utilize a calibration source with a known radiant flux $\psi_{eR}(\lambda)$. Its spectral intensity is given by

$$I_R(\lambda_i) = AS(\lambda_i)\psi_{eR}(\lambda_i) \tag{2.3}$$

Therefore

$$\psi_e(\lambda_i) = \frac{I(\lambda_i)}{I_R(\lambda_i)}\psi_{eR}(\lambda_i) \tag{2.4}$$

Using the radiant flux data ($\psi_{eR}(mW/nm) \sim \lambda(nm)$) of the calibration source shown in Fig. 2.2 and integrating the EL spectrum of the sample, the luminous flux ψ_V of the sample is obtained:

$$\psi_V = K_m \sum_i \frac{I(\lambda_i)}{I_R(\lambda_i)}V(\lambda_i)\psi_{eR}(\lambda_i)\Delta\lambda_i \tag{2.5}$$

Assuming a perfectly diffusive EL emission surface with a Lambertian emission (which is approximately the case for an OLED neglecting the effects of micro-cavity and Fresnel-loss[41]), the luminous intensity $I_V(\theta)$ at a given direction

$$I_V(\theta) = I_V(0)\cos(\theta) \tag{2.6}$$

$I_V(0)$ is the luminous intensity in forward direction, then

$$L = \frac{\psi_V}{\pi \cdot \Delta S} \tag{2.7}$$

where ΔS is the area of emission zone of the OLED, L is the luminance.

To make an *in situ* optical characterization (in vacuum), we established a simple measurement system (as shown in Fig. 2.3). A probing head made of a fiber (0.2 mm in diameter), fixed on the back of an OLED perpendicularly, receives the light emitted from the
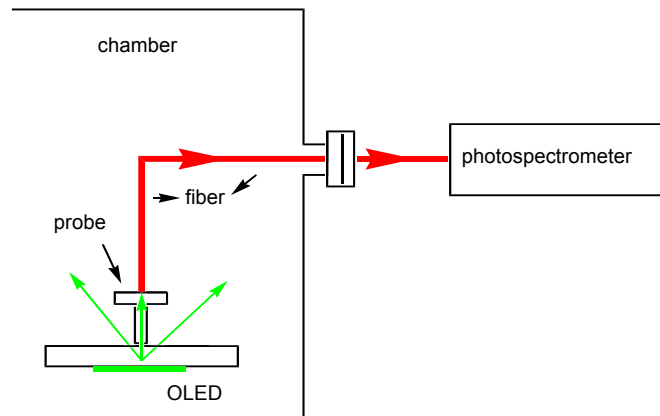

Fig. 2.3 Schematic diagram of the in-situ optical measurement of an OLED in a vacuum chamber.

sample. The light is fed into a photo-spectrometer by the fiber, and the EL spectrum of the OLED is thus obtained. A calibration is made by comparing the peak intensity of the EL spectrum $I_p(\lambda)$ (in counts) with the luminance value L (cd/m²) determined from the integrating sphere system for the same sample (both measurements are performed nearly simultaneously). It is found that a linear relation exists, e.g., the value of luminance can be given by the relation *L (cd/m²)* ≈ *I_p (count)/35.2* for a sample geometry of 2.5 × 2 mm. Since we have specific sample geometry (2.5 × 2 mm or 2.5 × 4 mm) as well as specific measurement geometry and conditions (set-ups of the spectrometer), the luminance value for a given sample can be determined directly by the peak intensity of the EL spectra measured in situ.

OLEDs are mainly characterized by three efficiency values:

(1) Luminous efficiency (η_p), or power efficiency (in lm/W) gives the ratio of the total light output in lumens to the electrical power in Watts

(2) Current efficiency (η_c, in cd/A) is the ratio of the luminous intensity in forward direction and the current flowing through the OLED (the value is the same as the luminance divided by the current density).

(3) Quantum efficiency (η_q, in %) is defined as the ratio between the number of emitted photons and the number of injected electrons.

Assuming a Lambertian emission at the operating voltage V, the luminous efficiency of an OLED can be calculated by

$$\eta_p = \frac{\psi_V}{P_{in}} = \frac{\pi L \cdot \Delta S}{P_{in}} \tag{2.8}$$

It is related to the current efficiency η_c by

$$\eta_p = \frac{\pi}{V} \eta_c \tag{2.9}$$

The quantum efficiency is given by

$$\eta_q = \frac{\psi_e / E_{mean}}{I_{in} / e} \qquad \text{where } \psi_e = 683 \int_{380nm}^{780nm} \psi_e(\lambda) d(\lambda) \tag{2.10}$$

E_{mean} is the average photon energy in a first order approximation related to the wavelength of emission peak λ_{max} by $E_{mean} = hc/\lambda_{max}$. P_{in} and I_{in} is the input power and input current in the EL device, respectively.

2.2 Electrochemical method

The electrochemical method is a powerful tool to study oxidation-reduction processes and the electronic properties of organic molecules (or layers) and polymers. The author will give at first a brief introduction of the electrochemical process and system, followed by some examples of its application for the preparation of OLEDs.

2.2.1 Electrochemical processes and system

The electrochemical processes are concerned with the charge-transfer reactions at the electrolyte/electrode interface. In a typical electrochemical cell as shown in Fig. 2.4[124], the overall chemical reaction is made up of two independent half-reactions on the Pt and AgCl/Ag electrode. Each half-reaction determines the interfacial potential difference at the corresponding electrode. Usually only one of these reactions is studied, and the electrode at which it occurs is called the *working electrode*. To focus on it, one standardizes the other half of the cell by using a *reference electrode* with a constant makeup and a fixed potential.
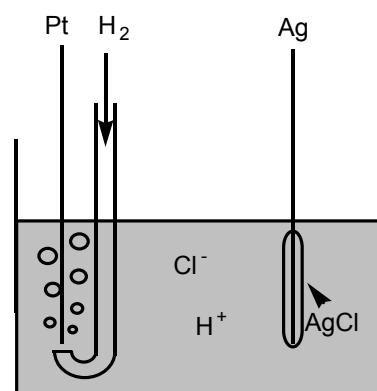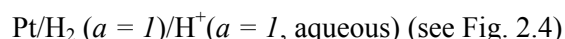

Fig. 2.4 A typical electrochemical cell: A Pt wire in a stream of H₂ and An Ag wire covered with AgCl in HCl. The cell is written schematically as Pt/H₂/H⁺, Cl⁻/AgCl/Ag. Source: Ref. 124.

The internationally accepted primary reference is the *normal hydrogen electrode (NHE),* i.e.

$$Pt/H_2 \ (a = 1)/H^+(a = 1, \text{aqueous}) \ (\text{see Fig. 2.4})$$

The electrode potentials are often measured and quoted with respect to other reference electrodes rather than to the NHE which is not very convenient from an experimental point of view. A common reference is the *saturated calomel electrode (SCE),* which is

$$Hg/Hg_2Cl_2/KCl \ (\text{saturated in water, at room temperature (RT)})$$
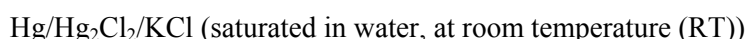
Its potential is 0.242V vs. NHE. Another reference electrode is the *silver-silver chloride electrode,*

$$Ag/AgCl/KCl \ (\text{saturated in water at RT})$$
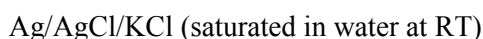
with a potential of 0.197V vs. NHE.

Sometimes, one should have an estimate of the absolute potential vs. the vacuum level, for example, the estimate of the relative potentials of metals and semiconductors based on their work function or the comparison of the energy-level data obtained by the electrochemical method with those from other approaches (e.g. UPS). The absolute potential of the NHE (vs. vacuum level) is estimated as 4.5 ± 0.1 eV based on a certain thermodynamic assumption[124], by which the standard potentials of other couples and reference electrodes are expressed in Fig. 2.5.

	E vs. NHE (volts)	E vs. Ag/AgCl (volts)	E vs. vacuum (volts)	E_F (Fermi level) (eV)
NHE	0	-0.197	4.5	-4.5
Ag/AgCl	0.197	0	4.7	-4.7
SCE	0.242	0.045	4.75	-4.75
$E_{1/2}(F_c/F_c^+)$	0.54	0.342	5.04	-5.04

Fig.2.5 Relation between the potentials on NHE, Ag/AgCl and absolute scale (vs. vacuum level), Source: Ref. 125.

In an electrochemical process (in Figure 2.6), when a more negative potential is applied to the working electrode (connecting an external power supply to the cell), the energy of electrons is raised. After they reach a level high enough to transfer into empty electronic states on the chemical species (A) in the electrolyte, the electrons start to flow from the electrode to the solution (*reduction,* see Fig. 2.6(a)). Similarly, imposing a more positive potential can

lower the energy of electrons, and electrons on the species will transfer to the electrode at some point (*oxidation,* see Fig. 2.6(b)). The critical potentials at which these processes occur are related to the standard potential, E^0. The E^0s of the A/A$^+$ and A/A$^-$ couples correspond in an approximate way to the highest occupied molecular orbital (HOMO) and the lowest unoccupied molecular orbital (LUMO), respectively.
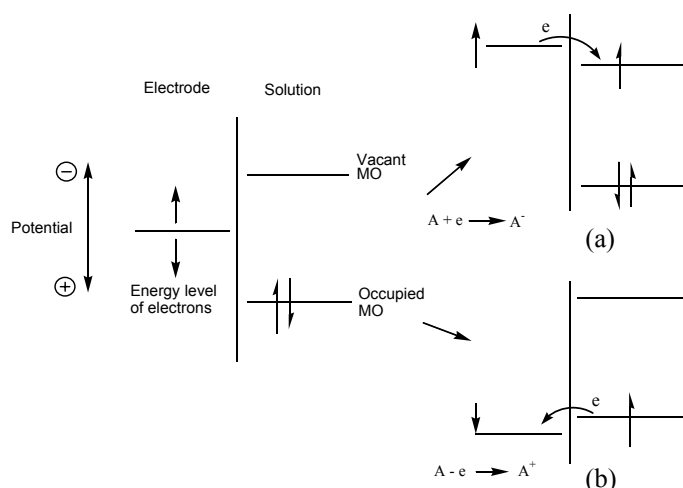

Fig. 2.6 Scheme of a reduction (a) and an oxidation (b) process of a species A in solution. The molecular orbitals (MO) of the species shown are the lowest unoccupied MO (LUMO) and highest occupied MO (HOMO). These correspond approximately to the standard potentials E^0s of the A/A$^-$ and A/A$^+$ couples, respectively. Source: ref. 124.

In the electrode reaction, the number of electrons (denoted by the total charge Q) across the interface is related stoichiometrically to the extent of the chemical reaction. The relationship between charge and amount of the product formed is given by *Faraday's law*, that is, the passage of 1F charges (F: Faraday constant) causes 1 equivalent of the reaction (i.e. consumption of 1 mole of reactant or production of 1 mole product in a one-electron reaction). The rate of the reaction

$$R(mol/s) = i/(nFA) \tag{2.11}$$

where n is the stoichiometric number of electrons consumed, A the electrode area and *i* is the current.

The information about the electrode reaction can be obtained from a current-potential (*i vs. E*) curve.

Since the existence of the solution resistance R_s, in the experiments in which iR_s may be high (e.g. involving the non-aqueous solution with a low conductivity), a three-electrode cell (shown in Figure 2.7(a)) is the standard electrochemical system up to date. In such a cell, the current is passed between a working electrode and a counter (or auxiliary) electrode, and the

desired potential is applied between the working electrode and a reference electrode by a potentiostat. This arrangement prevents the reference electrode from being subjected to large current that could change its potential. Furthermore it minimizes the contribution from the voltage drop iR_s to the electrode potential measured.
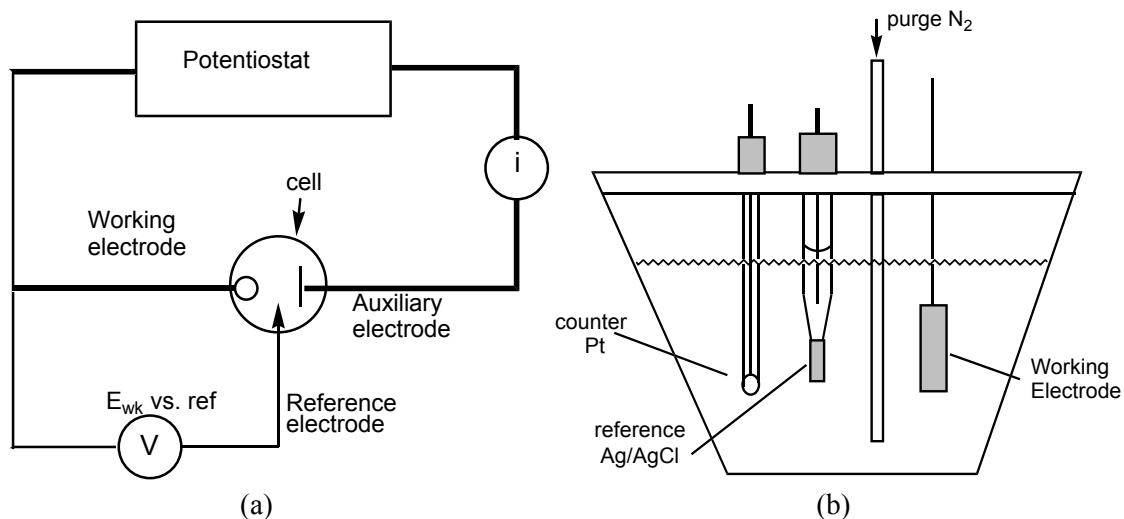

Fig. 2.7 A three-electrode cell: (a) scheme, (b) cell used in our experiment.

Figure 2.7(b) illustrates the cell used in our experiments. It consists of a glass container with a cap having holes for introducing the electrodes and nitrogen. Provision is made for oxygen to be removed from the solution by bubbling with N_2. Then the cell is maintained oxygen-free by passing N_2 over the solution. The reference electrode is an Ag/AgCl electrode, which is immersed into a tube of an internal solution (0.1 M $N(B_u)_4PF_6$ in acetonitrile) and isolated from the sample solution by a salt bridge. The potentials given in this work were calibrated by the formal potential of ferrocene (half-wave potential of F_c/F_c^+ couple, see Section 2.2.2), which has a constant potential of 0.352 V relative to a saturated Ag/AgCl electrode in an aqueous solution. The auxiliary electrode is platinum.

2.2.2 Voltammetry

The voltammetric method is the most commonly used electrochemical method, in which a controlled potential is applied to an electrochemical cell and the resulting current is measured. Various types of voltammetries have been developed which differ in the type of potential excitation waveform (e.g. potential step or potential sweep) and the state of the solution (quiescent or flowing) in the cell.

One key feature in voltammetry is the relationship between the potential applied and the concentration of the redox (reduction-oxidation) species at the electrode surface. Considering

a cell at open-circuit state ($i = 0$), the working electrode will keep equilibrium with the solution and exhibit an equilibrium potential E_{eq} related thermodynamically to the bulk concentration of the redox couple. It is assumed that the solution contains an oxidized species O which can be reduced to species R at the electrode according to

$$O + ne \Leftrightarrow R \tag{2.12}$$

If the charge-transfer electrode process is very fast (called *reversible system*), the potential of the electrode E is related to the concentrations of species O and R at the electrode surface (denoted as C_o^s and C_R^s, respectively) by the Nernst equation

$$E = E^{o'} + \frac{RT}{nF} \ln\left(C_o^s \middle/ C_R^s \right) \tag{2.13}$$

where $E^{o'}$ is the formal potential of the couple. (R: gas constant, T: temperature).

The change in surface concentration due to electrode reaction will lead to a concentration gradient and thus to a mass transfer between the solution and the electrode surface. A Nernst diffusion layer with a thickness δ exists near the electrode surface. In a reversible system, the ratio of electrode reaction is governed by the rate of mass transfer of the electroactive species, and the latter is proportional to the concentration gradient at the electrode surface. The current is therefore described by:

$$i(t) = nFA\left[D_o \left. \frac{\partial C_o}{\partial x} \right|_{x=0,t} \right] \tag{2.14}$$

In the case of a stirred solution (with a fixed δ), the Eq. (2.14) is approximated as

$$i(t) \approx nFAD_o \frac{C_o - C_o^s}{\delta} \tag{2.15}$$

where D_o is the diffusion coefficient of species O, C_o is bulk concentration of species O and x the distance from the electrode. The voltammogram (current-potential curve) of a fixed electrode can be derived by combining Eqs (2.13) and (2.14).

In the general cases where the interfacial charge-transfer kinetics is not so rapid (i.e. quasi-reversible system), the current-potential curve will be obtained by the Butler-Volmer equation[124]

$$i = FAk^o\left[C_O^s e^{\frac{-\alpha nF(E-E^{0\#})}{RT}} - C_R^s e^{\frac{(1-\alpha)nF(E-E^{0\#})}{RT}} \right] \tag{2.16}$$

where k_o is called the standard rate constant and α is the transfer coefficient.

In the following, the operation principle is given briefly for two types of voltammetric methods, which are employed in our experiments.

Potential sweep methods

A typical voltammogram obtained by scanning the potential in the stirred solution is shown in Fig. 2.8[125]. The shape of the curve can be understood by considering the slope of the concentration-distance profile. As the slope increases due to the decreasing of C_o^s, the current increases. A limiting cathodic current i_{lc} reaches when surface concentration C_o^s becomes zero ($i_{lc} = \dfrac{nFAD_oC_o}{\delta}$). The value of half-wave potential $E_{1/2}$ (the potential at which the current is equal to $i_{lc}/2$) is related to $E^{0'}$ of the redox couple. Thus $E_{1/2}$ can be used for the qualitative identification of chemical species.
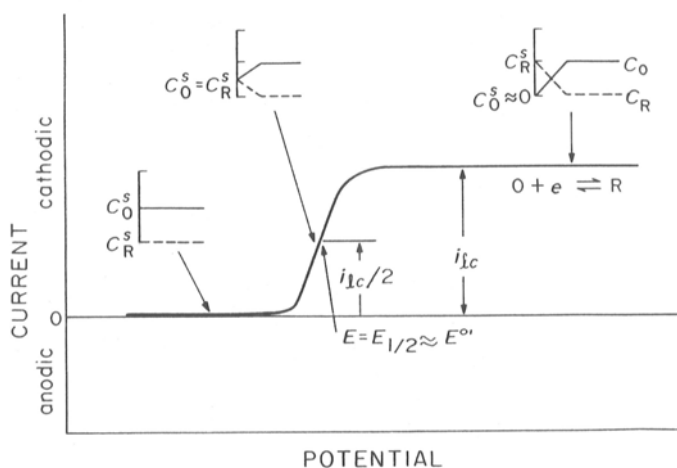

Fig. 2.8 A voltammogram with a representative concentration-distance profile in a stirred sloution. Source: Ref. 125.

Cyclic voltammetry (CV) is a very versatile technique among voltammetric methods. The CV measurement is performed in an unstirred solution by cycling the electrode potential and measuring the resulting current in the forward and backward direction. The controlled potential is a linear potential scan with a triangular waveform (inset of Fig. 2.9).

Fig. 2.9 provides an example of a CV for an ITO working electrode in a solution containing 1.0 mM ferrocene (F_c) as electroactive species and 0.1M N(Bu)$_4$PF$_6$ as supporting electrolyte in acetronitrile. The potential is scanned positively from 0 V. When it is sufficiently positive to oxidize F_c, an anode current takes place (shown at *b*) due to the electrode reaction

$$F_c - e \rightarrow F_c^+ \tag{2.17}$$

The current increases rapidly until the concentration of F_c at the electrode surface approaches zero, and the current peaks at *d*. Then the current decays as the solution surrounding the electrode is depleted of F_c due to its electrolytic conversion to ferrocenium

F_c^+. The scan direction is reversed at f. When the electrode potential becomes negative enough, the F_c^+ accumulated near the electrode will be reduced ($F_c^+ + e \rightarrow F_c$). The cathodic current rapidly increases until the surface concentration of F_c^+ approaches zero and the current peaks.
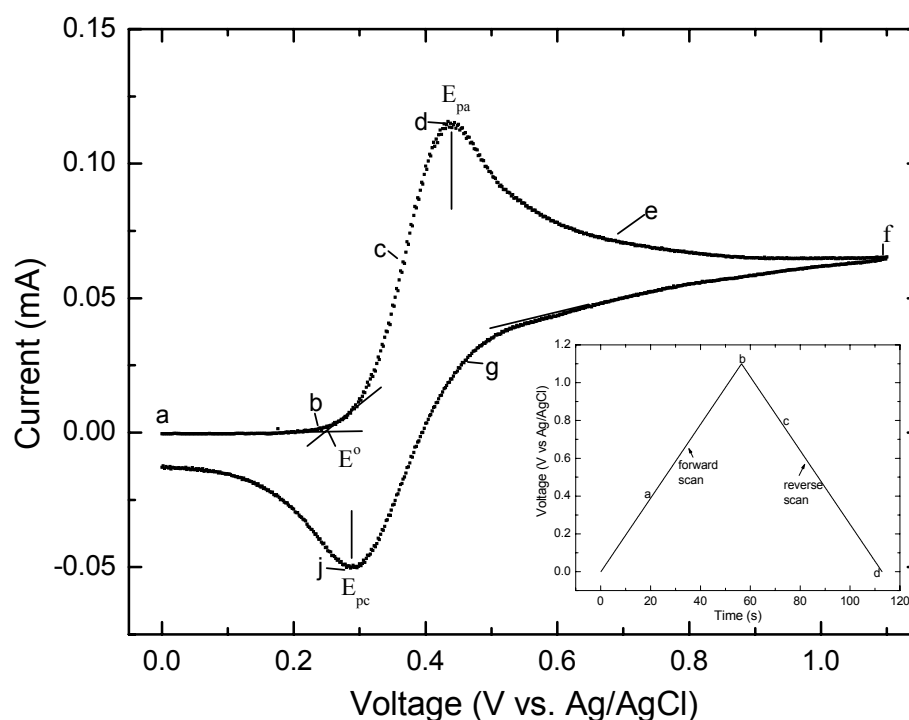

Fig. 2.9 Cyclic voltammogram (CV) of 1 mM ferrocene (F_c) in 0.1 M N(Bu)$_4$PF$_6$/acetonitrile solution. The scan starts at 0 V vs. Ag/AgCl electrode at a rate of 20 mV/s. Inset: excitation signal for the CV. The F_c/F_c^+ couple is used for the calibration of the potentials in our study (its half-wave potential (formal potential) $E_{1/2}$ has a constant value of 0.352 V vs. aqueous Ag/AgCl.

A detailed understanding of the CV curve can be gained by considering the Nernst equation (in a reversible system) or generally the Butler-Volmer equation as well as a diffusion-controlled mass transfer process near the electrode.

Since CV can generate rapidly the new redox states during the scanning, it is very useful in obtaining information about the complicated electrode reaction. The important parameters in a cyclic voltammogram are the anodic peak potential (E_{pa}), the cathodic peak potential (E_{pc}), the anodic peak current (i_{pa}), the cathodic peak current (i_{pc}) and the formal potential $E^{o'}$ of the redox couple. For the electrochemical reversible couple, the formal potential, $E^{0'}$ is given by

$$E^{o'} = \frac{E_{pa} + E_{pc}}{2} \tag{2.18}$$

The anodic (cathodic) peak current $i_{pa} = i_{pc}$ is proportional to $C_o v^{1/2}$, where v is the scan rate.

Potential step methods

In such methods, the electrode potential applied is a series of single potential-steps (called *potentiostatic*) or a sequence of the potential steps with different shape. For example, in the basic experiment of chronoamperometry, the current *i(t)* as a function of time is recorded corresponding to each potential step. By sampling the current at a fixed time τ during each of potential step experiments, the sampled current *i(τ)* vs. the potential can be obtained, which is called sampled-current voltammetry. The potential step methods are extensively used in the studies on the growth stages and growth mode of electrodeposited conducting polymers, as well as in the electrochemical doping process of the polymers (see Chapter 5).

2.2.3 Some applications to organic semiconductors.

2.2.3.1 Determination of the energy levels of organic semiconductors

As illustrated in Figure 2.6, the HOMO and LUMO levels are related with the standard potential E^0s of an organic molecule in the oxidation and reduction process, which is manifested in the CV curve as the onset of the oxidation peak and onset of the reduction peak, respectively. Thus the solid-state ionization potential (IP, the energy difference between the HOMO level and vacuum level) and the electron affinity (EA, the energy difference between the LUMO level and vacuum level) can be determined by the following relations[126, 127]

$$E_{onset}^{ox} = IP - 4.7(eV)$$
$$E_{onset}^{red} = EA - 4.7(eV)$$

(2.19)

where E_{onset}^{ox} and E_{onset}^{red} are the onset potentials of the oxidation and reduction versus Ag/AgCl reference electrode (4.7 eV vs. vacuum level seen in Fig. 2.5). The bandgap E_g (electrochemical) is derived by $E_g = IP - EA$. The values of these parameters determined by CV measurement can be compared directly with those obtained by other methods (e.g. UPS (for IP). However due to excitonic effect such E_g is not equal to the optical bandgap measured by UV-vis absorption spectra). In our measurements, a thin layer of the polymer (e.g. polythiophene) or a layer of organic molecules (e.g. NPB) is coated onto an ITO electrode, serving as a working electrode. However, the situation is complicated by a number of factors. For example, in an electrochemical oxidation, the negative counter-ions from the electrolyte must diffuse into the layer to maintain electrical neutrality. The presence of such counter-ions

can significantly alter the structure of the layer and hence alter the electronic properties. Since the onset of the oxidation is not sharp, it is often not clear which point on the CV curve should be taken as the ionization potential. Usually, the onset potential is determined from the intersection of the two tangents drawn at the rising current and background charging current in the CV. (see the E^0 point in Fig. 2.9)

2.2.3.2 Electrochemical synthesis of polymers

Electrochemical polymerization is a very important method for the preparation of conducting polymers. The process is based on the oxidation reaction of aromatic monomers (e.g. pyrrole[111,128], thiophene[129,130], carbazole[111] and their derivatives[131-133,116]) in the electrolyte. The product is the film on the electrode. The mechanism of the eletropolymerization is generally shown in the schematic Figure 2.10(a): (a) oxidation of the
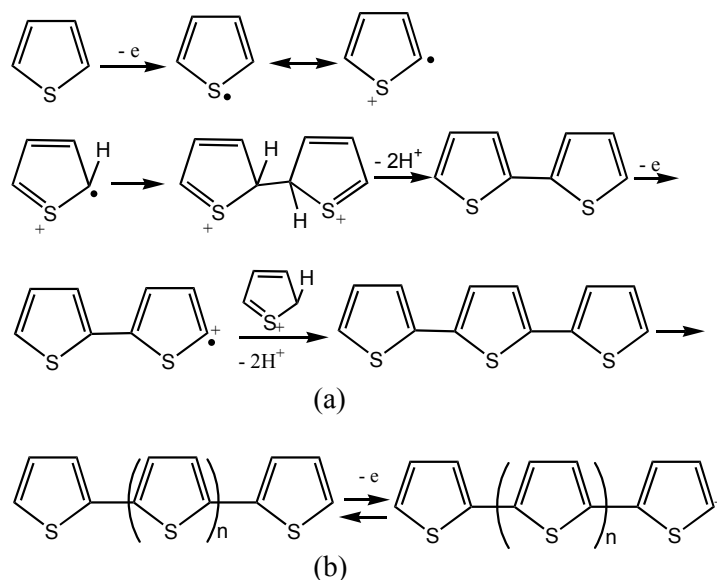

(a)

(b)

Fig. 2.10 (a) Schematic process for the electropolymerization of thiophene (b) Reversible electroactive behavior of polythiophene in the potential cycle.

monomer to a radical cation (by an applied potential near the oxidation potential of the monomer). (b) dimerization of the radical cations by the coupling reaction. (c) proton loss to yield a neutral dimer. (d) oxidation of dimer to its radical cation. (e) reaction of dimeric radical cation with another radical cation.., and (x) formation of oxidized conducting polymer.

The electropolymerization is usually carried out in a three-electrode cell. The potential of working electrode is applied by a potential step or a potential scanning. In our study we adopt the potential scanning. The growth can be controlled at a very low rate, which will benefits for the layer morphology. The basic parameters determining the properties of the polymer include the type and the concentration of monomer and counterion as well as the type of solvent[134-135].

The nature of the working electrode (e.g. stability and surface morphology, etc.) is also of importance[111]. In addition, other factors (e.g. growth temperature and the magnitude of the potential) can have a strong influence on the morphology and conductivity of the layer[136]. These parameters have to be optimized to produce the polybithiophene thin layers with well-defined structural and electrical properties for the hole-injection contact in OLEDs (see Chapter 4).

In the conducting form, the electrochemically-prepared polymer contains anions that are affiliated with the positively- charged polymer chains. The amount of charge within the polymer determines the level of the oxidation (doping level). Many types of polymer films are electroactive and can be switched between a neutral and nonconducting state (the reduced state) to an oxidized and conducting state (the doped state) (see Fig. 10(b)). Therefore the doping level can be adjusted during the redox cycle. In Chapter 5, we will utilize this approach to modify the work function by the adjustment of the doping level of the conducting polymer PEDT:PSS, which is performed by the potentiostatic electrolysis of the polymers.

3. Preparation of OLED structures

3.1 High vacuum system for OLED preparation

The OLED samples were prepared in a single-chamber high vacuum (HV) system *Lab 500* (Leybold). The system is evacuated by a combination of a fore-vacuum rotary pump and a turbo molecular pump. The base pressure is about 4 x 10^{-7} mbar. The chamber can be equipped with up to 8 evaporation sources for the organic materials and metals that are sublimed in resistively- heated Mo boats. This configuration may result in an across-contamination for the different sources during the evaporation, which will lead to the electroluminescence quenching and leakage current in the device. Thus each source has been isolated from another by Al foil, which can eliminate effectively the effect mentioned above. The system has to be vented to exchange the sample and install the evaporation sources. quartz oscillators together with the control units (Leybold-Inficon) monitor the evaporation rate and layer thickness. The source-sample distance is 25 cm, much larger than the sample diameter (25 x 35 mm), to guarantee an even thickness of the layer over the whole sample area.

3.2 Materials and properties

The chemical structure of the molecules used in this study is given in Figure 3.1. Alq_3 acts as an emitter and electron transport material. It had been chosen for OLEDs in a broad volume of studies because of its high chemical stability and relatively high electron mobility. One of the best attributes of Alq_3 is its property to form a high-quality thin film upon vacuum deposition. However, the positively-charged state of Alq_3 is chemically unstable which will be disadvantageous for the long-time reliability of the device[137]. NPB and TPD are used as hole-transport layer. Their films (also Alq_3) are amorphous so that a smooth morphology can be achieved. We prefer the NPB in most cases of OLED preparation because its glass transition temperature (the temperature above which the layer is getting crystalline) is relatively high (95 °C, compared to 65 °C for TPD). The crystallization is believed to be one of the major limiting factors for the device lifetime because it roughens the layer, which may result in the delamination of the contact. Table 3.1 lists some of the basic properties of these materials. The positions of the HOMO and LUMO level of the organic layers are especially important for OLEDs, Furthermore, the mobility of the majority carriers must be high for the electron

N,N'-bis(3-methylphenyl)-N,N'-bis-(phenyl)-benzidine (TPD)

tri(8-hydroxyquinolinato) aluminum
(Alq$_3$)

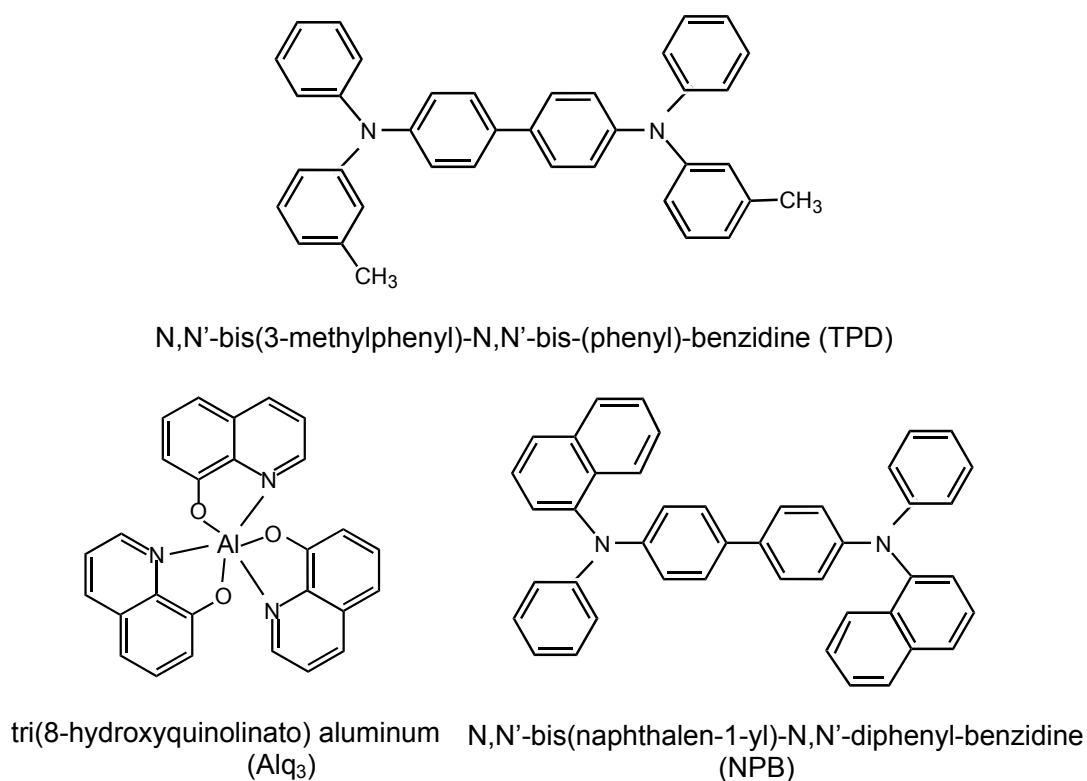N,N'-bis(naphthalen-1-yl)-N,N'-diphenyl-benzidine
(NPB)

Figure 3.1 Chemical structures of the materials used in OLED study

and hole transport materials. For the hole transport materials, the hole mobility is relatively independent on the electric field. However, the mobilities of electron and hole in the Alq$_3$ film are dispersive and strongly depend on the field and temperature (especially for the Alq$_3$ without purification by sublimation)[143,144], which has a substantial influence on the transport behavior in a high field.

Table 3.1 The properties of some materials which are relevant to OLED studies.

Material	Supplier	HOMO	LUMO	Mobility (at RT)	Density	Other
TPD	Syntec	5.4 eV[138]	2.4 eV[138]	$\mu_p \sim 1 \times 10^{-3}$ cm²/Vs[9] $\mu_n \ll \mu_p$	1.3 g/cm³	Amorphous layer, T_g = 65 °C*
NPB	Syntec	5.7 eV[139,140]	2.6 eV[139,140]	$\mu_p = 1/2\ \mu_{p,\ TPD}$[9] $\mu_n \ll \mu_p$	1.3 g/cm³	Amorphous layer, T_g = 95 °C
Alq$_3$	Syntec	6.0 eV[139,142]	3.3 eV[142]	$\mu_n < 5 \times 10^{-5}$ cm²/Vs[9,141] $\mu_n \ll 0.01\ \mu_p$[143]	1.3 g/cm³	Amorphous layer, T_g = 170 °C

* T_g: glass transition temperature

3.3 Procedure and characterization

Figure 3.2 shows the schematic structure of a multilayer OLED (upper scheme) as well as its geometry and preparation steps (lower scheme). Indium-tin oxide (ITO) acts as the anode. The work function of ITO depends strongly on the surface treatment and varies in the range of 4.2 eV to 4.9 eV[58,145-146]. The ITO substrates used here were delivered from Merck (Germany) with a sheet resistance of 15 Ω/□. The work function is about 4.3 eV from UPS measurement (Dr. Peisert, IFW Dresden), and surface roughness (rms) is 1.5 nm determined by AFM. For OLED fabrication, the ITO- covered glasses were patterned by etching with HCl (10 wt %) solution after protecting the active area with a commercial resist (Opticlean). For the cleaning, the patterned substrates were scrubbed in a detergent (Fit, *ca.* 4 vol. %) to remove the dust and imperfections from delivery and cutting, and then boiled in 1,1,1-trichloroethane, finally rinsed ultrasonically in acetone followed by ethanol and dried in flowing nitrogen gas to remove the organic contaminations.
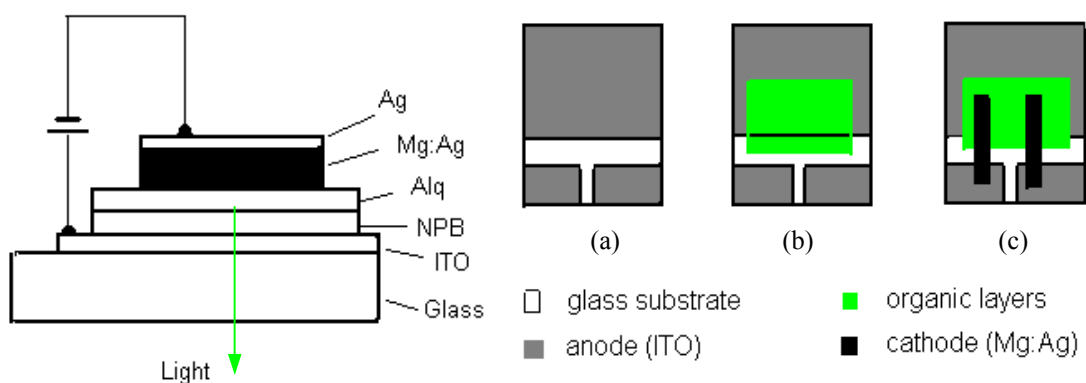

Fig. 3.2 (left) Schematic structure of a mutilayer OLED device. (right) The geometry and preparation steps of the mutilayer OLED: (a) substrate with a patterned indium-tin oxide (ITO), (b) after the evaporation of the organic layers, (c) with the cathode (Mg:Ag). The overlap of the ITO, the organic layer and cathode determines the active area of OLED.

Prior to the first cycle of the evaporation, each of the sources with newly-filled materials was degassed extensively in high vacuum for several hours by increasing the heating current gradually, and then the pre-evaporation at low rate was performed for each source. This process can guarantee that the evaporation afterwards is carried out at a good vacuum environment (4-5 x 10^{-7} mbar for the organics and 5 x 10^{-7} to 1 x 10^{-6} mbar for metals) even after the sources are exposed to air for sample transportation. Therefore it will benefit the purity of materials and the quality of deposited films. Upon evaporation, the heating current was increased by small steps and it took at least 20 minutes to reach the evaporation temperature in order to guarantee a uniform temperature distribution in the boat with the material inside. The hole transport layer and the Alq_3 layer were deposited successively with a

thickness of 60-100 nm for each layer. A mixture of Mg and Ag (10:1) was used as the cathode and deposited by co-evaporation of Mg and Ag. Its work function is 3.7 eV[147]. Typical evaporation rate is 1.5-2.3 Å/s for organic materials and 2-3 Å/s for metals. The calibration of the layer thickness (and the determination of geometry factor) was carried out by comparing the thickness value of a test film displayed on the quartz oscillator with that measured using an atomic force microscope (AFM, Nanoscope III, Digital Instruments).

The electrical and optical properties of OLEDs were characterized in situ or in N_2 atmosphere. Current-voltage (I-V) characteristics were measured by a Hewlett-Packard 4140B semiconductor parameter analyser. The electrical sample-contacts were connected by Cu tapes, allowing the preparation of two complete samples on one substrate. The EL spectra were recorded using a Sentronic S2000 optical spectrometer (Sentronic, Germany). The luminance (cd/m²) was calculated from the intensity of the EL spectra measured through an optic fiber system in situ (see Fig 2.3) or by an integration sphere in the atmosphere of N_2 using a calibrated source as the reference (see Fig 2.1).

3.4 Transport and electroluminescence (EL) features

Figure 3.3 shows the EL spectra from a NPB/Alq_3 OLED device. The emission peak is at 530 nm (2.35 eV). From the optical absorption edges of the Alq_3 layer, the apparent band gap is estimated to be 2.7 eV. There exists a red shift of the EL spectra from the Alq_3 absorption, which may be interpreted as the Frank-Condon shift resulting from the large conformational energy changes on the optical excitation.
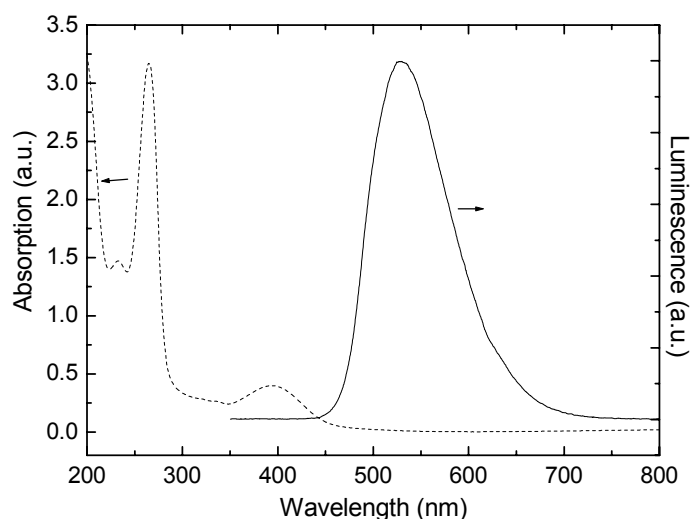

Fig. 3.3 UV-vis absorption spectrum of Alq_3 and the electroluminescence spectrum of the NPB/Alq_3 device. The Alq_3 layer is deposited on a quartz substrate and has a thickness of 200 nm.
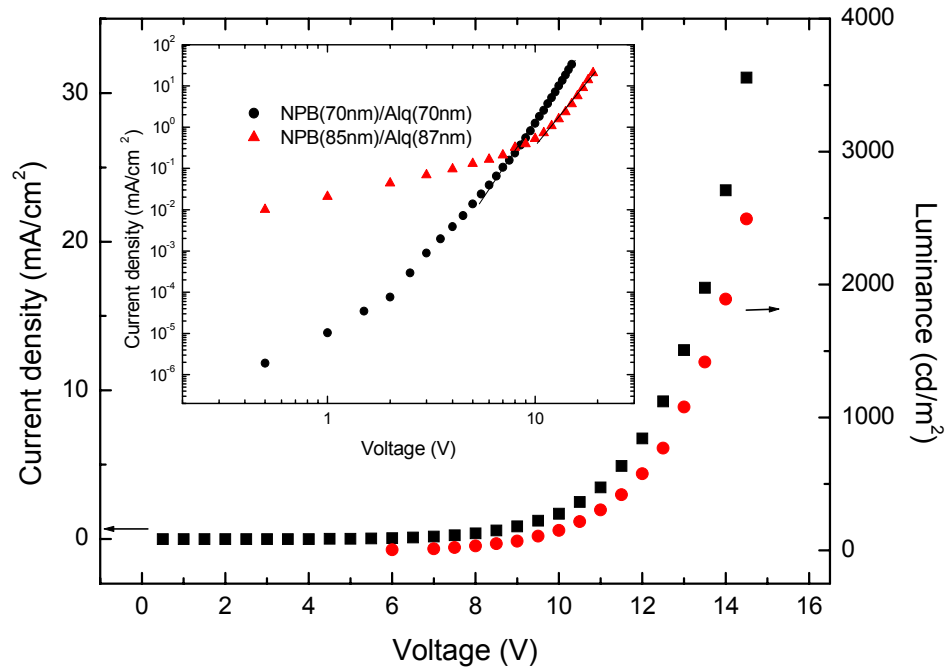
Fig. 3.4 Current-luminance-voltage (I-L-V) characteristic of a pristine OLED device with a 70 nm of NPB and a 70 nm of Alq$_3$. The inset shows the log-log plot of the I-V curves for two devices with different thickness of the organic layers. Both samples were run in air for a short time then characterized at the atmosphere of N$_2$

A typical current-luminance-voltage (I-L-V) characteristics of a pristine OLED is shown in Fig. 3.4. In the log-log plot (Inset of Fig. 3.4), the I-V curves can be fitted with a power- law relation $I \propto V^m$. At high electric fields, the factor m is 7-8, is in good agreement with the prediction of a trap-limited space charge transport. In the prediction, the current is given as: $I \propto \dfrac{V^m}{d^{2m-1}}$, d is the thickness of the organic layer and $m = \dfrac{E_t}{k_B T}$, E$_t$ is the chara-

Table 3.2 Performance of pristine OLEDs with different thickness of the organic layers.

Type of samples	Type 1	Type 2
External quantum efficiency (%)	0.444	1.566
Brightness (max) (cd/m²)	596[a]	2520[b]
Turn-on voltage (V)	9	5
Operating voltage (V) at 100 cd/m²	*ca.* 16.7	10
Luminous efficiency (lm/W)	0.909[a]	1.704[b]

Type 1: ITO/85 nm NPB/87 nm Alq$_3$/Mg-Ag/Ag
Type 2: ITO/70 nm NPB/70 nm Alq$_3$/Mg-Ag/Ag
a. At the applied field of 19 V
b. At the applied field of 14.5 V

cterristic energy in an exponential trap distribution. Since NPB is trap-free, the current should be controlled by trap-limited transport of electrons in Alq_3[148,16]. At low fields, the situation is more complex: m values of 1-2 are obtained, thus several factors such as the carrier injection/transport and the leakage current are involved. Table 3.2 summarizes the performance data for two types of the devices. They show a high turn-on voltage of more than 5 V and an operating voltage of more than 10 V as well as a low luminous efficiency, which is attributed to an inefficient charge injection from the anode due to a very large hole-injection barrier (~1.2 eV).

3.5 Current instability

When initially operating OLEDs, some of the freshly-prepared devices are short-circuited (with a resistance of several tens to several hundreds ohms). After briefly running a current of several tens of milliamps through the device, however, the short circuit opens and the devices emit light. During the operation in vacuum or in the atmosphere of dry N_2, a noisy leakage current always exists. Figure 3.5 shows a commonly-observed noisy current-voltage behavior of the NPB/Alq_3 device (in HV) in which a large leakage current is found in the low field (< 6V). Meanwhile the shape of the I-V curve in the low field can also vary between the different voltage sweeps. However, the L-V feature does not show such an anomalous behavior. On the
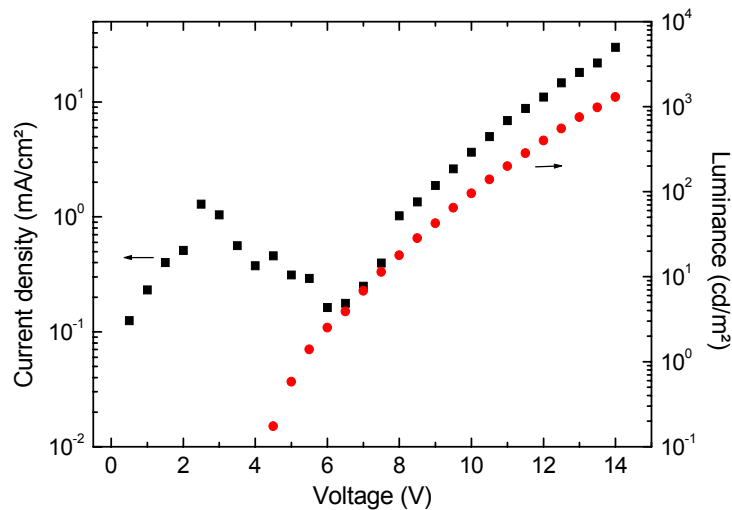
Fig. 3.5 L-I-V characteristic of an OLED device showing a leaking current in vacuum.

other hand, increasing the thickness of the organic layers up to 250 nm can eliminate effectively the probability of appearance of the current instability. The phenomena, observed also by other groups in various types of OLEDs[149-151], indicate the formation of microscopic conduction paths through the organic layers; the large paths can be burnt out by the

application of high current. The existence of the paths suggests that inhomogeneities exist at the organic/electrode interface, which may lead to a non-uniform electric field across the device. At some spatial points, very high local electric field will result in the high current 'hot-spots' in the low field. When the onset voltage of the EL is reached, the charge injection at the electrode increases and the current becomes more homogenous. The effect of current instability will be eliminated.
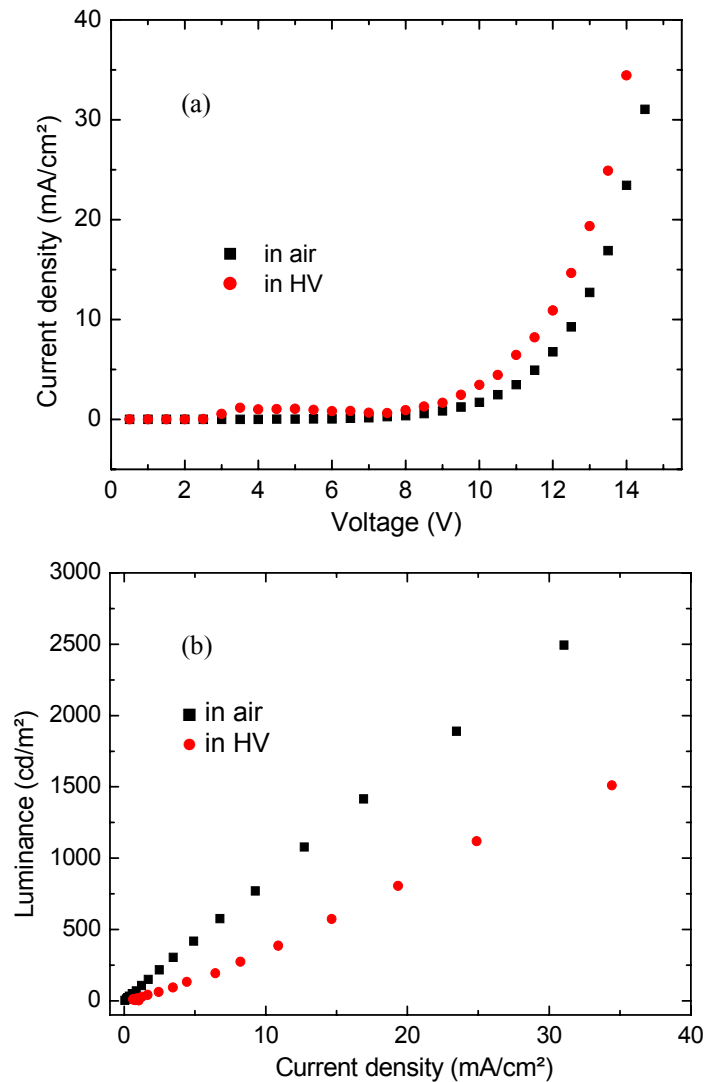
Fig. 3.6 (a) current density vs. voltage and (b) luminance vs. current density characteristics of an OLED measured in high vacuum and just after the sample is exposed to air.

The assumption mentioned above can be verified further by the observation of the behavior of OLEDs operating in air (see Fig. 3.6). The same devices show much less or even no leakage current (also see Fig. 3.4). Although the onset voltage of the EL increases slightly, the proportionality between the luminance and current density (equivalent to current efficiency) is

enhanced as shown in Figure 3.6 (b). The increase of the onset voltage is partly attributed to the increase of the contact resistance due to the oxidation of the cathode. However, the effect does not influence the luminance versus current-density characteristic because the contact resistance does not affect the current. The high current at the 'hot-spots' accelerates the oxidation of the metallic atoms of the cathode at these sites, which leads to a blocking of the microscopic conducting paths and thus to an elimination of the leakage current. The decrease of the leakage current will increase the part of the current that contributes to the EL and thus leads to an enhanced efficiency.

The origin of the interfacial inhomogeniety is not clear yet. However, since the organic layers deposited are homogenous and pinhole-free with a roughness of 1 nm, the particles and imperfections, pre-existing on the ITO surface or introduced during device fabrication, are the best candidates for the source. In this case, the evaporated thin organic layers do not cover fully the particles on the ITO surface, thus the cathode could come in contact with the ITO. A very high electric field will be formed locally around the imperfections and thus the leakage current could occur. The current instability could produce an intensive local Joule heating, which will be detrimental to the morphological stability of the device as well as cause the degradation of device efficiency.

Since the hole injection is inefficient and a strong current instability exists for the pristine molecular OLED, it will be necessary to improve the energetics and the contacts of the anode/organic interface by a modification of the ITO anode surface (see Chapter 1.5). This goal can be achieved by the introduction of a thin buffer layer between the ITO and the hole-transport layer if such buffer layer has a favorable energy level for easing the hole-injection as well as it can planarize the anode surface. This is just the motivation that we will utilize the charge injection contact for improving the performance of OLED in the following chapters.

4. Electropolymerized polybithiophene for OLED

4.1 Electrodeposition and characterization

In this chapter, an electrochemically prepared polybithiophene (PbT, Figure 4.1) is introduced as a hole-injection contact material for small molecular OLEDs. PbT offers some advantages as compared to other conjugated polymers[111, 130, 152]. First, it is highly stable in morphology and remains unchanged up to 350 ˚C in air. The glass transition temperature is high as well. Second, it is chemically and electrochemically stable in air, and it can keep electroactive in electrolytes during multiple redox cycles, what should benefit the operating stability of OLED devices.

Electropolymerization is a convenient and common method for the film growth of the polythiophene (PT) family. The films produced by this process are good candidates for the application of electrochromic displays[111]. However, the PT layers formed by electropolymerization process were usually not homogeneous enough for the purpose of device fabrication[153-154]. Here, it is demonstrated that well-defined smooth ultrathin layers of PbT can be formed electrochemically using the dimeric thiophene.

Poly(2,2'-bithiophene)
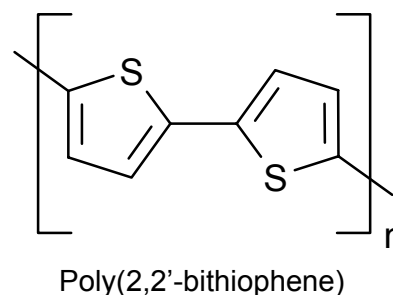
Fig. 4.1 Chemical structure of polybithiophene.

4.1.1 Growth condition and morphology

The synthesis of PbT was carried out by potential cycling between 0 V and 1.20 V (final potential is 0 V) in an one-compartment electrochemical cell. A program- driven potentiostat (HEKA) was used. The solution was 25 mM 2,2'-bithiophene (bT, Aldrich) in acetonitrile (Fluka) with 0.1 M tetrabutylammonium hexafluorophosphate ($N(Bu)_4PF_6$, Fluka) as supporting electrolyte. The ITO on glass substrate (Merck, 15Ω/□) served as the anode (working electrode). The reference and counter-electrode was Ag/AgCl and Pt, respectively. Prior to use, the patterned ITO-coated glass was cleaned extensively as described in Section 3.2. The electrolyte solutions were degassed by nitrogen bubbling for 15 min and a nitrogen atmosphere was maintained over the solution during the experiment in order to remove and avoid oxygen. After electrochemical preparation, the films were carefully rinsed with pure acetonitrile, then dried in high vacuum ($< 1 \times 10^{-6}$ mbar) for more than 12 h. The electrochemical properties of

the polymer films were measured by cyclic voltammetry (CV) in bithiophene-free N(Bu)$_4$PF$_6$/acetonitrile solution. The potentials given were calibrated by the formal potential of ferrocene and the values were given vs. aqueous Ag/AgCl electrode. The thickness of the films was measured by AFM as well as by a Sloan Dektak 3030ST surface profiler.

Figure 4.2 shows the electropolymerization of 2,2'-bithiophene (bT) by potential scanning. When the switching potential is in the range of the oxidation potential (E$_{pa}$) of bT (1.3V vs.
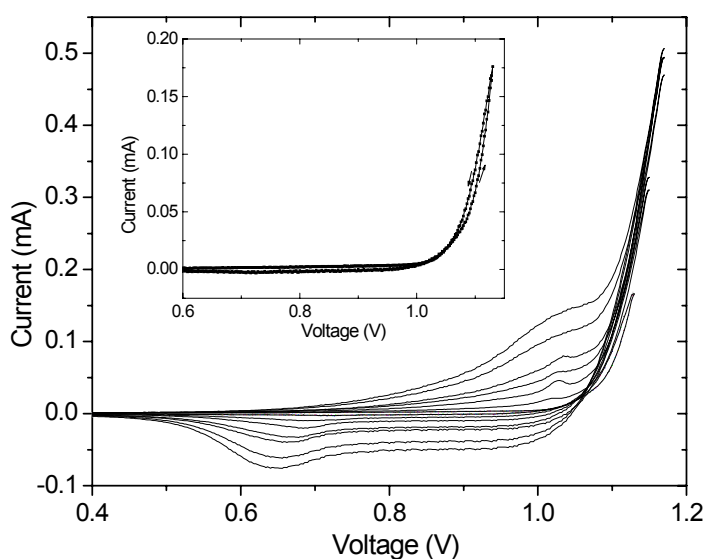

Fig. 4.2 Electropolymerization of a 25 mM bithiophene in 0.1 M N(Bu)$_4$PF$_6$/acetonitrile solution by potential cycling between 0 V and 1.2 V. Scan rate is 20 mV/s. The potentials are referred to aqueous Ag/AgCl electrode

Ag/AgCl), the bithiophene is electrooxidized and thus polymerized. The trace crossing on the reverse sweep (inset of Fig. 2) in first cycle is viewed as the proof of the start of the nucleation process of the polymer. Multisweep experiments show the increasing current from the redox process in each cycle, indicating a continuous growth of the film on the electrode. The polymerization proceeds easily even when a very low dimer concentration (about 0.01M of bT) is used. The resulting layer is homogenous, semitransparent (with a color of light orange), and in the neutral (undoped) state. The doped films can be obtained by applying a potential larger than 1.0 V on the working electrode (covered with a produced polymer layer) in the N(B$_u$)$_4$PF$_6$/acetonitrile solution.

In contrast, the electropolymerization of the thiophene monomer is much more difficult as compared to its dimer and results in a poor quality of the polythiophene layer with a rough morphology. Only a limited number of nucleation sites are formed during the initial stage. Moreover the polymerization current is much lower and the polymer grows as isolated nodules embedded in a thin continuous film. The difference in the film quality can be

explained by the electropolymerization mechanism. As illustrated in Section 2.2.3.2, the polymerization procedure is initiated by the coupling reaction of radical cations from the oxidation of the monomers, which results in the formation of dimers. Then by the reaction of the dimeric radical cation with another cation, oligomers and eventually a polymer is formed. A shorter reaction pathway will be reached if the polymerization is initiated by the coupling of dimeric radical cations. The density of the nucleation sites will thus increase dramatically which leads to a more homogenous film growth. The difference in the polymerization processes mentioned above can also be manifested by the much lower oxidation potential E_{pa} of bithiophene compared to E_{pa} of 2.06 V for thiophene (vs. Ag/AgCl)[130, 154].

The electropolymerization reaction involves the removal of about 2.25 electrons per molecule of bT[154]. Therefore the 'mass thickness' d of the resulting layer can be estimated from the electro-deposition charge Q (net charge in the redox process) using the following relation:

$$\left[\frac{Q}{2.25eN_o} \right] M_w = \rho S d \tag{4.1}$$

therefore

$$d \ (in \ nm) = 5.20Q \ (in \ mC/cm^2) \tag{4.2}$$

where N_o is Avogadro constant, M_W is the molecular weight and S is the active area of the working electrode. The density ρ of the PbT layer is assumed to be 1.5 g/cm³. Comparing the film thickness estimated from Eq. (4.2) with the actual thickness measured by AFM and the surface profiler, we find that the value of 'actual' thickness is about 70% of that of the 'mass thickness' in all cases. It means that some amount of the electrodeposition charge does not contribute to the film deposition.

a. Film morphology

The morphology and structure of the PbT films at different growth stages are determined by scanning electron microscopy (SEM) and AFM. Fig. 4.3(a) shows a SEM graph for a 20 nm thick undoped layer. The surface is homogenous and smooth, and does not present the irregular defects. At the enlarged view by AFM (Fig.4.3 (b)), the layer consists of the closed-packed fibres entangled with the granular structures; the surface root-mean-square (rms) roughness is about 6-7 nm. The surface roughness is also small than that of the PT thin layers electropolymerized from the thiophene monomers in the literature. When the layer thickness increases, the surface becomes more rough and irregular. At a thickness above 60 nm, the surface roughness increases more rapidly as shown in Fig. 4.4. The polymer structure is a
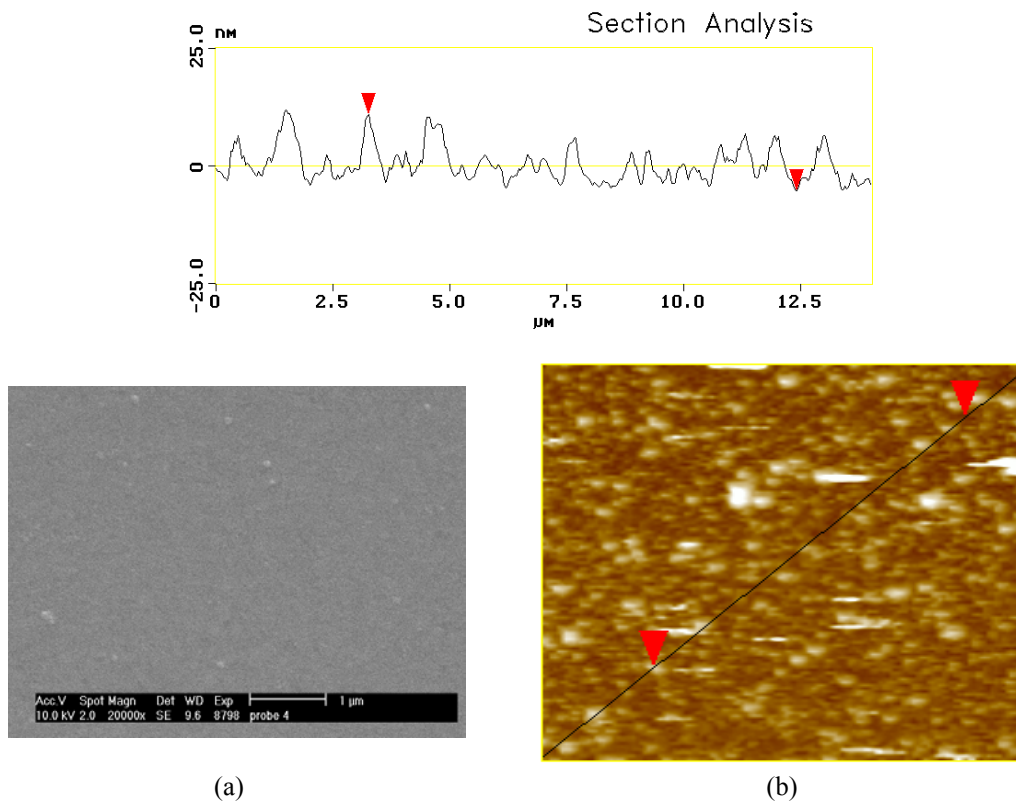
Fig. 4.3 (a) Scanning electron microscope (SEM) and (b) atomic force microscope (AFM) graphs of a 20 nm undoped polybithiophene (PbT) layer.

collection of cylinders with around 100-150 nm in diameter and different heights, grown perpendicularly on the flat underlying layer as found by the AFM observation. The surface
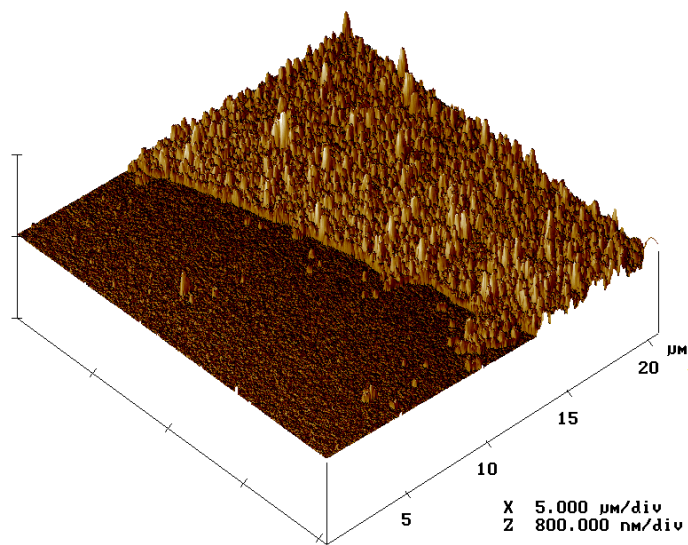
Fig. 4.4 AFM graph of an undoped PbT layer of 75 nm. The flat part in the left responds to the underlying ITO and the right part is the PbT layer grown on ITO.

roughness can reach 15-20 nm. The doped PbT layers show the same smooth morphology as the undoped ones at the low thickness (lower than 30 nm). However, at higher thickness the roughness is larger compared to the latter, which should be attributed to the swelling effect by the solvated PF_6^- dopants.

Our observation is consistent with the investigation of other authors on the growth stages of different kinds of polythiophene films. Chao et al.[115] confirmed that two different types of polymer layers are successively formed during the electrodeposition of poly(3-methylthiophene) (PMeT). In the first step of the layer growth (up to 30-40 nm), the film is a stack of dense parallel fibres in a layer-by-layer way, whereas the second layer is made of the aggregates of the granules arranged in a disordered way. By investigating the effect of the potential and monomer concentration on the nucleation and growth of PT, Schrebler[155] proposed that three nucleation mechanisms contribute to the growth process. The contribution from the two-dimensional (2D) instantaneous nucleation is important in the first stage of the nucleation process, indicating that the polymer deposition is initiated by the formation of a 2D film. The transition between the growth stages occurs at a larger thickness of the PbT layer as compared to the cases of PT's growth described by these authors, which is attributed to an improved electrodeposition condition here. Since the morphology of the PbT layer is poorly-defined at large thickness which is unfavorable to the device fabrication, only the ultrathin layer (less than 60 nm) will be used in most cases of the following device preparation.

b. Effects of growth parameters

The effects of dimer concentration, growth temperature as well as the concentration of supporting electrolyte on the growth rate and the structure of the PbT layer have been investigated. It is found that the role of anion seems not to be dominant. The I-V curve for the
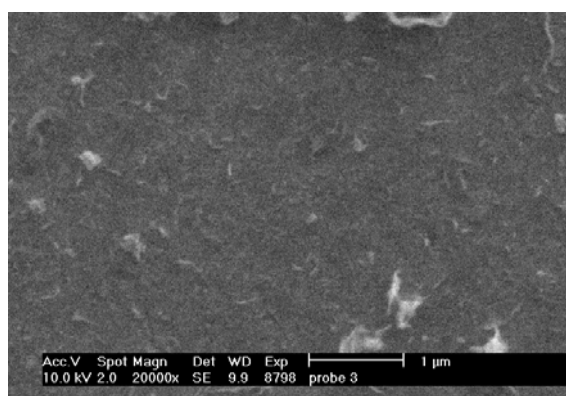

Fig. 4.5 SEM graph of a 22 nm PbT layer electrodeposited in the electrolyte containing 50 mM bT.

electropolymerization does not show a difference and the film morphology is nearly identical if PF_6^- is replaced by ClO_4^-. However, the concentration of dimer has a significant effect on the layer growth. Increasing the concentration of bithiophene from 25 mM to 50 mM leads to a more than three-fold enhancement of the anodic current in the I-V curve during the electropolymerization, which corresponds to a much higher growth rate of the layer. Moreover, the resulting films are much rougher and more irregular with lots of bright stripes on the surface as manifested in Fig. 4.5. This indicates that the fast polymerization is unfavorable to the film structure. Therefore a relatively low concentration of bT should be used to obtain a well- defined morphology.

   In addition, the electrodeposition of PbT was made in a low temperature cell (around –6 to – 8 °C). As expected, the growth rate is lowered as shown from a reduction of the polymerization current by 20-30 % in each of the potential scans compared to the case at room temperature (27 °C). However, the difference in the film structure is very small for both kinds of the layers in the same thickness. The surface roughness is reduced slightly for the layers fabricated at low temperature.

4.1.2 XPS results

   Figure 4.6 shows the XPS survey spectra of the undoped and PF_6^- doped PbT films with the thickness of 30 and 25 nm, respectively. For the undoped layer, an intensive and sharp carbon peak at 285 eV is associated with only one chemical state of C atom (the C-C bond and S-C bond are not well distinguished). The S 2p doublet ($2p_{1/2}$, $2p_{3/2}$) is resolved with an expected
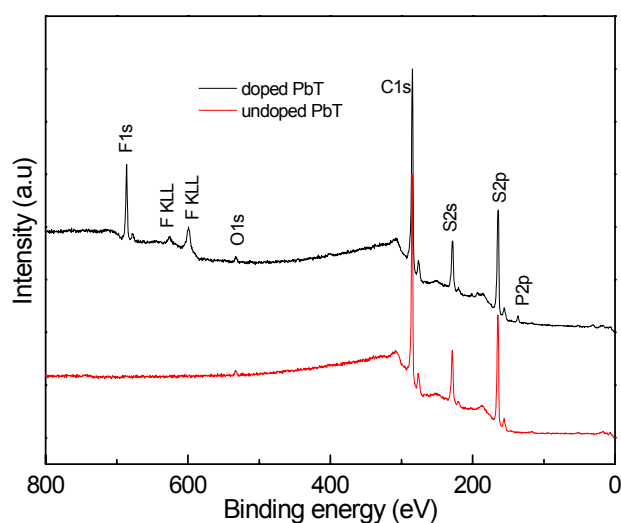

Fig. 4.6 XPS survey spectra of the PbT layers: undoped (30nm) and doped with PF_6^- (25 nm), respectively. Excitation source is Mg K_α.
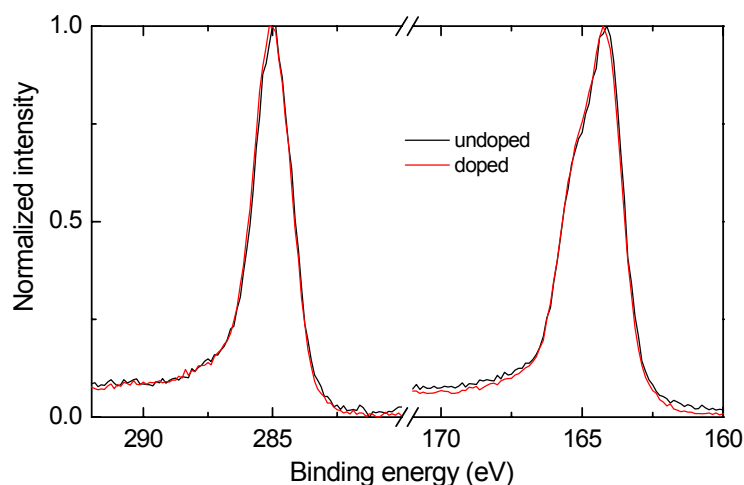
Fig 4.7 The C 1s and S 2p XPS spectra for an undoped and a doped PbT layer, respectively.

Table 4.1 Atomic concentration profiles in the PbT layers obtained from quantitative XPS analysis

PbT	C (%)	S (%)	F (%)	P (%)	O (%)	N (%)
undoped	78.02	20.33	0.18	0.08	1.28	0.3
doped	74.24	19.37	4.33	0.67	1.20	0.4

* Concentration analysis of C (O, F, N) and P (S) is made by their 1s and 2p peaks, respectively.

ratio of 2/3 (in Fig 4.7). Quantitative results of the atomic concentration listed in Table 4.1 agree well with the molecular structure of PbT: C_4H_2S (C: S = 4:1 in the atomic ratio). For the doped layer, the spectral data confirm the presence of PF_6^- anions from the appearance of F 1s and P 2s and P $2p_{1/2, 3/2}$ peaks. The concentration ratio of F and P is also consistent with the PF_6 structure and the doping level is estimated as 4.0 % from the quantitative analysis. However, the change of the C 1s and S 2p spectra (e. g. the energy shift) is very small upon the doping as shown in Fig. 4.7, which indicates that no charge is located on these two elements. The charge should thus be delocalized on the polymeric chain as suggested by Diaz[156]. In addition, the O 1s emission at 532 eV is very weak in both the doped and undoped PbT; the concentration of oxygen is around 1 at% (in Table 4.1). It decreases to 0.5% inside the layer found from the depth profile by Ar^+ ion sputtering, which indicates that the surface oxygen is attributed to the absorbed O_2 from air. Therefore we are able to obtain a very clean PbT layer from the eletropolymerization process with little chemical contamination.

To obtain the information on the depth distribution of the dopant anions, angle resolved XPS measurements have been carried out for the surface of the doped PbT. The inelastic mean free path of a photoelectron (λ) is estimated as 3 nm for the organic materials[157]. Since 95 % of the signal intensity comes from the layer underlying the surface with a thickness of the effective escape depth d:

$$d = 3\lambda \cos\theta \qquad\qquad (4.3)$$

where θ is the take-off angle of photoelectrons vs. surface normal, an information depth up to

10 nm can be reached. Table 4.2 shows the calculated atomic concentrations for the different acceptance angles, no distinct change is visible. It indicates that the elements from the dopant (F, P) as well as C and S are distributed homogeneously within a depth of 10 nm from the surface. The conclusion is confirmed further by the observation of the depth profile by Ar$^+$ sputtering.

Table 4.2 Atomic concentration profiles in a doped PbT layer obtained at different acceptance angles

ϑ (°)	C	S	F	P
30	74.11	19.98	4.85	0.92
45	75.12	19.93	4.04	0.83
60	75.14	19.65	4.29	0.86
70	75.92	19.50	3.90	0.67
80	80.09	17.04	2.52	0.65
15	75.06	19.80	4.02	0.83

ϑ: analyser take-off angle to sample normal

4.1.3 Electrochemical propertiess

Fig. 4.8 shows a cyclic voltammogram (CV) of the PbT film (10 mC, equivalent to a thickness of 50 nm) in 0.1 M N(Bu)$_4$PF$_6$/acetonitrile solution at different scan rates. The
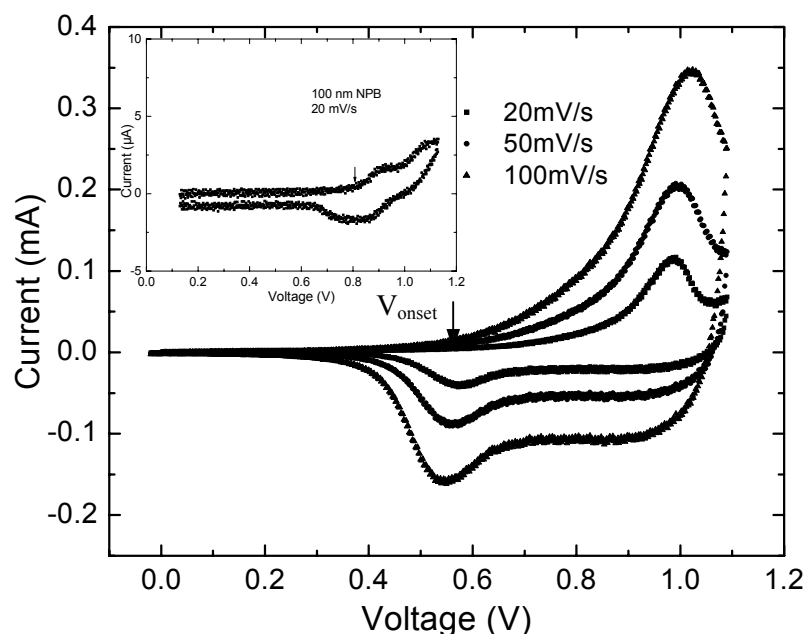

Fig 4.8 Cyclic voltammogram (CV) of a PbT film deposited on ITO in 0.1 M N(Bu)$_4$PF$_6$/acetonitrile solution. Inset: The CV of a 100 nm NPB layer on ITO. The reference electrode is Ag/AgCl.

voltammogram displays a peak potential for the oxidation at 1.05 V, followed by a flat reduction wave and a reduction peak at 0.55 V in the reverse sweep. The film can be cycled between the oxidized and reduced state without a distinct change in the CV, accompanied by a reversible color change from green-black to light orange.

The oxidation process (or doping) of the polymer (from 0 to 1.1V) corresponds to the transfer of electrons from the polymer to the ITO electrode, producing holes. Meanwhile anions diffuse into the polymer and form the anion-hole pairs to maintain electroneutrality. In the reverse sweep (reduction or dedoping), the anions are expulsed towards the electrolyte accompanied by a reorganization process of the polymer chains. The redox process in the PbT layer is nearly reversible, as manifested by the similar amount of the charge involved in the oxidation (Q_{ox} = 0.924 mC) and in the reduction (Q_{red} = 0.858 mC) processes. The anodic peak current (at E_{pa}) increases with the sweep rate.

The ionization potential (IP), equivalent to the HOMO level, was estimated for the PbT layer from the onset of the oxidation peak V_{onset}, as often applied in such studies[127]. Using the relation $IP = V_{onset} + 4.7$ eV (as shown in Eq. (2.19) of Section 2.2.3.1), the value of the IP for PbT is about 5.25 eV. We also measured the IP value of NPB (inset of Fig. 4.8), which is 5.5 eV. The HOMO level of PbT is thus located between the work function of ITO (*ca.* 4.3 eV as given in Section 3.2) and the HOMO of NPB. Therefore the PbT layer can act as a hole-injection layer between the ITO and the NPB.

In an electrochemical redox process, the Fermi level (E_F) of the polymer is defined by the setting potential (related to the equilibrium potential)[124]. Since the final potential (set at the end of the polymerization) is 0 V (vs. Ag/AgCl) in each potential cycling of the polymerization, the Fermi level of the undoped PbT will be at 0 V vs. Ag/AgCl while apart from the HOMO level by − 0.55 eV (within the band gap). The band gap of PT is 2.0 eV[158], the middle of the band gap is therefore at − 0.45 V vs. Ag/AgCl. It indicates that the undoped PbT is still a weak p-doped semiconductor because its E_F is 0.45 V below the middle of the band gap. Thus a small amount of free charge carriers exist within the layer. The increase of the final potential or the doping of the layer at the high potential will lead to a lower E_F and more free charge carriers.

The reproducible redox behavior of the PbT layer has confirmed the high electrochemical stability. The reduced state of the polymer remains very stable in air for a period of at least several months and the stored PbT still maintains electroactive if cycled in the electrolyte again, indicating a high chemical stability. However, its doped state shows a much lower stability. In the measurement of open circuit potential (OCP), the PbT layer oxidized at 1.2 V shows a decrease of the OCP value from 1.0 V to 0.65 V within 20 min. The procedure of

rinsing and drying results in a further reduction of the OCP caused by the decay of the doping level. Therefore only a low doping level (4 %) can be kept as verified from the XPS measurement.

The instability for the doped state is attributed to the high oxidation potential (*ca*. 1.0 V) of PbT, which lies close to the value for water (1.1 V). The doped PbT will be reduced slowly by the trace of water in the electrolyte or in air. On the other hand, the reduction potential of PbT is much higher than the value for O_2, so the undoped layer will not be oxidized by O_2 and thus is stable in air.

4.2 Effect on the hole injection and the OLED performance

4.2.1 Hole-only device

In order to investigate the influence of the PbT on the hole-injection at the organic/electrode interface, simple hole-only devices (i.e. with single-charge carriers) were prepared. In these devices, the organic layers are sandwiched between the ITO anode and the Ag cathode. Vapor deposition of silver was carried out at the pressure around 5 x 10^{-7} mbar with an evaporation rate of *ca*. 1 Å/s. The large work function of silver (4.3-4.4 V)[159] can reduce the electron injection into the LUMO level of the organic layer (PbT and NPB).

4.2.1.1 ITO/PbT/Ag structure

The inset of Fig. 4.9 shows the forward- biased I-V characteristics of two ITO/PbT/Ag devices with the undoped PbT thicknesses of 36 nm and 60 nm. Fig 4.9 (a) gives a plot of *ln(j) vs. V*$^{1/2}$ for the devices. A good linear dependence is found at a low bias ($\leq$ 3 V). It indicates that the I-V behavior can be described by Richardson-Schottky (R-S) thermoionic emission mechanism[32]. The mechanism is based on the lowering of the image charge potential by the external field $F = V/d$, d is the layer thickness. The current density j_{RS} is then given by

$$j_{RS} = A^* T^2 \exp(-\frac{\Delta_B - \beta_{RS}\sqrt{F}}{k_B T}) \qquad (4.4)$$

Here $A^* = 4\pi q m^* k_B^2 / h^3$ (*= 120 A/(cm²K²) for m* = m$_o$)* is the Richardson constant, $\beta_{RS} = \sqrt{q^3 / 4\pi\varepsilon\varepsilon_o}$, Δ_B is the zero-field injection barrier, ε the relative dielectric constant, and ε_o is vacuum permittivity. Assuming the validity of Eq. (4.4), a linear dependence of *ln(j)* as a function of $d^{1/2}$ is expected if the current data of the devices with the different thickness taken at the constant V are plotted. The data shown in Fig. 4.10 obey this prediction, demonstrating
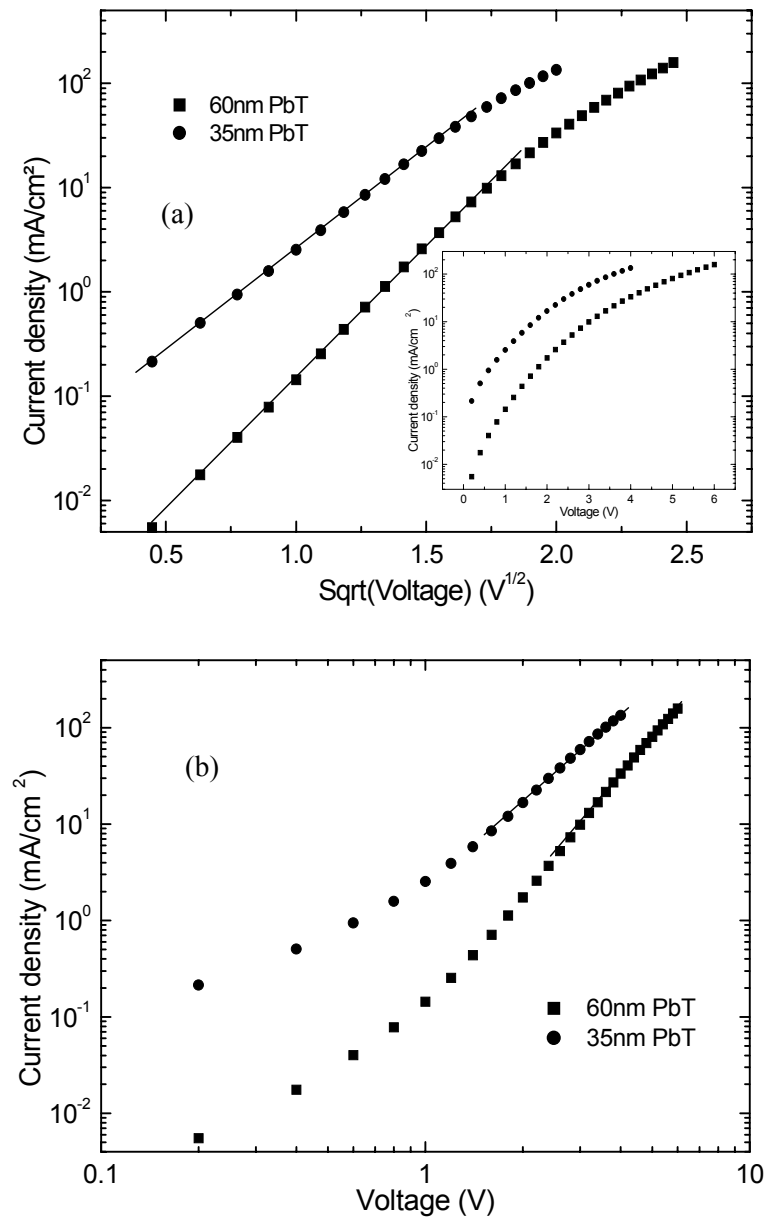
Fig 4.9 Current-voltage (J-V) features of two ITO/PbT/Ag devices with different PbT thickness plotted in the form (a) *ln(J)* as a function of $V^{1/2}$ and (b) the log-log representation. Solid lines: the linear fit. ITO is positively biased. Inset: the same I-V curves in a semi-logarithmic form.

that at low fields the charge-carrier transport behavior of such devices is injection-limited, i.e. there is a thermionic emission at the PbT/anode interface.

The barrier height for the hole-injection is estimated to be 0.7-0.75 eV derived from Eq. (4.4), consistent with the energy displacement (~0.90 eV) between the work function of ITO and the HOMO of PbT obtained from the electrochemical measurements. The lowering of the

barrier height may be attributed to the broadening of the energy levels of the PbT chains originating from the structural disorder in the organic semiconductor[160]. The value of the

dielectric constant ε is about 2.5 as calculated, which is in the range of the magnitude for most of PT materials. It is to be pointed out that, the built-in potential (V_{bi}), approximately the difference of the work function φ between ITO and Ag cathode, is not considered in our analysis due to the similar φ value for Ag and ITO and thus a negligible V_{bi} in our device. The validity of this assumption is also manifested
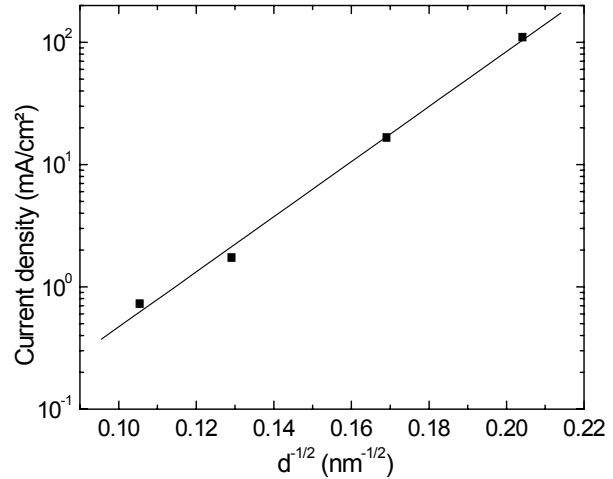
Fig. 4.10 Current data of the ITO/PbT/Ag devices (with different PbT thickness) at a bias of 1.5 V plotted in the form *ln(j)* as a function of $d^{-1/2}$.

from the I-V behavior at the reverse bias (ITO is negatively biased) which is nearly the same as that at the positive bias shown in Fig. 4.9.

At higher fields (larger than 2.5-3 V), the contribution of the bulk conduction through the polymer becomes dominant. A power dependence of the I-V feature is given in Fig. 4.9(b): I $\propto V^m$, m ~ 3, which suggests that the current through the PbT is space- charge limited with a shallow trap distribution. The high current at a relatively low voltage (lower than 6 V) indicates a good hole-transport capability of the bulk PbT, which is consistent with the relatively high hole mobility (10^{-5}-10^{-3} cm²/(V·s))[161-162, 120] for the PT materials.

4.2.1.2 ITO/PbT/NPB/Ag structure

In this configuration, the organic layer is the hole-transport layer NPB with and without PbT (see Fig. 4. 11). None of these types of devices shows electroluminescence (EL) due to the negligibly small number of electrons injected. The transport current in the ITO/NPB/Ag structure is very low even at a high bias (15 V), which is attributed to the poor hole-injection at the ITO/NPB contact. On the other hand, the current of the PbT- sandwiched device exceeds that in NPB-only one at the voltage above 4 V and is even more than one order of magnitude larger at higher voltages. Since the NPB layer is identical in both cases, the higher current should be correlated with a decreased barrier as a result of the introduction of the PbT

layer. This behavior demonstrates that PbT is effective in enhancing hole injection by the contact with ITO and NPB.
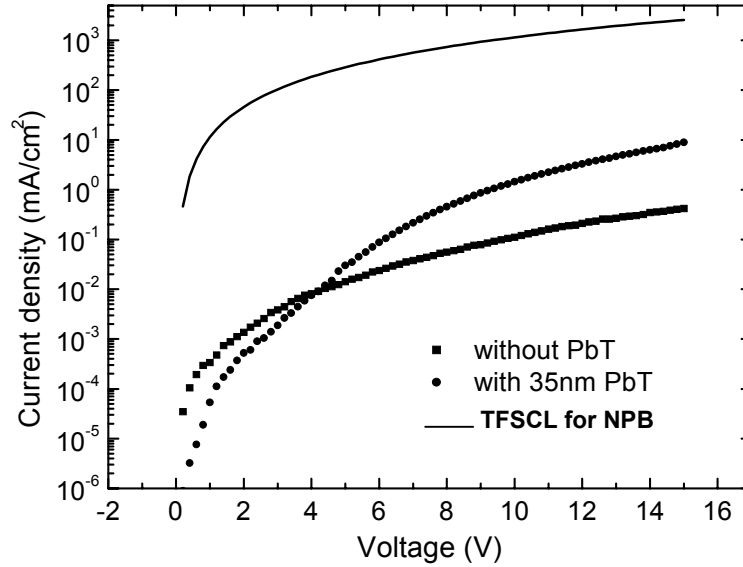
Fig. 4.11 I-V characteristics of hole- only devices with and without a PbT layer. The thickness of the NPB and PbT layer is 200 nm and 35 nm, respectively. The solid line shows the trap free space- charge limited (TFSCL) current densities for a 200 nm of NPB calculated from Eq. (4.5).

For comparison, Fig. 4.11 also shows the theoretically predicted trap free space-charge limited (TFSCL) current[16] (the maximum unipolar current that can flow through a device) for a NPB layer of 200 nm, based on the relation:

$$J_{SCL} = \frac{9}{8} \varepsilon\varepsilon_o \mu \frac{V^2}{d^3}$$
(4.5)

where the hole mobility for the trap- free NPB as assumed is field-independent with a value of 4×10^{-4} cm^2/V·s given in the literatures[9, 163]. The measured current density in the device with PbT is about two to three orders of magnitude lower than the calculated TFSCL current. The result indicates that the transport behavior of such a device is still injection- limited even by the introduction of an injection layer, which is attributed to a considerably large injection barrier at the ITO/PbT contact due to a very low work function of the ITO. The enhancement of hole-injection will be expected if the ITO with a higher work function is used.

Another approach may lie in the increase of the oxidation degree of PbT and thus a higher concentration of free charge carriers, by which a thin space charge layer at the contact can be formed and the condition for the formation of a Schottky barrier can be reached to achieve an efficient tunnelling injection of holes from ITO into the PbT[159].

Due to the complexity of the ITO/PbT/NPB contact, a quantitative analysis of I-V data by a theoretical model is difficult. For further investigations on the organic/anode interface and the role of the PbT interlayer, the contact is characterized by impedance spectroscopy (IS)[164]. A

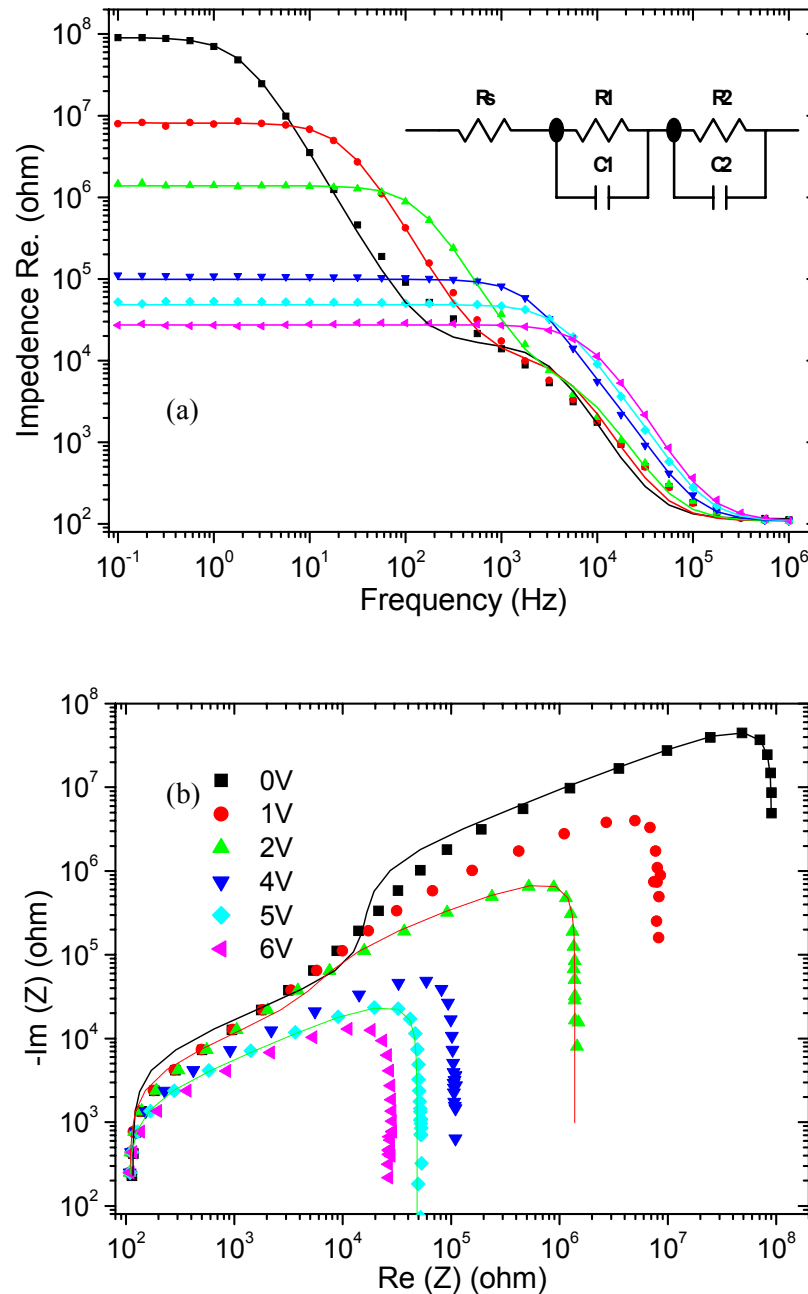Fig. 4.12 (a) Real part Re(Z) and (b) Cole-Cole plot of the complex impedance $Z(\omega)$ of an ITO/PbT/NPB/Ag device ($d_{PbT} = 35$ nm, $d_{NPB} = 200$ nm, device area $A = 7$ mm^2) at room temperature for different bias voltages in the atmosphere of N_2. The dots represent the experimental results while the solid curves are the fittings using the equivalent RC circuit shown in the inset.

frequency response analyser (Solartron Instrument SI 1260) combined with a 1296 dielectric converter is used by applying an ac voltage with a rms amplitude of 0.1 V in the frequency range between 1 Hz and 1 MHz. The dc bias on the device varies from 0 to 7 V.

Fig. 4.12 shows the real part Re (Z) and Cole-Cole plot of the complex impedance $Z(\omega) = Re(Z) + jIm(Z)$ of above ITO/PbT/NPB/Ag device at different bias. As expected, the real part of the impedance at low frequencies decreases strongly with the increase of the bias voltage. The maximum Re(Z) value in the Cole-Cole plot corresponds to the sum of the device resistance and the resistance of the ITO substrate. Whereas at higher frequencies, Re(Z) and Im(Z) are more frequency-independent. The minimum Re(Z) at infinitely high frequency is the ITO layer resistance (*ca.* 110 Ω). It is to be noted that, at the bias voltage lower than 3 V, a distinct structure located at around 3 to 4 kHz is detectable in each Re(Z(w)) curve, corresponding to the second semicircle in the complex impedance plane. The behavior can be modelled by two RC circuits in series (shown in inset of Fig.4.12). The fitting of the Z(ω) curves with the equivalent circuit is displayed in Fig 4.12 (a) and the fitting data are given in Table 4.3 for different dc biases. It is found that the capacitance C_1 and C_2 corresponds well to the geometrical capacitance of the PbT layer (3-4 nF) and that of the NPB layer (*ca.* 0.80 nF), respectively, with $C_{1(2)} = \dfrac{\varepsilon_{1(2)}\varepsilon_o A}{d_{1(2)}}$. Whereas the bias-dependent resistance R_1 and R_2 is attributed to the resistance of the PbT and that of the NPB layer, respectively. At high fields, the bulk resistance of PbT becomes very small so that its contribution to the voltage drop is not significant with respect to the NPB. For a very thin PbT layer (e.g. 20 nm), the PbT will act as a real interlayer with a negligible voltage drop upon the layer.

Table 4.3 Parameters obtained by fitting the experimental data with the equivalent circuit depicted in Fig. 4.12

V_{bias} (V)	R_1 (Ω)	C_1 (nF)	R_2 (Ω)	C_2 (nF)	R_s (Ω)
0	9.02 x 10^7	0.884	2.19 x10^4	3.027	116
1	8.12 x 10^6	0.855	1.04 x 10^4	3.059	110
2	1.36 x10^6	0.822	5378	3.442	110
4	9.66 x10^4	0.775	2254	4.367	109
5	4.68 x10^4	0.768	1534	4.486	108
6	2.51x 10^4	0.779	1080	4.595	110

From the I-V and IS measurements, Fig. 4.13 gives a schematic energy level alignment at the contact of ITO/NPB and ITO/PbT/NPB. The insertion of a PbT thin layer partitions an

abrupt injection barrier at the ITO/NPB contact into two smaller energetic steps to allow an easier injection of holes into the hole transport layer. A further optimization is the introduction of additional interlayers. Normally several layers are necessary to cause the barrier to vanish.
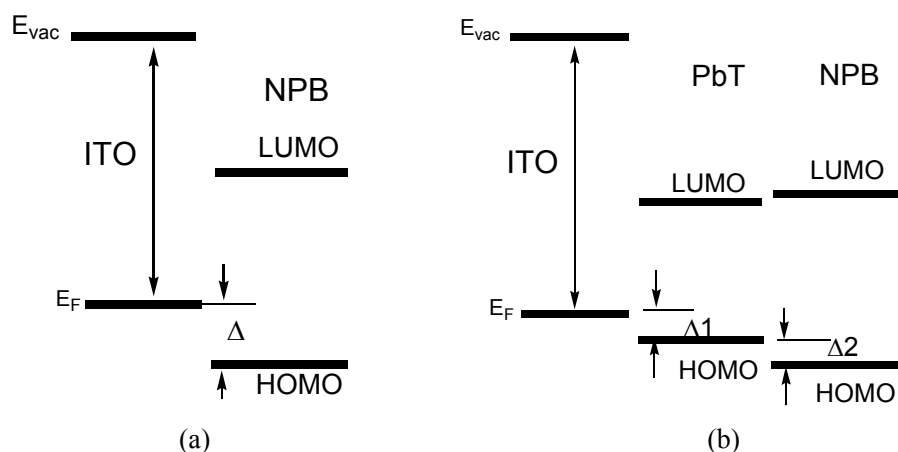
Fig. 4.13 Energy level alignment at the interface of (a) the ITO/NPB and (b) the ITO/PbT/NPB, respectively. Δ is the energy barrier for hole injection.

This is expected to be particularly useful for the hole-transport layer with a very large HOMO level for which the hole injection is difficult. It should be mentioned that this level scheme neglects such an effect as the interfacial dipole that to some extent has a significant influence on the energy offset at the interface[139, 165]. The more detailed and precise information about the energy level alignment can be obtained by photoelectron spectroscopy (XPS and UPS)[142].

4.2.2 Mutilayer OLED: NPB/Alq$_3$ bilayer

Mutilayer OLED devices consist of a NPB layer with varied thickness (70-100 nm) and a 70 nm tris(8- hydroxyquinolinato) aluminium (Alq$_3$) layer on a PbT-coated ITO anode. The device structure is shown in the inset of Fig. 4.14 (a). The same structure without PbT was also fabricated as a control device. As the cathode layer an alloy of Mg and Ag (10:1) of 150 nm thick was used. Electrooptical properties were characterized as described in Section 3.2.

The current-voltage (I-V) and luminance-voltage (L-V) characteristics of these OLEDs are plotted in Fig. 4.14. The device without the polymeric hole-injection layer shows a poorly behaved I-V feature. On the other hand, well-behaved I-V characteristics are observed for the devices with the PbT layer. In these cases the leakage current is suppressed by four to five orders of magnitude at low electric fields, while the onset of light emission (turn-on voltage, at which luminance is 1cd/m²) decreases as expected. The current and luminance are significantly enhanced even for larger thickness of the hole transport layer at a given

Fig. 4.14 Performance of multilayer OLEDs measured in situ. Top: I-V characteristics; bottom: L-V characteristics. The OLEDs are characterized by a 20-25 nm Pb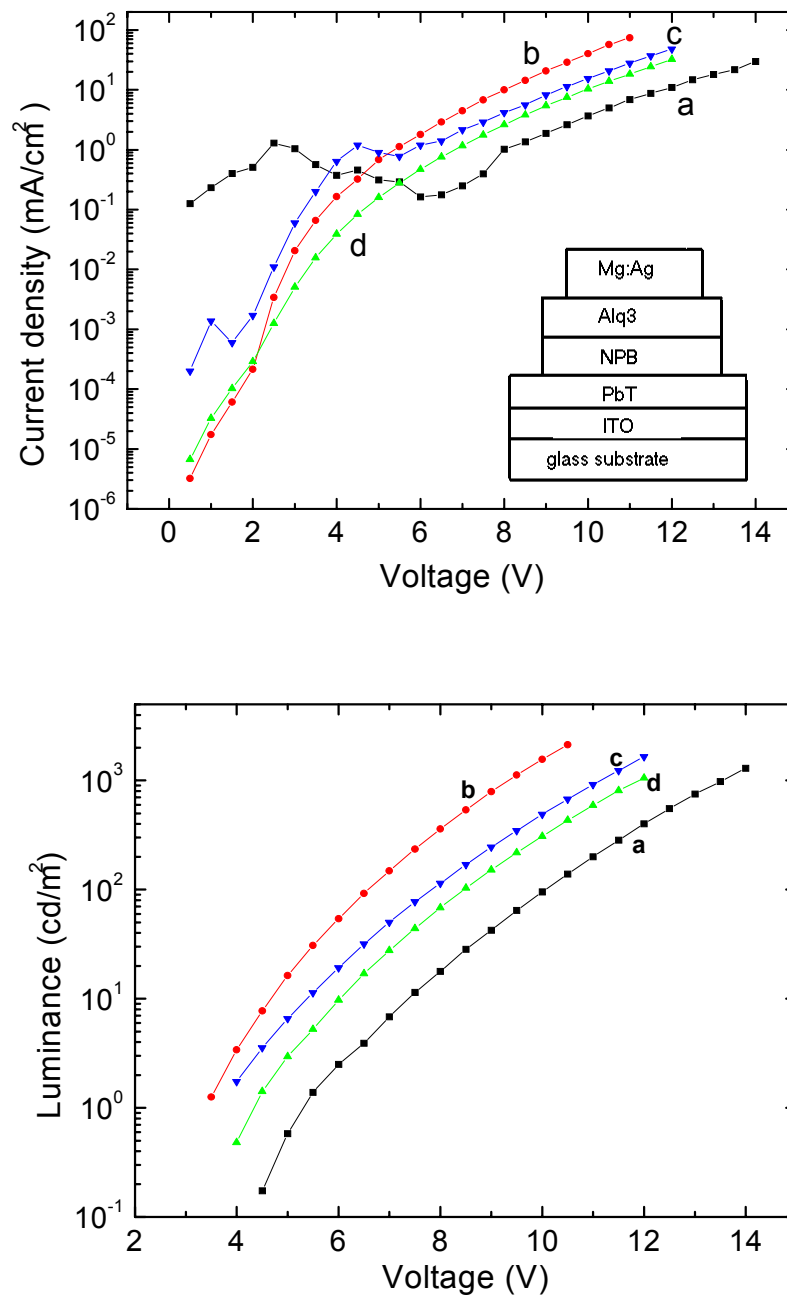T injection interlayer and 70 nm Alq_3 layer, as well as the NPB layer with a thickness of 70 nm (b), 87 nm (c), 100 nm (d), respectively. Device A has no PbT layer and a NPB thickness of 70 nm. Inset: OLED structure.

voltage. Both current and luminance are more than one order of magnitude larger compared to the device without PbT for a given layer thickness of NPB and Alq_3: the operating voltage is reduced by 4 V at the same luminance. Table 4.4 provides the main performance data of both types of devices. The improvement of the performance by the introduction of PbT is manifest. The luminous efficiency reaches 1.7 lm/W for devices with the injection layer compared with 1.1 lm/W for the control device. The improved performance should be caused by a remarkable enhancement of the hole injection between ITO and NPB by the insertion of the PbT layer.

Table 4.4 Performance of a 70-nm NPB/70-nm Alq_3 structure with and without PbT layer

	OLED with PbT	OLED without PbT
Luminance (cd/m^2) at 10 V	1560	100
Current density (mA/cm^2) at 10 V	42	3
Operating voltage (V) for $100cd/m^2$	6.5	10
Max. Luminous efficiency (lm/W)	1.7	1.1
Quantum efficiency (cd/A)	3.8	4.5

a. Device efficiency

Fig. 4.15 shows the (external) current efficiency η_c (cd/A) as a function of the applied voltage for different OLEDs. The devices with PbT show a weak dependence of the efficiency on the thickness of the hole transport layer, i.e. a small enhancement with the reduction of the NPB thickness. In all cases the efficiency seems to have a maximum value. On the other hand, the efficiency for the control device increases gradually with the applied voltage within a long
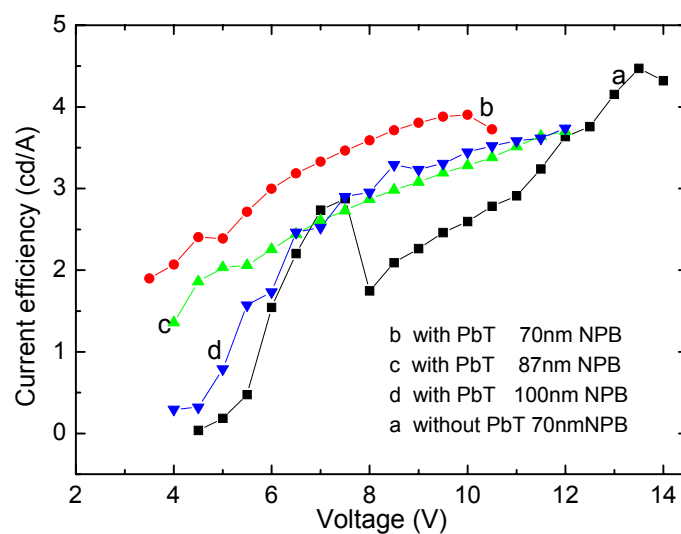

Fig. 4.15 External current efficiency η_c (cd/A) as a function of the bias voltage for different OLEDs shown in Fig. 4.14. The absorption of the PbT layer was not accounted for.

range of the bias sweep (0-13.5 V) (the oscillation at the interval of 4 to 8 V may be due to current instability), its maximum efficiency is around 4.5 cd/A compared to 3.9 cd/A on the counterpart with PbT (device b). Taking into account the absorption loss of the PbT layer for the emission of Alq_3 (the transmission of such a PbT layer is *ca.* 80%), the corrected efficiency is nearly the same for both devices. It indicates the efficiency η_c does not depend on the hole-injection behavior.

Similar results were also obtained by other authors, who measured an identical efficiency (cd/A) on TPD/Alq_3 OLEDs that had different ITO's or a Pt- modified ITO anode[166, 79]. The reason for this behavior lies in the fact that the quantum efficiency (corresponding to η_c) in such bilayer OLEDs is determined by the ratio of the density of holes and electrons accumulated at HTL and Alq_3 sides of the HTL/Alq_3 interface[6, 167], respectively. The enhancement of hole-injection from the anode increases the hole accumulation at the NPB side, which results in a higher electric field across the Alq_3 layer and thus an enhanced electron injection and transport in Alq_3. As a result, the accumulation of electrons also increases at the Alq_3 side, which restores the ratio of charge densities at the interface. Therefore the introduction of PbT as the injection layer does not affect the quantum efficiency in spite of a lowering of the operating voltage. However, upon the enhancement of hole injection, the applied bias at which an optimized accumulation of charge carriers is achieved at the NPB/Alq_3 interface will shift towards a lower voltage as shown in Fig. 4.15. Additionally, it is expected that holes are the dominant charge carriers and the electron injection from the cathode should be the main limiting factor for the EL process in this case

due to a large electron injection barrier at the $Alq_3/Mg:Ag$ interface as well as a relatively low electron mobility in Alq_3. With further optimization by the introduction of LiF/Al as cathode at which the electron injection is enhanced remarkably[88], or by the use of the more effective electron transport layer (e.g. Bphen)[86], a larger ratio of electrons/holes at the NPB/Alq_3 interface and thus a more balanced injection and transport of holes and
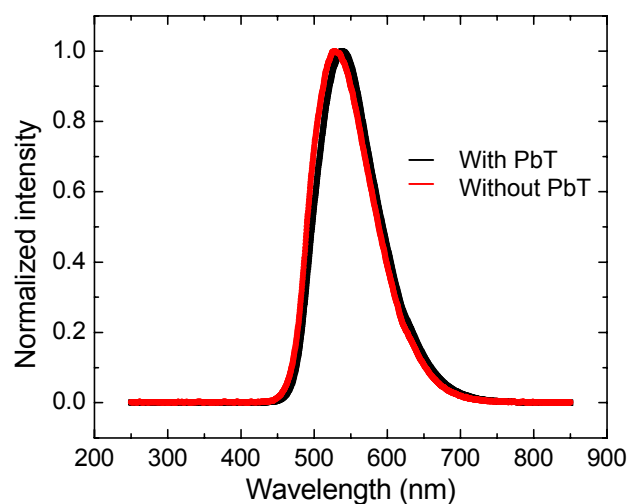
Fig. 4.16 Electroluminescent spectra of the $ITO/NPB/Alq_3/Mg:Ag$ devices with and without PbT interlayer.

electrons can be achieved. A higher quantum efficiency is expected.

b. Influence of the PbT thickness

Fig. 4.16 shows the EL spectra of the control device and the device with a 24 nm PbT interlayer. They are almost identical, with an emission peak at 530 nm, although the color of
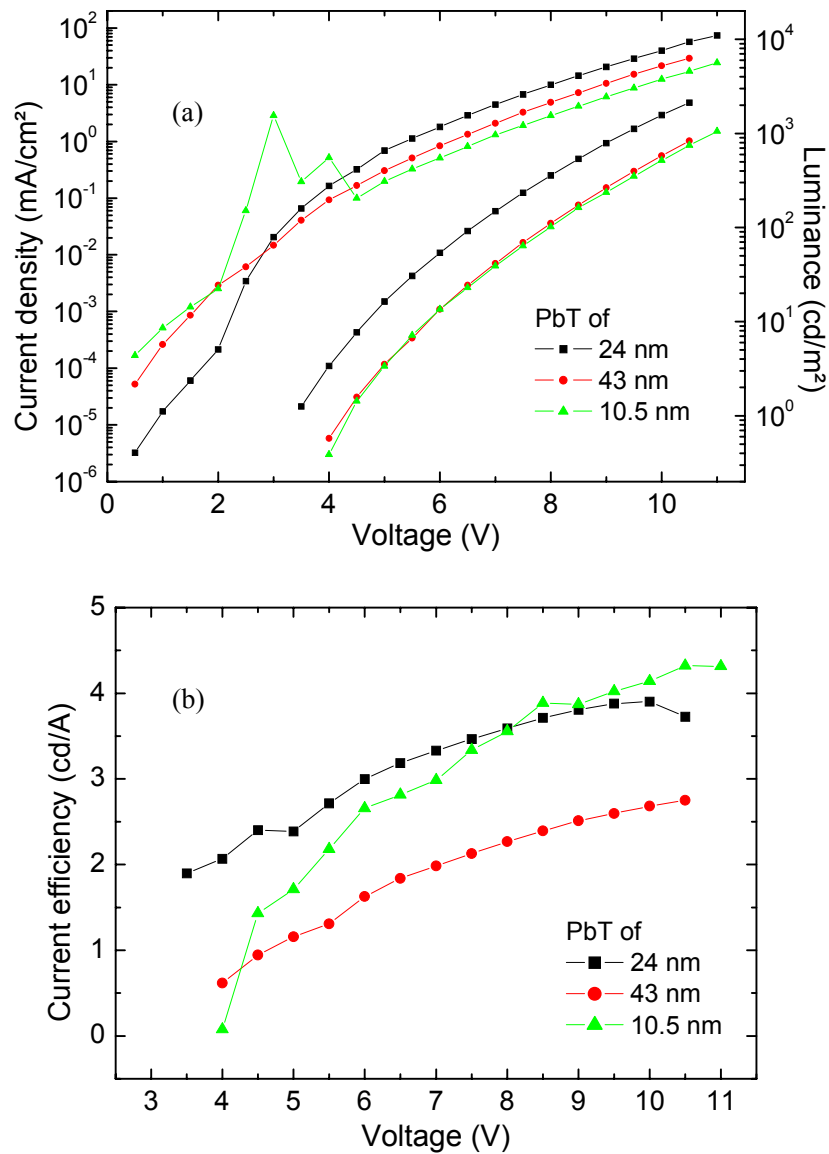
Fig. 4.17 (a) I-L-V and (b) EL efficiency characteristics of OLEDs as a function of the thickness of the PbT interlayer.

the PbT ultrathin layer is slightly orange which is attributed to its absorbance. The investigation has also been made on the influence of the thickness of the PbT layer on the I-L-V feature of OLEDs as shown in Fig. 4.17. There is no distinct dependence on the PbT thickness in the range of 20-30 nm. However at lower thickness (device A, with a 10.5 nm of

PbT), the leakage current is found to increase at low fields while the operating voltage rises somewhat. This should be attributed to an incomplete coverage of the ITO anode by the PbT layer and thus the existence of a bare part of ITO because the roughness of the PbT layer is up to 6-7 nm. On the other hand, a further increase of the PbT thickness (device C, with 43 nm of PbT) will lead to an increase of the operating voltage as well as a lowering of the current efficiency. It is suggested that in this case, the voltage drop on the PbT layer will increase considerably due to a larger thickness and a low conductivity of the PbT (in the neutral state). Therefore the effective bias applied on the NPB/Alq$_3$ bilayer is reduced. More notably, the absorption loss of the EL emission through the PbT layer becomes much larger (the transmission of a 43 nm PbT is lower than 60 %), which reduces the light output. Thus a reduction of the device efficiency is caused. Based on our investigation, the optimum thickness range of the PbT is 20-25 nm. The layer with such thickness is utilized for OLED preparation in most cases.

c. Current- voltage feature

Fig. 4.18 shows the current-voltage curves of different NPB/Alq$_3$ OLEDs in a log-log plot. The principal I-V behavior of all devices is very similar even though a large difference of the
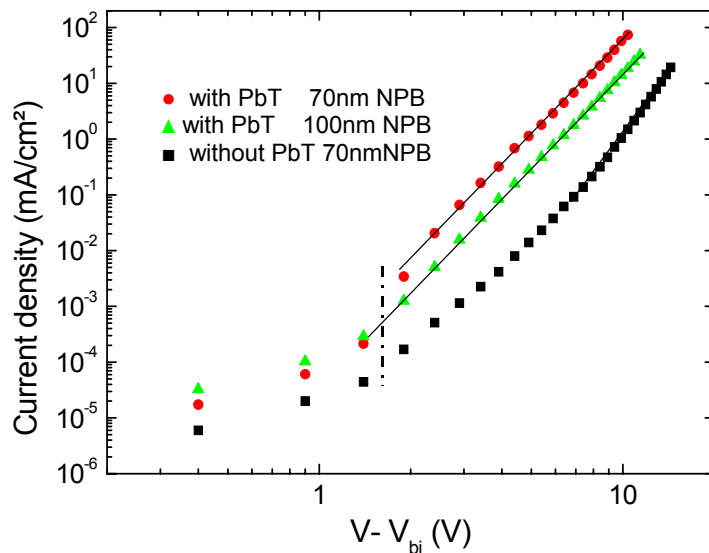
Fig. 4.18 Current-voltage features of OLEDs with and without PbT layer in double logarithmic plot. The built-in potential V_{bi} is approximated by the work function difference of ITO anode and Mg:Ag cathode (*ca.* 0.6 V).

current density by more than one order of magnitude between the devices with and without PbT. At the low field, the transport current should be a combination of an injection current and a small leakage current. At higher fields, the I-V characteristics for all devices can be

described by $I \propto V^m$, $m \sim 6$, indicating that the current is controlled by the trap-limited transport of electrons in Alq_3[148]. The transition from the behavior at low fields into that at high fields takes place at the effective voltage of 1.5-2 V (considering the built-in-potential V_{bi} of the device), identical for different devices in which different hole injection and transport features are manifest. We suggest that the transition point corresponds to the onset of the bipolar injection and recombination, i.e. turn-on voltage of EL light output, despite that we have not detected the EL emission at such low voltage due to the low sensitivity of our spectrometer system.

It is surprising to note that the device current is determined by the bulk conduction behavior of Alq_3 at high field considering that a considerably large injection barrier for hole (electron) remains at the organic/anode (cathode) interface. The bipolar current effect should thus be significant which is assumed to redistribute the electric field in the device and to influence the carrier injection behavior. However, a detailed analysis of charge carrier injection and transport in bilayer OLED is more complicated, which demands thickness- and temperature-dependent I-V investigations, as well as more importantly the inclusion of the bipolar injection and recombination effect in the theoretical description[158,18]. Numerical simulation should also be used if the charge trap effect and field-dependent mobility are considered.

d. Device reliability

Besides the capability of enhancing the hole-injection at the organic/anode contact, a noticeable merit by utilizing the PbT layer is a remarkable elimination of the leakage current of the device that originates from dusts and imperfections on bare ITO. A thin layer of PbT can cover the imperfection in a conforming way, which prevents a direct contact between anode and cathode at the microconducting pathways to eliminate the local 'hotspots' and thus the occurrence of the non-emissive blackspots in the cathode. In addition, the crystallization of the PbT layer is negligible due to its high glass transition temperature, which will favor the morphological stability of the organic layer. Based on these facts, we expect that the introduction of PbT will benefit the device reliability. Although we have not carried out a systematic investigation about the influence of the PbT layer on the lifetime of OLEDs, we have indeed observed a much slower degradation of the current and luminance for the OLEDs with PbT compared to the devices with a bare ITO. The tests were performed with a starting luminance of 100 cd/m² in vacuum and at the constant bias (6.5 V for PbT- with device vs. 10 V for PbT- without one). Meanwhile the current noise during device operation is eliminated significantly for the device with PbT, indicating the enhanced device stability.

4.2.3 Doping effect of PbT

The polybithiophene layer used in the device fabrication on the preceding sections was undoped. The doped (oxidized) PbT should be more favourable due to its high work function and higher conductivity, as well as a higher transmission factor[114]. PF_6^-- doped PbT (with a doping level of 4.0%) was utilized as the hole-injection contact for OLED. Fig. 4.19 gives the I-V features of a hole- only device (a) and a bilayer OLED (b) with a 25-30 nm doped PbT layer. The transport current on the hole- only device shows an ohmic behavior, indicating the
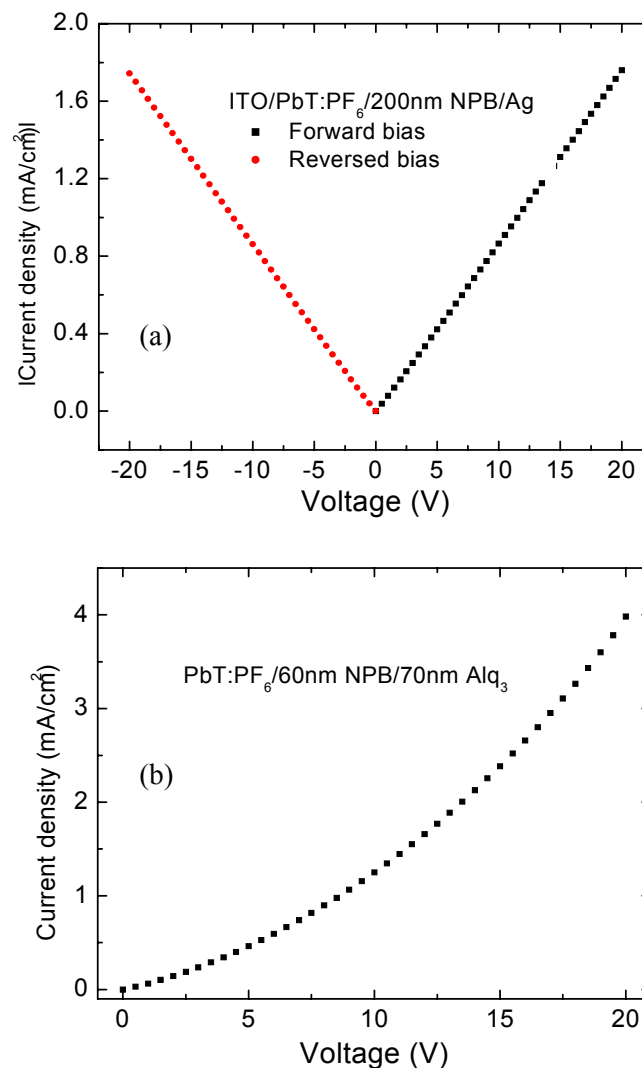
Fig. 4.19 Electrical characteristics of the devices introducing a PF_6^-- doped PbT layer. (a) an ITO/PbT (25 nm)/NPB (200 nm)/Ag; (b) an ITO/PbT(25 nm)/NPB(70 nm)/Alq_3(70 nm)/Mg:Ag device.

existence of a resistance of about 104-105 kΩ at both positive and negative biases. Moreover, no light emission occurs on the bilayer OLED. The exact reason is not clear yet. It is suggested that there exists two possible sources for such behavior. One is the formation of a

thin insulating interfacial layer at the PbT/NPB interface[123] which hinders the current transport and results in the symmetric I-V feature. Another lies in a possible diffusion and migration of small dopant anions from the PbT layer into the organic layer, which leads to the EL quenching at the NPB/Alq$_3$ interface. A clue to solve the puzzle may lie in the investigation of the dependence of the I-V feature on the doping degree (corresponding to different concentration of free charge carriers) of the PbT layer in combination with impedance measurement and the XPS.

4.3 Conclusions

Polybithiophene thin layers with a well-defined morphology and a high degree of smoothness have been prepared by the electropolymerization of 2,2'- bithiophene. The films in the semiconducting and neutral state are chemically and electrochemicallly stable, whereas the oxidized state is relatively unstable and only a low doping level remains with a relatively homogenous spatial distribution of the counter-anions. The energetic states (e.g. the HOMO) of PbT have been determined by the electrochemical method.

Semiconducting PbT thin layer has been utilized as a hole-injection contact. The following results have been obtained:

(1) The PbT improves remarkably the hole-injection between ITO and the molecular hole-transport layer NPB. However, a considerably large barrier remains still at the ITO/PbT contact, which leads to a thermionic injection of holes at low field.

(2) Vapor- deposited NPB/Alq$_3$ OLEDs incorporated with a PbT layer show a sharp reduction of the operating voltage as well as an enhanced luminous efficiency and luminance compared to the device without PbT. The introduction of PbT does not affect the value of the current efficiency but shifts its maximum to a lower field. Additionally, the optimum range of the PbT thickness is found regarding the OLED performance. However, the fabrication of OLEDs incorporated with doped PbT layer has not been successful.

Based on these facts, it has been demonstrated that the incorporation of an electropolymerization step into the fabrication of vapor-deposited molecular OLEDs is an alternative approach to produce high performance OLEDs. This result is very encouraging for the utilization of this method to other anode structures based on the polymer (semiconducting and conducting)/small molecule interface.

5. Electrochemical treatment of PEDT:PSS for OLED

5.1 Introduction

As seen in the preceding section, there is a considerably large barrier for hole injection between ITO and an undoped PbT interlayer as well as a voltage drop through such a layer in spite of an enhanced hole injection. The oxidized state of PbT is unstable and the fabrication of an OLED using doped PbT has not been succeeded. Therefore, other polythiophene materials with a stable doping level have to be introduced. Poly(3,4-ethylendioxythiophene) (PEDT) seems to be a good candidate due to its remarkable properties[131-132,168]. PEDT is very stable in the doped state and can reach a high conductivity up to 200 $S \cdot cm^{-1}$. It is one of the most environmentally stable conducting polymers known so far. Additionally, it is almost transparent in thin oxidized films[131]. Usually, the electropolymerization is a convenient method for the preparation of PEDT layer, which has been extensively studied in last years. However, as demonstrated in our experiments[169], PEDT layers from this process are not homogenous enough with a large amount of irregular structures in the surface, which cause readily the short circuit of OLED devices using such PEDT as the injection layer.

On the other hand, a water-soluble blend of PEDT with poly(styrensulfonate) (PSS) (PEDT:PSS, invented by Bayer AG) from oxidatively chemical polymerization has good film-forming properties[170, 171], and has been commonly used as the buffer layer in polymeric OLEDs. It has been found that the PEDT:PSS-covered ITO anode reduces the operating voltage and increases the device lifetime remarkably[68-71]. This was attributed to a lowered hole-injection barrier between ITO and the HTL as well as a smoother surface of the anode than the bare ITO. Usually, this layer is prepared by spin-coating of the PEDT:PSS dispersion. To optimize its electronic and optical properties, a controlled treatment of the dispersion or the produced layer is necessary. However, up to now, there are only a few reports on this strategy. For instance, PEDT:PSS was added with a small amount of glycerol (G-PEDT:PSS) [172], which allows the conductivity of PEDT:PSS to be dramatically enhanced. Based on this, a whole- PEDT:PSS anode without ITO has been employed in OLEDs[173]. Here, we attempt to adjust the doping level of the PEDT:PSS layer electrochemically in order to tune the hole-injection capacity between the ITO/organic interface.

The doping level of the polymer anode is correlated with its electrochemical equilibrium potential (E_{eq})[174], and an offset exists between E_{eq} and the work function ϕ, with the latter directly influencing the hole injection barrier[124]. It is therefore possible to control ϕ of the

anode directly by adjusting the doping level of the polymer. The electrochemically-induced charge transfer is a convenient method to adjust the redox state of the polymer in an electrodeposition process[174], and the potentiostatic doping of the polymer is usually used. Gross *et al.* demonstrated that the barrier of hole injection can be tuned continuously by modifying the doping level of an poly(4,4'-dimethoxybithiophene) (PDBT) layer prepared eletrochemically[114]. For the π-conjugated PEDT, this method is particular suitable because the polymer keeps redox- active without degradation over a broad potential range from –1.0 V to 1.4 V[131, 168]. Thus a wide range of the tunability for E_{eq} exists. Within this range, a continuous distribution of the redox states is observed. Therefore the work function should be adjustable in small steps by the electrochemical method. However, the layer formed by electropolymerization is not smooth enough, which will be disadvantageous to the performance and reliability of the device fabricated[114]. In our case, a smooth PEDT:PSS layer from a casting procedure was chosen and p-toluensulfonic acid was used as supporting electrolyte to modify the doping state of the polymer. By utilizing the treated polymer layer as the hole-injection contact, an effort is made to optimize the hole-injection feature and performance of the vapor- deposited molecular OLEDs.

5.2 Electrochemical treatment: process and characterization

Patterned ITO-coated glasses (Merck. 15Ω/□) were cleaned extensively, and then treated in oxygen plasma prior to use. The polymer films were prepared by spin-coating of an aqueous PEDT:PSS dispersion (Baytron ® P[175], its chemical structure is shown in Fig. 5.1) on ITO. Very homogenous layers were formed due to the good wetting of such ITO surfaces. The thickness is about 60-150 nm as determined by AFM measurement. Then the films were dried at 100°C for 10 min in air. The PEDT:PSS films prepared according to this procedure are referred as 'as-prepared' in contrast to 'treated' films in the following sections.

The tuning of doping level was carried out by the potentiostatic electrolysis at the applied potentials from -0.6 V to 0.8 V in a one-compartment cell. The supporting electrolyte was water- free 0.1 M p-toluenesulfonic acid (its structure is shown in Fig. 5.2) in acetonitrile. Tosylate (Tos⁻) was chosen due to its structural similarity with the repeating unit of PSS as well as its higher mobility compared to PSS. The PEDT:PSS-coated ITO anodes served as working electrodes; the reference and counter electrode was Ag/AgCl and Pt, respectively. All potentials given are referred to the potential of an aqueous Ag/AgCl electrode. The electrolyte was degassed from oxygen by nitrogen bubbling for 15 min and a nitrogen atmosphere was

Poly(3,4-ethylenedioxythiophene) (PEDT)

PSSH

(PSS⁻Na⁺)
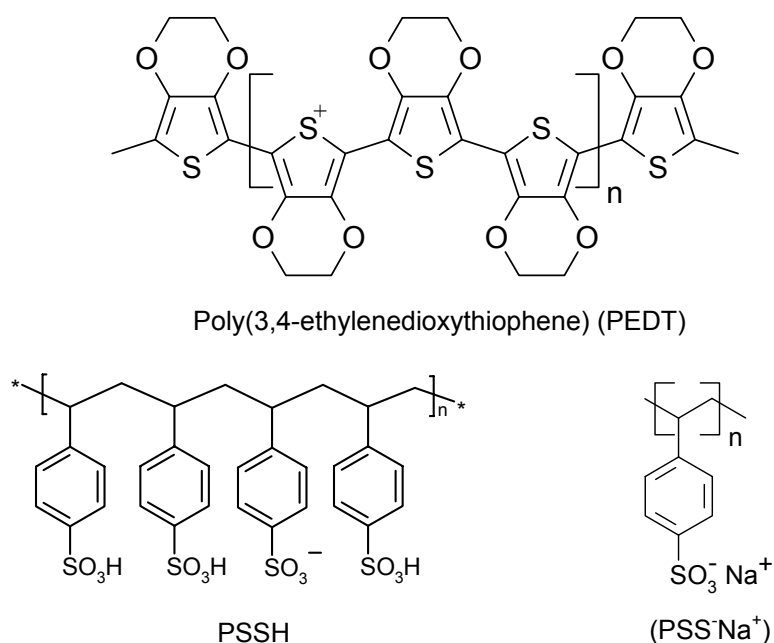
Fig. 5.1 Chemical structure of PEDT:PSS

maintained over the solution during the experiment. Thereafter, the films were rinsed carefully with acetonitrile and dried in a stream of pure N_2. The electrochemical equilibrium potential E_{eq} was determined from the value of open circuit potential (OCP) measured after the procedure mentioned. The absorption spectra were obtained at relevant E_{eq} values in air with a Shimadzu UV 3101 PC UV-vis-NIR spectrophotometer. XPS measurements were performed with a PHI 5600I spectrometer equipped with monochromatized Al K_α source, and ultraviolet photoelectron spectroscopy (UPS) measurements were carried out with He I (hν = 21.2 eV) radiation.

5.2.1 Variation of doping level

Fig. 5.2 is the cyclic voltammogram (CV) of an 'as-prepared' PEDT:PSS film (60 nm) in 0.1M toluenesulfonic acid/acetonitrile solution. The voltammogram shows an oxidation peak of PEDT at *ca.* 0.35 V, which is very similar to that for the PEDT electrodeposited in aqueous electrolyte. The film displays a reproducible redox behavior in the electrolyte and remains electro-active after continuous cycles between –0.2V to 0.7 V, indicating a high electrochemical stability.

When an electrode potential was applied upon the working electrode, the anodic or cathodic current flow occurs in dependence of the value of the potential. The amount of the charge within the polymer was thus changed, which as we assume should be accompanied by the
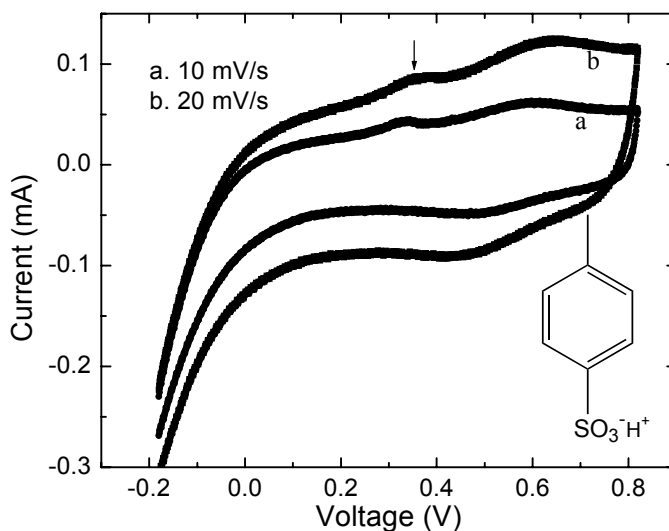
Fig.5.2 Cyclic voltammogram of an as-prepared PEDT:PSS film in 0.1M toluenesulfonic acid/acetonitrile solution at different scan rates. The thickness of the layer is *ca.* 60 nm. The inset shows the chemical structure of toluenesulfonic acid.

Table 5.1 The amount of the injected charge Q and the variation of doping level $\Delta\delta$ for a 120 nm PEDT:PSS layer (area: 5 cm², density: 1.5 g/cm^{-3}) by applying different potentials (vs. aqueous Ag/AgCl electrode).The sequence of potential steps applied follows the way: $0V\rightarrow 0.47V\rightarrow \ldots \rightarrow 0.77V\rightarrow 0.26V\rightarrow \ldots \rightarrow -0.48V$. The effect of double-layer capacitance on injection current was neglected.

Applied potential (V)	Q (mC)	$\Delta\delta$ (10^{-2})
none (as-prepared)	0.0	0.0
0.77	1.98	7.91
0.67	1.14	4.55
0.57	0.712	2.84
0.47	0.382	1.53
0.26	-0.30	-1.20
0.17	-0.632	-2.52
-0.18	-4.93*	-19.7**
-0.48	-15.30*	-61.1**

 * A part of cathodic current comes from a reduction process of the ITO substrate at negative potential ($\leq$ -0.18 V).
 ** Not reliable value of the doping level.

injection of Tos$^-$ anion or the migration of H$^+$ cation out of the polymer during the doping, as well as the injection of H$^+$ into the layer during the dedoping, respectively. The nominal doping level can be defined as:

$$\delta = \frac{\text{molar number of charge injected}}{\text{molar number of PEDT repeating units}} \quad (5.1)$$

Since PEDT:PSS (untreated) is highly p-doped with an oxidation level of 33%[175], the amount of charge (positive and negative) injected during the redox process should correspond to the variation of doping level $\Delta\delta$ in the polymer. With the known amount of PEDT:PSS deposited on ITO, the number of PEDT repeating units can be calculated (overall molar ratio of PEDT to PSS repeating units is 0.82[175]). Hence the change of doping level can be quantitatively determined. Table 5.1 lists the amount of injection charge and relevant $\Delta\delta$ values for a 120 nm thick PEDT:PSS layer at different electrode potentials. The doping level increases monotonically with the applied positive potential.

Table 5.2 Electrochemical equilibrium potentials E_{eq} of a PEDT:PSS layer corresponding to the $\Delta\delta$ value shown in Table 5.1 after the adjustment at different applied potentials (vs. aqueous Ag/AgCl electrode).

Applied potential (V)	E_{eq}^{a}(V)	E_{eq}^{b} (V)
None (as-prepared)	0.37	0.37
0.77	0.68	0.59
0.67	0.57	0.51
0.57	0.52	0.45
0.47	0.41	–
0.26	0.27	0.27
0.17	0.23	0.22
-0.18	-0.01	0.09
-0.48	-0.05	0.02

a. Measured in the solution (20 min after the modification at positive potential and 5 min after the modification at negative potential, respectively).
b. Measured after the modified layers were rinsed by acetonitrile and dried

To validate the above introduced $\Delta\delta$, we correlate its value to a 'true' quantification of the doping level by measuring the electrochemical equilibrium potential E_{eq}. Table 5.2 gives a series of E_{eq} values of the layer after the corresponding redox processes. It indicates that the doping level of PEDT:PSS layer can be modified further in spite of its compact morphology, and suggests that the amount of the charge injected is indeed a good measure of the doping state of the polymer. As shown in Fig. 5.3, the E_{eq} value increases approximately logarithmically with the amount of the injected charge. The higher oxidation state (e.g. E_{eq} of 0.68 V) relative to the unmodified layer (E_{eq} of 0.37 V) is very stable, which is manifested

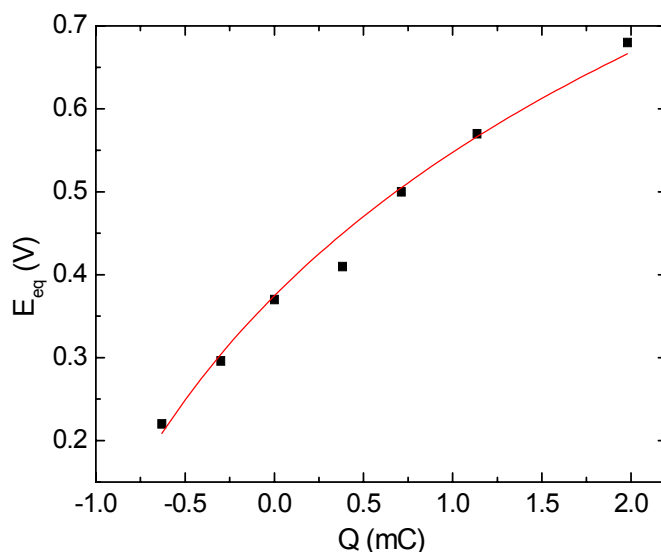Fig. 5.3 E_{eq}'s change (E_{eq}^a in Table 5.2) of a PEDT:PSS film (with a thickness of 120 nm and an area of 5 cm²) as a function of charge Q injected during electrochemical treatment. For the dedoping at high negative potential ($\leq$ -0.18 V), the data are not shown because of the high instability of the E_{eq} value and because the derived Q value is uncertain (a large part of cathodic current comes from the reduction process of the ITO substrate).

from only a slight drop of E_{eq} when the electrochemical process is interrupted by disconnecting the electrochemical cell. Such a high oxidation state also changes little at dry state in air (a slight drop to 0.59 eV of E_{eq}. This observation is different from that in other conducting polymers e.g. polyanilline and polypyrrole[176, 177]. In those cases, the counterion tends to be solvated and mobile in the polymer when in contact with the solvent, resulting in an unstable doping. This stabilization of increased doping of PEDT:PSS is critical for the device preparation.

In contrast, the reduced state is more difficult to obtain. The applied potential of up to −0.5 V only leads to an E_{eq} value of 0 V in air. Furthermore, the reduced layer shows a rapid increase of open circuit potential in the electrolyte after the interruption of the reduction process. It is attributed to the very low reduction potential of PEDT (-0.5 V)[168]; a trace amount of O_2 and water from the electrolyte or air can oxidize the layer. In addition, if the layer is reduced at a large negative potential ($\leq$ −0.48 V) at first and then oxidized at the potential above 0.37 V (E_{eq} of as-prepared layer), the doping level is always lower than that for the as-prepared film (also confirmed by the following UV-vis-NIR spectra). It suggests the possibility that a degradation process of the PEDT:PSS occurs during the dedoping process.

The change of surface morphology of PEDT:PSS during electrochemical treatment is an important issue to consider. Fig. 5.4 shows the SEM graphs for the layers as- prepared and

after the doping at a potential of 0.77 V. Both of surfaces are highly smooth and no apparent morphological change takes place. The surface roughness of the modified layer is in the range

(a)   (b)
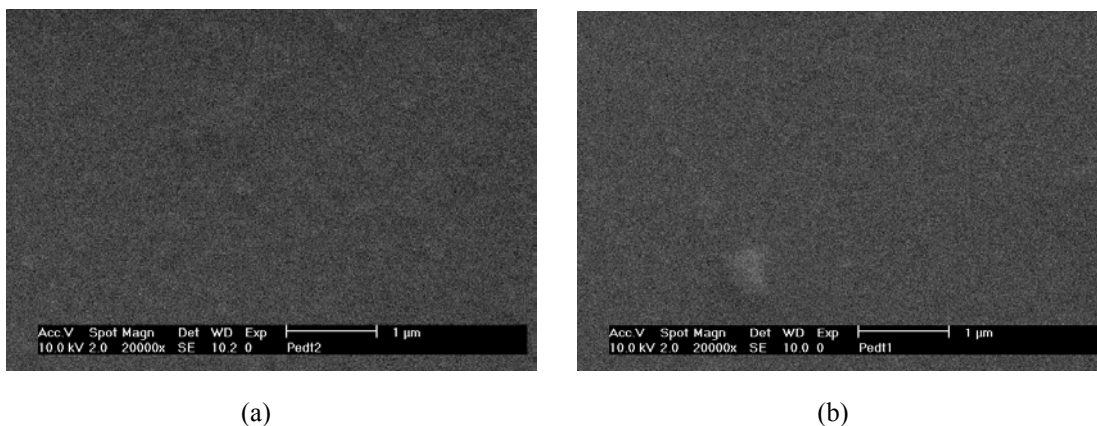
Fig. 5.4 SEM graph of PEDT:PSS layers for (a) as-prepared and (b) after electroche doping at the potential of 0.77 V.

of 2-3 nm determined by AFM, which is almost the same as that for the as-prepared layer. The morphological changes after the reduction are still small, only a little small cracks are found at the boundary of the film after long-time reduction for up to 400 seconds, which is attributed to the erosion of underlying ITO layer by the acidic electrolyte. In general, this indicates that the electrochemical treatment does not affect the homogeneity of the films.

5.2.2 UV-vis-NIR spectra

Fig. 5.5 shows a series of UV-vis-NIR absorption spectra for PEDT:PSS films adjusted at different electrode potentials. The absorption band below 1000 nm decays especially for the feature centred around 890 nm which is suggested to be the polaronic band[178]. While the band between 2000 nm and 1300 nm enhances gradually with the increase of positive potential, which is ascribed to a bipolaron subgap state[179]. The number of bipolaron states increases while the number of polaron states decreases with increasing doping level, which indicates that a transition from polaronic to bipolaronic state occurs during the doping process. The variation of the absorption corresponds to that of the E_{eq} value shown in Table 5.2.

It is to be pointed out that the absorption band at a higher oxidation state is very similar to that for the as-prepared layer (slight enhancement of bipolaron band relative to the latter), because the oxidation level is already high in the latter. On the other hand, the infrared bands are still present and the absorption associated to the π-π* transition (band at 580 nm) remains very weak when the high negative potential is applied. It indicates that the reduced PEDT is not entirely neutral, similar to the case for aqueous PEDT electrodeposited[180]. Two possible
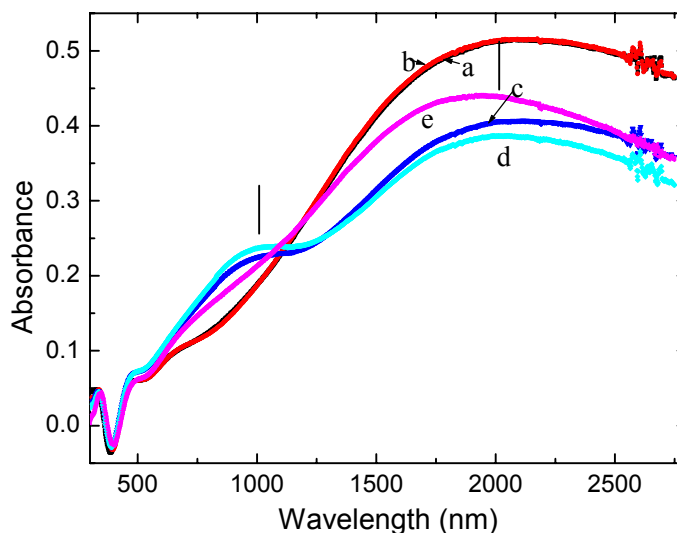
Fig. 5.5 UV-vis-NIR absorption spectra of a 120 nm PEDT:PSS on ITO as a function of the electrode potential: a. as-prepared, b. 0.77 V, c. –0.18 V, d. -0.48 V, e. 0.77 V after the layer was reduced at –0.48 V.

reasons are suggested which cause such a feature: (1) existence of some amount of charged PEDT after the reduction which originates from the compact structure of the PEDT:PSS layer; and (2) the low stability of the reduced state of PEDT in the ambient atmosphere. A neutral film will be oxidized rapidly during the interval of the measurement. Therefore, the *in-situ* spectro-electrochemical investigation of the reduction process should be carried out to distinguish between these two sources.

5.2.3 XPS and UPS results

XPS spectra were used to investigate chemical change of PEDT:PSS during the electrochemical modification process. Fig. 5.6 shows the XPS survey spectra of PEDT:PSS layers before and after the doping/dedoping, respectively. For an as-prepared layer, a clearly visible Na 1s peak is found, indicating a large amount of sodium (roughly one sodium atom per four sulfur atoms from quantitative analysis) in the near-surface region. However, Na 1s emission disappears completely after the treatment. Furthermore, the absence of sodium is also found if the as-prepared layer is immersed in pure acetonitrile for 10 min. This indicates that sodium can be completely exchanged by the solvent before the electrolysis (the electrolyte has to be degassed for 15 min). Therefore Na^+ ion is not responsible for the doping/dedoping process.

Fig. 5.7 (right part) shows the S 2p core-level spectra of PEDT:PSS as-prepared and after the doping. The complexity of the S 2p spectra implies that several sulfur-containing chemical
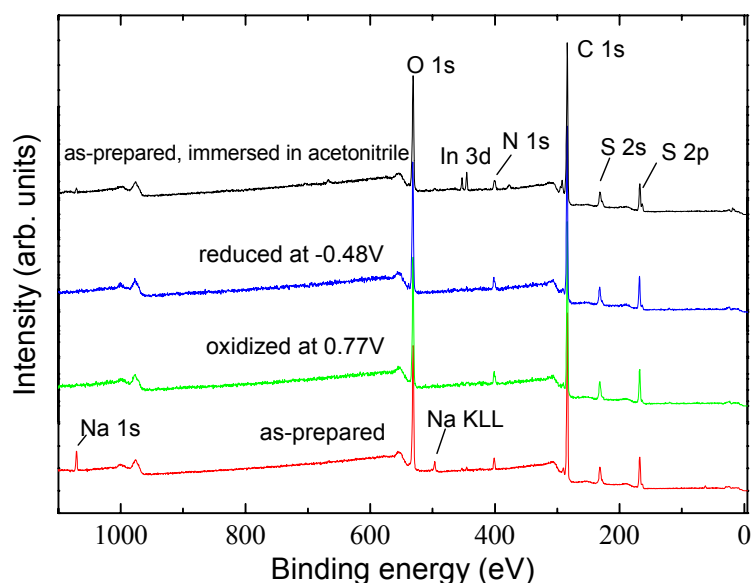
Fig. 5.6 XPS survey spectra of PEDT:PSS layers for as-prepared and after electrochemical treatment or stored in acetonitrile for 10 min.

species are present. For the as-prepared film, the lower binding energy (BE) doublet at 163.4 eV and 164.7 eV can be assigned to the sulfur atom in PEDT[181, 182]. Moreover it shows an asymmetric tail on the higher BE side. This arises from the presence of positive charges in the monomer units of the PEDT chain (p-doped), which is delocalized over several adjacent rings. The S 2p emission with the higher BE near 168 eV is assigned to the sulfur atoms in PSS, which according to the analysis by Greczynski[181] is a combined contribution from the PSSH and PSS$^-$Na$^+$ species in PSS chains. For the sample with higher doping level, the lineshape of
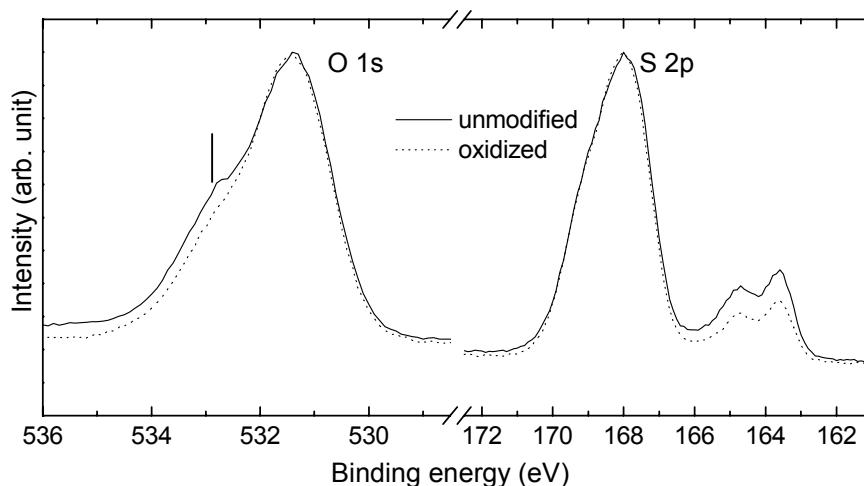
Fig. 5.7 S 2p and O 1s core-level spectra of the PEDT:PSS layers as-prepared and after the electrochemical doping at 0.77 V.

S 2p keeps similar to that for the as-prepared layer. However, the intensity of PEDT component relative to that of PSS is reduced, which should be attributed to the injection of tosylate anions from the electrolyte into the near- surface region. Moreover, the S 2p peak at 168 eV becomes more well- resolved and shifts slightly towards higher BE. This is attributed to the removal of sodium, by which PSS^-Na^+ is converted to the sulfonic acid form (PSSH) so that most of PSS component arises from the PSSH species. On the other hand, the relative intensity of the PEDT component changes only slightly after the reduction process (not shown), indicating the absence of expulsion of PSS^- anions into the electrolyte during the reduction.

The variation of O1s spectra (left part of Fig. 5.7) after electrochemical treatment is consistent with that of the S2p emission. The oxygen component (at 532.8 eV) assigned to the oxygen atom in PEDT, is found to decrease relative to the PSS component at lower BE (531.7 eV) after doping, which can be attributed to the penetration of Tos^- anions. While the lower BE component shifts towards higher binding energy side. This is correlated with the conversion of PSS^-Na^+ into PSSH in the polymer.

From the XPS experiments and other results shown above, some comments will be given on the microscopic process involved in the electrochemical treatment of PEDT:PSS films. Upon doping, Tos^- anions penetrate into the layer to compensate the enhanced positive charge on the PEDT chains, which is shown by the S2p and O1s spectra. However, the channel that the H^+ ions diffuse from the PSSH chain into the electrolyte is also considered to be possible. It will produce more PSS^- repeating units on the PSS chain acting as the counterion. It is not certain whether this channel exists and we also do not know the number ratio of Tos^- to PSS^- repeating units during the doping. On the other hand, the cathodic current during the dedoping should originate from the injection of H^+ cations from the electrolyte rather than the diffusion of PSS^- chains out of the layer because of its large size. This is verified further by the treatment of PEDT:PSS using $N(B_u)_4PF_6$ as supporting electrolyte. During the doping, the value of the anodic current is nearly the same as that using toluesulfonic acid solution at a given potential. However, the cathodic current is reduced by a factor of 2 during the dedoping, because $N(B_u)_4^-$ is a larger ion (and thus less mobile). Its diffusion is more difficult than that of H^+ due to its relatively large size as well as the close-packed PEDT:PSS structure.

The work function of PEDT:PSS films was measured by UPS. Fig. 5.8 (a) shows He I UPS spectra of the layers before and after electrochemical treatment. The binding energy is referenced to the Fermi level (E_F), and the samples were biased at −5.0 V so that the inelastic secondary electron cut-off for the sample could be determined. The spectra reveal the
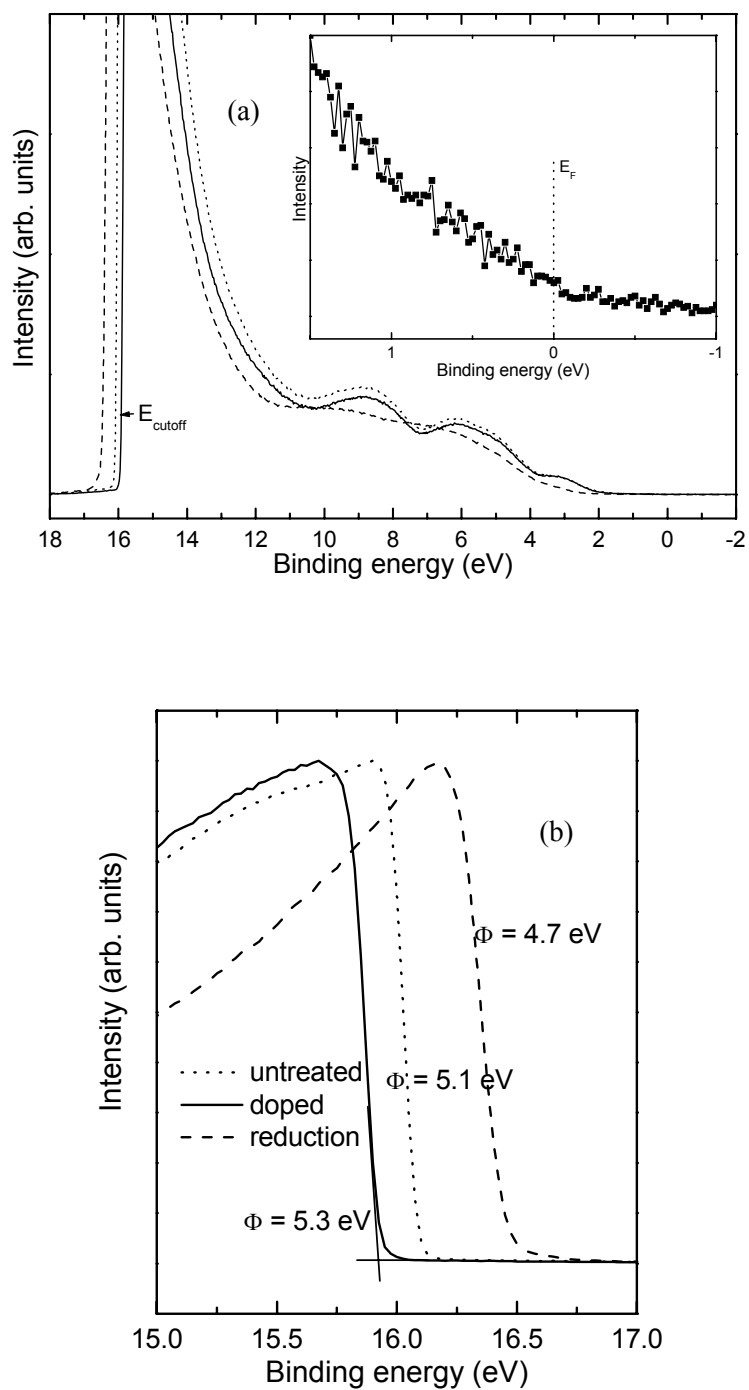
Fig. 5.8 He I UPS spectra of PEDT:PSS from as-prepared as well as those after electrochemical doping (at the potential of 0.77 V, E_{eq} of 0.59 V) and dedoping (at –0.48 V, E_{eq} of 0.02 V): (a) valence band spectra, (b) inelastic second electron cut-offs. The inset shows the Fermi edge from low BE part of the spectrum.

molecular orbital structures at the binding energy above 2 eV, but between 2 eV and the E_F the spectra appear featureless. As seen from the inset of the figure, a finite density of states at Fermi edge was detected which is thus a direct confirmation of the metallic characteristic of PEDT:PSS. The work function ϕ of the sample can be obtained by[183, 184]

$$\phi = h\upsilon - \Delta E \tag{5.2}$$

where $h\upsilon$ is the photon energy and the spectrum width ΔE is determined from the distance between the sample inelastic cut-off (E_{cutoff}) and the Fermi edge. Fig. 5.8 (b) shows the emission cut-offs for as-prepared as well as oxidatively and reductively modified films, respectively. The different cut-off energies indicate the variation of the work function upon the adjustment. The work function of as-prepared layer is 5.1 eV, in good agreement with the value given in the literature[72, 184]. The work function ϕ for further-oxidized sample (E_{eq} of 0.59 V) enhances by 0.2 eV while the ϕ decreases by 0.40 eV for the reduced layer (E_{eq} of 0.02 eV), which is in good agreement with the changes of the E_{eq} values. This unambiguously demonstrates that the work function can be tuned by an electrochemical adjustment of the oxidation level in the PEDT:PSS layers.

5.2.4 Energy level alignment

The work function of PEDT:PSS is independent of that of the underlying ITO substrate upon comparing our UPS results with those in the literatures[72, 185]. This is because the density of charge carriers in highly doped PEDT:PSS (conductivity of *ca.* 10^{-1} S·cm^{-1}) is high enough to allow the equilibration of the Fermi level between the polymer and ITO substrate by means of interfacial charge transfer. Thus PEDT:PSS always aligns to E_F of the ITO with a potential

(a) Before contact   (b) After contact
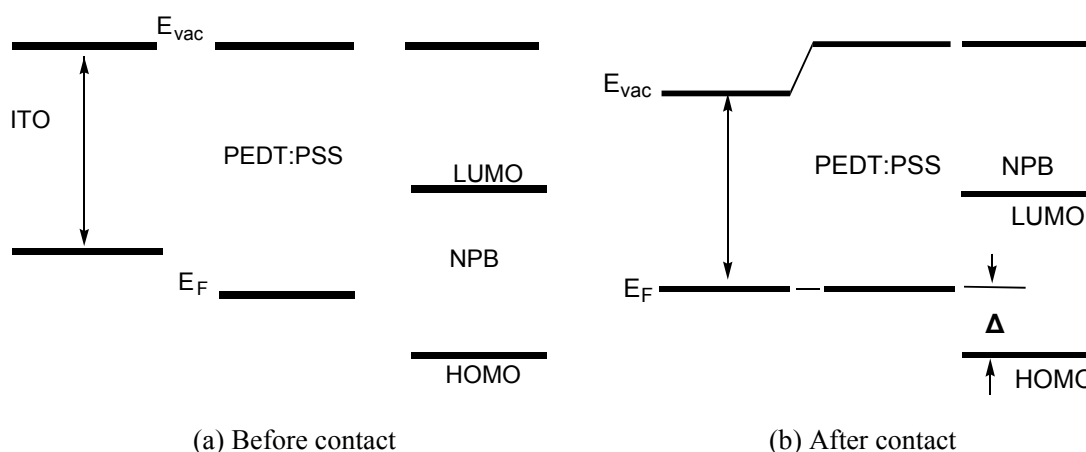
Fig. 5.9 Schematic energy level diagram for an ITO/PEDT:PSS/NPB system (a) before and (b) after the polymer contacts with ITO by which the interface is formed. The barrier for hole injection is denoted by Δ.

drop at the interface which equals to the work function difference as illustrated in Fig. 5.9. The change of work function by the modification of the doping level in the polymer does not influence the alignment of the Fermi level but only the interfacial potential drop. Fig. 5.9 also shows the energy level diagram at the interface between PEDT:PSS and a hole transport layer NPB. The separation of E_F in the polymer and the HOMO level of NPB is the energy barrier for hole-injection. As reported by Mäkinen et al. from UPS measurements[72], the interfacial dipole effect is negligible in PEDT:PSS/small molecule interface thus the vacuum level of PEDT:PSS aligns with that of NPB, i.e. the hole-injection barrier is simply equal to the difference between the HOMO level of NPB and work function of the polymer. Since the work function is enhanced by electrochemical doping, the hole injection barrier should be reduced with the increase of the doping level of PEDT:PSS. For the polymer with a high E_{eq} of 0.59 V, the barrier will be very small (0.2 eV, the HOMO value of NPB is 5.5 eV) and an ohmic contact is almost achieved.

Hole-only devices were prepared to study the influence of electrochemical doping on the hole-injection. A 60 nm PEDT:PSS layer on ITO oxidized at 0.77 V acts as anode. The device structure is ITO/polymer/150 nm NPB/Ag. Fig. 5.10 shows the I-V characteristic of such a device in a log-log plot. A power law dependence is found above the bias of 1.5 V, $I \propto V^{1.93}$, approaching the trap free SCL current (TFSCL)[16, 166] $J_{SCL} \propto V^2$. The inset of Fig. 5.10 gives
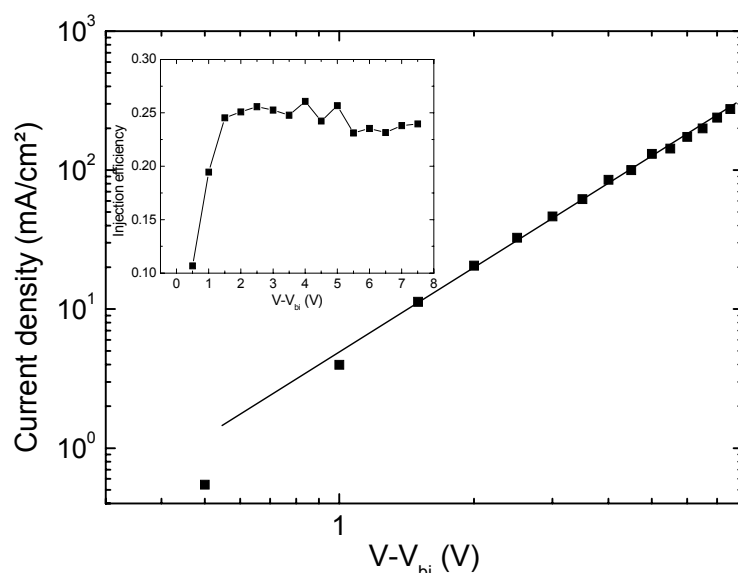
Fig. 5.10 I-V characteristic of a hole- only ITO/PEDT:PSS/NPB/Ag device in a log-log plot. The polymer anode was doped further at the potential of 0.77 V. The thickness of the NPB layer is 150 nm. The solid line shows the TFSCL current calculated for 150 nm of NPB. Inset: injection efficiency of the device. The built-in-potential V_{bi} equals to the difference of the work functions between the polymeric anode (5.3 eV) and Ag cathode (4.3 eV), with a value of 1.0 eV.

the injection efficiency of such a device, which is defined as the ratio of the measured current and the TFSCL current[79]. The mobility is assumed to be 4 x 10^{-4} $cm^2/V \cdot s$ for NPB. The value of the injection efficiency is in the range of 0.2-0.3, nearly 3 orders of magnitude larger than that at an ITO/NPB interface (in Section 4.2.2). It indicates that the injection is close to be ohmic at such a polymer anode/NPB interface due to high ϕ of 5.3 eV for PEDT:PSS. The deviation from the ideal TFSCL value may originate from an insufficient purity of the NPB material (unsublimed), in which the mobility is strongly reduced.

5.3 Effect of electrochemically treated PEDT:PSS on the performance of OLED
5.3.1 NPB/Alq$_3$ bilayer OLED: influence of doping level (E$_{eq}$) on PEDT:PSS

Molecular OLED devices consist a NPB layer with a thickness of 70 nm and a 70 nm thick tri(8-hydroxyquinoline) aluminium (Alq$_3$) layer on electrochemically treated PEDT:PSS/ITO anodes. The thickness of the polymer is 60 nm. A mixture of Mg and Ag (10:1) was used as the cathode. The inset of Fig. 5.11 gives the schematic structure of the devices. The I-L-V characterization was performed *in situ* and in ambient atmosphere.

As shown in Fig. 5.11, the current–voltage (I-V) and luminance-voltage (L-V) characteristics strongly depend on the doping level of PEDT:PSS. The onset of light output and current is reduced monotonously with the increase of the E$_{eq}$ value. The result should be correlated with a systematic decrease of hole injection barrier at the polymer/NPB interface as a result of enhancement of the work function for the PEDT:PSS layer. When the doping level exceeds that of an as-prepared anode, the devices built on these modified anodes gradually show enhanced luminance and a reduction in the operating voltage according to the level of oxidation in the anode. For the anode with the very highly oxidized state (E$_{eq}$ of 0.59 V), the operating voltage of the OLED is reduced by more than 2 V and the luminance improved five-fold at the given voltage, compared to the device on the as-prepared anode. This is attributed to a nearly ohmic transport behavior at such a polymer/NPB interface due to a small hole-injection barrier. In addition, the OLEDs using the PEDT:PSS anodes both as-prepared and with a higher E$_{eq}$, show a remarkable enhancement of current density and EL luminance compared to the devices on a bare ITO anode, a fact which originates from a more favorable work function of these polymeric anodes. Table 5.3 summarizes the performance data of the devices that show a strong dependence on the doping level of electrochemically- treated anodes. The operating voltage is reduced by 3.2V if the E$_{eq}$ value of the anode varies from 0 V to 0.59 V, and correspondingly the luminous efficiency (lm/W) is enhanced nearly twice. It
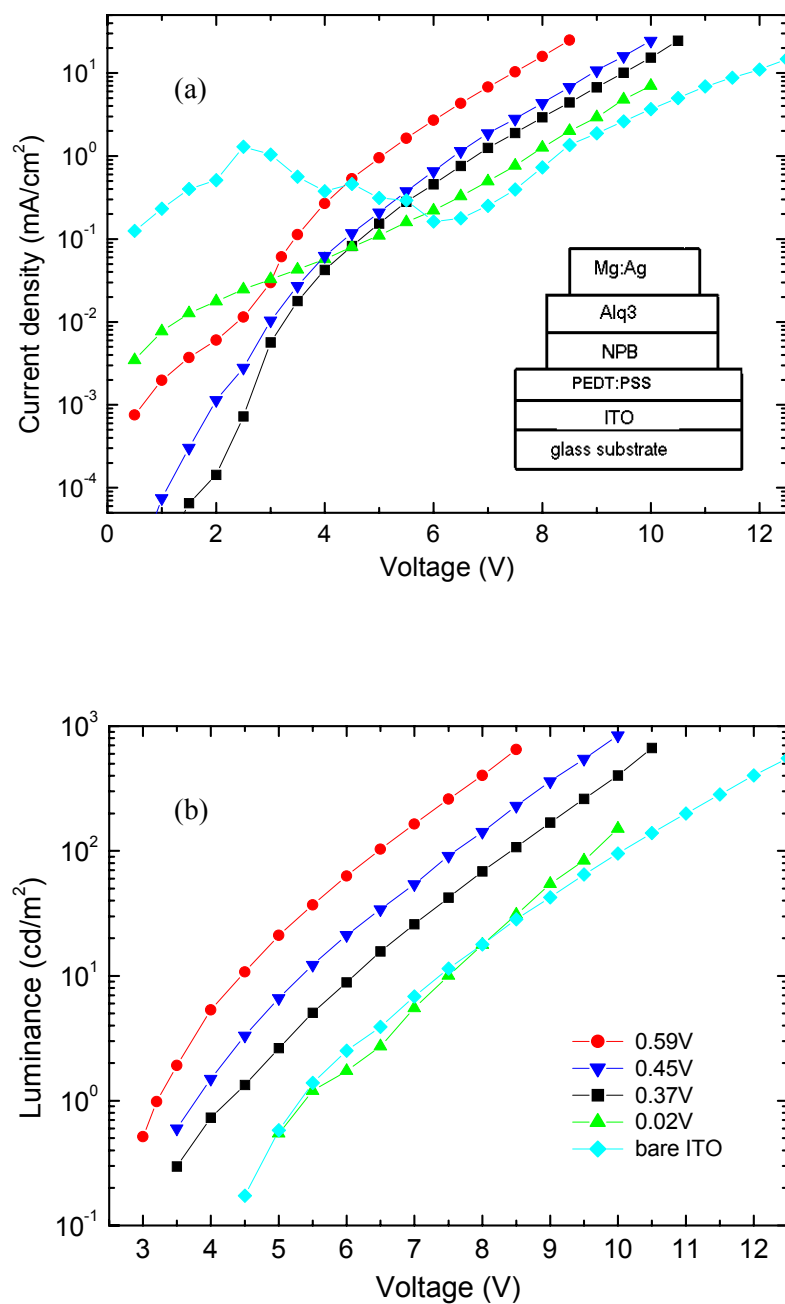
Fig. 5.11 Performance of the OLEDs with a general structure: Modified anode/NPB/Alq$_3$/Mg:Ag: (a) I-V, (b) L-V characteristics. The 60 nm thick PEDT:PSS (on ITO) anodes are adjusted electrochemically to different equilibrium potentials E$_{eq.}$ Inset: OLED structure.

indicates that the modification of doping level of the anode influences not only the hole injection but the recombination efficiency of the OLED.

Table 5.3 Performance of OLEDs built on modified anodes with different E_{eq} values.

E_{eq} of anode (V)	0.59	0.45	0.37	0.02
Turn-on voltage (V) for 1 cd/m²	3.2	3.8	4.3	5.4
Operating voltage (V) for 100 cd/m²	6.5	7.7	8.5	9.7
Current density (mA/cm²) for 100 cd/m²	4.2	3.2	4.1	6.0
EL efficiency (cd/A) for 100cd/m²	2.40	3.25	2.40	2.00
Luminous efficiency (lm/W) for 100 cd/m²	1.16	1.33	0.887	0.64

a. EL efficiency

In Fig. 5.12, the EL efficiency (cd/A) of the devices is plotted vs. the bias voltage. The EL data are corrected accounting for the variation of the PEDT:PSS transmission (see in Fig. 5.5). Devices on the reductively treated anodes show a large reduction of efficiency due to poor hole-injection behavior. For the devices on the anodes with lightly oxidative treatment, the
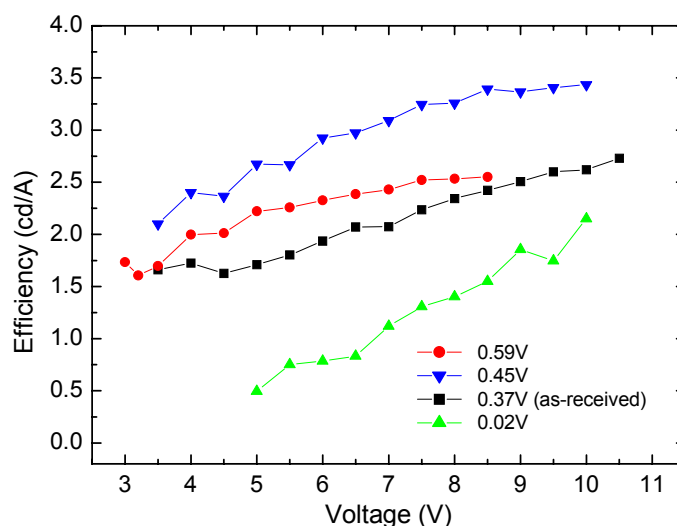
Fig. 5.12 Current efficiency (cd/A) as a function of the bias voltage for different OLEDs shown in Fig. 5.11.

EL efficiency is enhanced obviously and the voltage at which the efficiency maximum is reached shifts to lower bias compared to the device on an unmodified anode. This

enhancement can be explained by the increase in the number of holes injected into the Alq_3 layer so that the recombination probability is increased at a lower bias voltage. However, the maximum efficiency of the devices on highly oxidized anodes (E_{eq} of 0.59 V), 2.6 cd/A, is lower than that of devices with slightly modified anodes (3.4 cd/A). This is caused by excess hole- injection relative to electron injection, which leads to a reduced ratio of the electron/hole numbers. With further optimization, e.g., by the introduction of LiF/Al as the cathode[88], for which electron injection will be remarkably enhanced, a higher EL efficiency is expected.

b. Current-voltage feature

Fig. 5.13 shows the current-voltage curves of the NPB/Alq_3 OLEDs built on the PEDT:PSS/ITO anodes with different doping states (E_{eq}) in a log-log plot. The I-V behavior is very similar for the devices with an oxidatively- modified anode and with an untreated one.
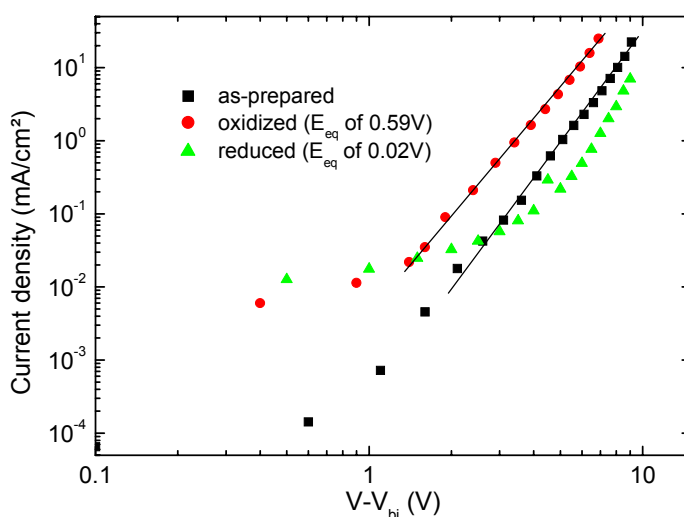
Fig. 5.13 Current-voltage features of the OLEDs on anodes with different oxidation level (E_{eq}) in a double-logarithmic plot. The built-in potential is approximated by the work function difference of the polymeric anode and Mg:Ag cathode.

At high bias, both I-V characteristics follow the space- charge limited (SCL) dependence: $j \propto V^m$, m ~ 6.0-6.5, in analogy to the case using a PbT interlayer. The current is controlled by the trap-limited transport of electrons in the bulk Alq_3. The transition from the low-field ohmic behavior into the high-field one occurs at an effective bias of 1.5-2 V (considering V_{bi}), similar to the case of the PbT-inserted OLEDs, even though the built-in-potentials for the two types of devices are very different (1.4-1.6 V for PEDT devices vs. 0.6 V for PbT devices). However, the I-V curve of the device with a low E_{eq}- anode (E_{eq} of 0 V) cannot be fitted well using the known SCL or injection-limited expressions (R-S thermionic emission, Fowler-Nordheim tunnelling or diode equation). This indicates the complexity at such an injection

contact that may originate from the degradation process in the polymer as well as a possible passivation of the polymer-ITO interface during electrochemical reduction. Further investigation about the influence of the reduction condition (and thus different E_{eq}´s) on the I-L-V feature, should be performed to give a deeper insight in interfacial charge transfer process.

Additionally, it is to be noted that some of the OLEDs using the as-prepared or oxidatively-treated anodes display an injection-limited I-V feature, i.e. R-S thermoionic emission. In these cases, the current and light output are several times lower than those for the 'normal' devices with the same kinds of anodes and then decrease further by one or two orders of magnitude after several voltage sweeps. This is probably related to traces of water in PEDT:PSS which have not been removed during thermal treatment or are absorbed during the transfer of the substrate into the chamber (without inert atmosphere). The chemical reaction occurs between water and the NPB, which leads to an interfacial passivation and thus the degradation of device performance[69]. Therefore, special attention should be paid on the effect of thermal treatment. Also the polymer substrates should be handled in a moisture- free atmosphere to eliminate the content of water.

c. Device stability

Initial lifetime studies were performed on OLEDs with different PEDT:PSS/ITO anodes to test the device stability. The devices were run in dry N_2 atmosphere of the growth chamber under constant voltage. The starting luminance is 400 cd/m² for all devices tested. The bias applied was 10V for the device with the as-prepared polymer anode while it was reduced by 2V if the anode with an E_{eq} of 0.59 was introduced. Fig. 5.14 shows the typical variation in current and luminance as a function of the operating time. During the first one or two minutes of operation, the current and luminance of all samples rise, which is perhaps a heating effect. In the following hours the current and luminance show a decrease. The device with the unmodified anode shows a fast degradation with a decrease in luminance of more than 60% in the first hour. Then a slow degradation occurs. The decrease in the current mimics that in luminance. Such behaviors is similar to that for the molecular PEDT:PSS/TDAPB/Alq$_3$ devices[70] and polymeric PANI/MEH-PPV OLEDs[67]. For the device with a reductively- treated anode, the luminance and current increase roughly by a factor of 2 in the first two minutes of the operation and then decay rapidly manifesting a high instability due to the unfavourable interfacial feature, which is thus not shown in Fig. 5.14.

On the other hand, the OLED on the anode with a high E_{eq} shows a much slower degradation with a loss of starting luminance by *ca.* 25% in the first hour of operation. The

degradation rate is also slightly lower in the following aging than that for the device with an unmodified anode. The improvement of device stability (for the first stage of aging) should be
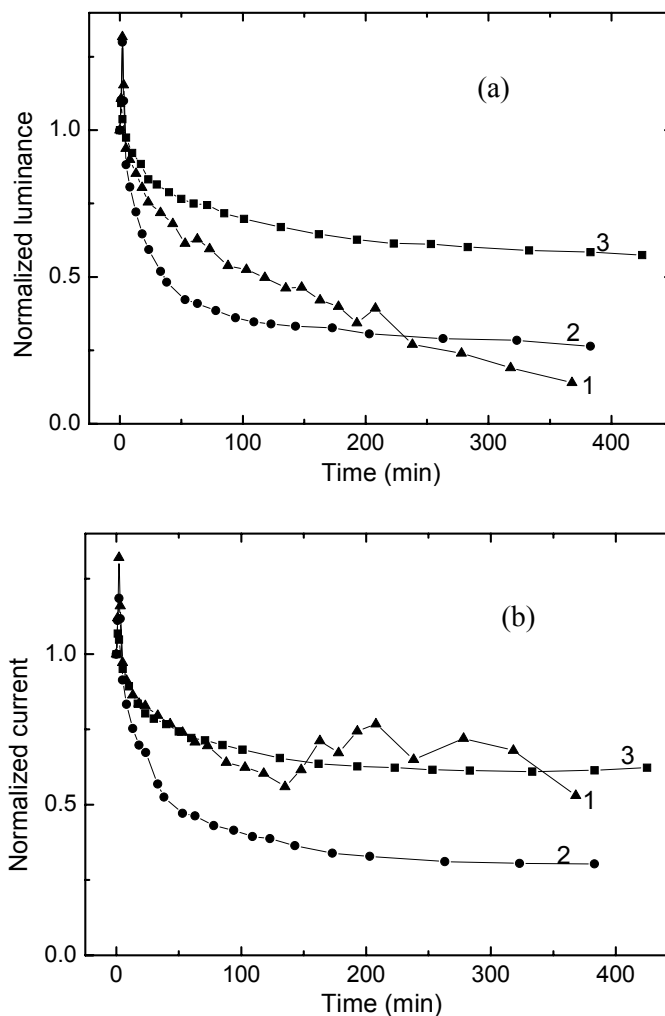
Fig. 5.14 Change in luminance (a) and in current (b) vs. time normalized to the initial value for the OLEDs using different anodes: 1. bare ITO; 2. as-prepared PEDT:PSS/ITO; 3. PEDT:PSS/ITO oxidized further at the potential of 0.77 V.

attributed to the removal of small mobile ions, e.g. sodium ions and possibly H^+ ions from PEDT:PSS by electrochemical treatment. Otherwise, such positive ions will perform an electrophoresis process e.g. field-driven migration from the polymer/organic interface into the NPB layer and thus produce a reverse internal electric field. The electric field will cause a reduction of the effective forward field within the device for the carrier injection and transport, which leads to a decrease of current and luminance. The assumption can be confirmed further if applying a reverse bias voltage on the device with the as-prepared anode and then measuring the luminance and current at forward bias. The EL output is enhanced by

15% upon the bias e.g. at − 4 V for 2 minutes. In this case, the internal electric field formed under the reverse bias has the same direction as the latter forward bias, and thus acts as a positive factor for device performance. The similar behavior has also observed by Zou *et al.* in pristine TPD/Alq$_3$ devices[186] even though the effect is not so pronounced as in our case.

The second stage with a slow degradation rate is related to the growth of dark spots at the cathode that leads to the extension of non-emissive areas. The reduction of the hole injection barrier by increasing the doping level of the anode eliminates the energy dissipation at the polymer/NPB interface. Moreover, the reduction of the electric field by lowering the operating voltage will slow down the electrochemical corrosion process of the cathode upon the operation. These will lead to an enhanced device stability of the OLEDs with higher E_{eq}.

Fig. 5.14 also shows the aging behavior of the OLED using a bare ITO anode. The luminance and current fall continuously and the device keeps only 15% of the initial luminance after 6 hours. Furthermore, when the device is running the current noise is much higher compared to the PEDT:PSS device. The poor stability arises from the dust and imperfection on ITO (see Section 3.5) that causes micro-shorts through the organic layer. In contrast, PEDT:PSS planarizes the ITO surface to cover the dust. No voltage drop across the polymer occurs due to the high conductivity of PEDT:PSS. This leads to a lateral homogeneous current density, reducing the probability for electrical shorts and prolonging the device lifetime.

5.3.2 Improvement of EL efficiency by introducing LiF/Al cathode

As seen from Fig. 5.12, the EL efficiency for the PEDT:PSS devices is very low and even not comparable to the maximum value (4.3 cd/A) for pristine NPB/Alq$_3$ devices. This rises from a relatively insufficient electron injection at the interface between the electron transport layer and cathode. Therefore the enhancement of electron injection will be necessary to improve further the OLED performance. An effective approach is the insertion of an ultrathin lithium-fluoride (LiF) layer between the electron transport layer Alq$_3$ and aluminium cathode introduced first by Hung et al[88], which drastically improves the electron injection. Although the actual mechanism is still not completely clear, two interplays of the process have been proposed: (1) lowering of the work function of aluminium in combination with a monolayer LiF, which makes a better alignment of E_F of Al with the LUMO of Alq$_3$[89]. (2) LiF dissociates by evaporating hot Al atoms on top of LiF, Li atoms diffuse into the underlying organic layer and cause an n-type doping[187, 188]. Furthermore, other highly insulating compounds like MgO, CsF[90] and Lithium oxide[189] also work for this purpose.

At first, the role of LiF/Al cathode is tested by fabricating the OLEDs with an as-prepared PEDT:PSS/ITO anode. LiF was thermally evaporated at a rate of 0.05 nm/s. The thickness of
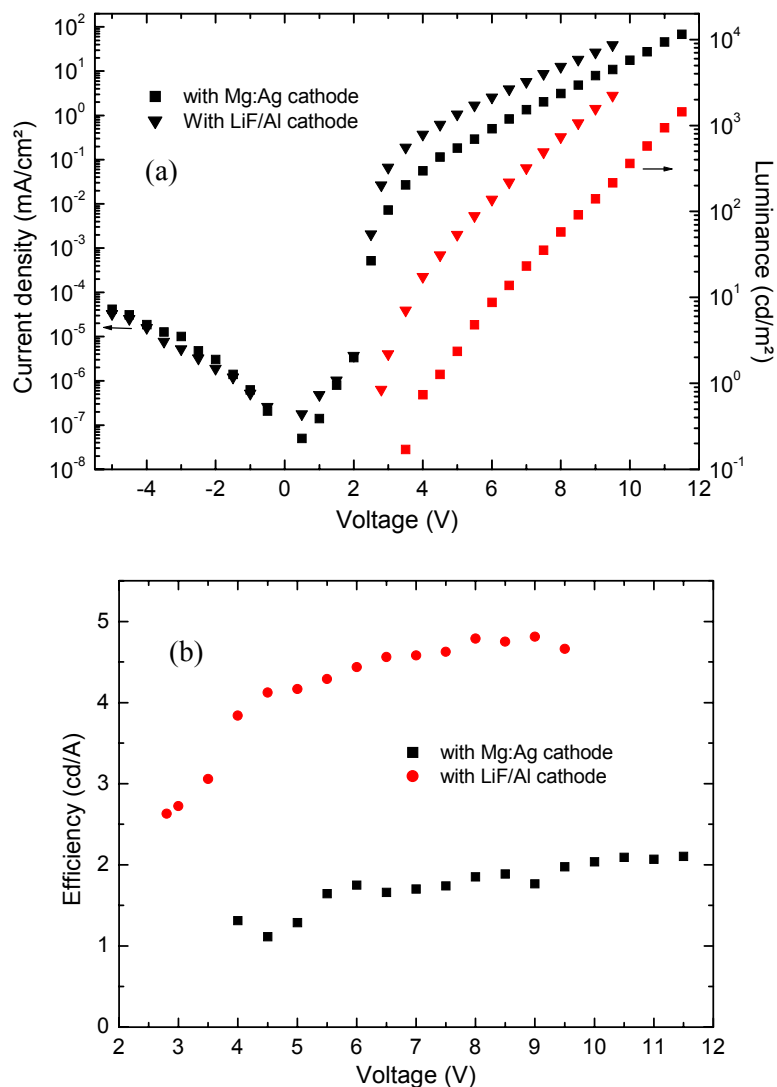
Fig. 5.15 (a) I-L-V, (b) EL efficiency-voltage characteristics of the OLEDs with as-prepared PEDT:PSS/ITO anode and different types of cathodes.

the LiF layer is 0.5 nm. Fig. 5.15 shows the I-L-V characteristics of OLEDs with a LiF/Al and a Mg:Ag cathode, respectively. The onset of luminance decreases to below 3.0 V and the operating voltage is reduced by 3 V via the introduction of LiF instead of Mg:Ag. More notably, the current efficiency (shown in Fig. 5.15 (b)) rises rapidly from the EL onset towards a plateau region. The maximum efficiency increases by a factor of 2 to 5.0 cd/A with respect to the device with a Mg:Ag cathode. The result demonstrates unambiguously that the insertion of a LiF layer improves remarkably the electron injection corresponding to an
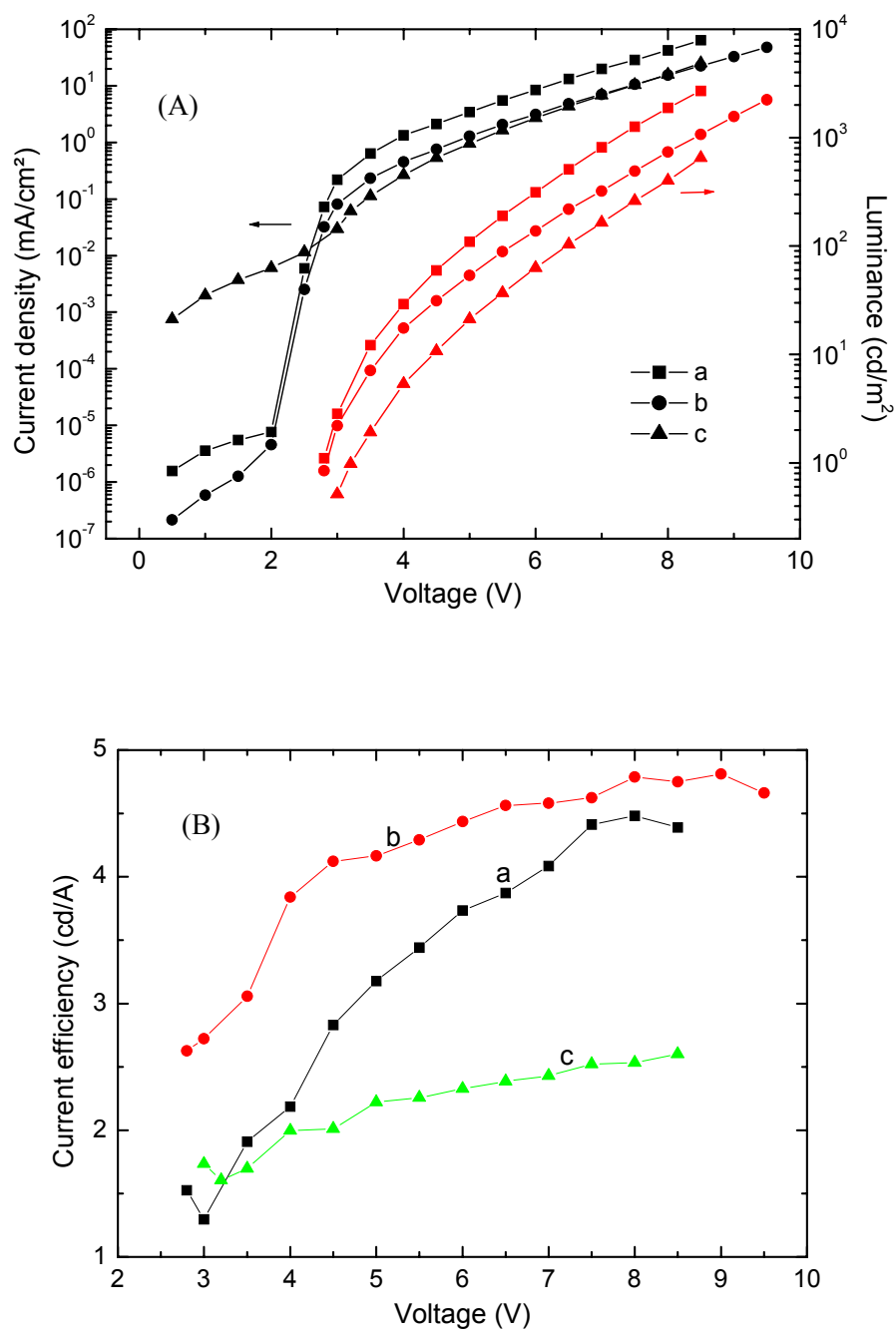
Fig. 5.16 (A) I-L-V, (B) EL efficiency-voltage characteristics of the OLEDs with different combinations of anode and cathode: a) LiF/Al cathode and polymeric anode with a E_{eq} of 0.59 V; b) LiF/Al cathode and as-prepared polymeric anode; c) Mg:Ag cathode and polymeric anode with a E_{eq} of 0.59 V.

efficient hole injection from the PEDT:PSS anode so that a more balanced hole-electron injection and recombination is reached.

To achieve an optimized performance of the device, the further-oxidized PEDT:PSS anode was utilized in combination with the LiF/Al cathode. The I-L-V characteristics are shown in Fig 5.16. The device using a LiF/Al cathode and the anode with a E_{eq} of 0.59 V, displays a further reduction of the operating voltage by 2 V and 1.5 V with respect to the device using an oxidized anode together with Mg:Ag cathode and that using an as-prepared anode combined with LiF/Al, respectively. The onset of light output decreases to 2.8 V and the operating voltage for a luminance of 100 cd/m² is 4.5 V. Although the EL efficiency for such a device is slightly lower compared to the device on an as-prepared anode (shown in Fig 5.16 (B)), the value is still much higher (4.7 cd/A) than that for the device using a Mg:Ag cathode. It indicates that the combination of the high E_{eq}- anode with LiF/Al cathode, i.e. an enhanced injection of holes and electrons, is effective to obtain the optimized OLED performance. On the other hand, the decrease of the current efficiency in such a device implies that the electron injection and transport is still a limiting factor. With a more effective electron transport layer e.g. Li- doped Alq_3[92] or the optimization of the thickness (e.g. a thinner layer) and purity (by train sublimation) of Alq_3, a more balanced charge carrier injection and combination can be achieved. Thus further enhanced efficiency is expected.

As an efficient method for optimizing the properties of a conducting polymer, electrochemical doping has several advantages: (1) It is a well- established procedure in solid-state organic materials and more convenient than other methods, e.g. chemical oxidation/reduction process. (2) The doping level can be adjusted in infinitesimally small steps by simply changing the applied potential of the working electrode. Thus optimised hole injection condition can be achieved. (3) Electrochemical treatment using small counterions is valid for the compact polymer layers from the casting process. The treatment does not alter and roughen the morphology of the polymer surface, which is crucial for devices fabrication. The method can be used to other π- conjugated polymers in general which serve as carrier injection contact in OLED devices. It should be possible to extend the principle, i.e. modification of the oxidation state of p-type doped polymers, to the adjustment of the reduction level of n-type doped polymer cathode that affects the electron injection by a reverse electrochemical process[190].

5.4 Conclusions

The main results on electrochemical treatment of PEDT:PSS, which is utilized as the anode of the molecular OLEDs, are summarized as:

1. The doping level of the compact PEDT:PSS films can be adjusted quantitatively by the electrochemical doping/dedoping process using toluenesulfonic acid as the electrolyte. The diffusion of Tos$^-$ anions and H$^+$ cations is responsible for the charge transfer process.

2. The increase of the doping level causes the enhancement of the work function of PEDT:PSS, which reduces the hole injection barrier at the interface of polymer anode/hole transport layer. An ohmic transport behavior is almost achieved for the anode with a very high doping level.

3. The performance of the OLEDs depends strongly on the oxidation state of the PEDT:PSS/ITO anode. The devices built on the stronger p-type doped polymer anodes show the reduction of operating voltage as well as a remarkable enhancement of the luminance. The stability of such devices is also improved by the removal of the mobile ions in the polymer anode. Furthermore, a combination of an oxidatively modified anode with a LiF/Al cathode reduces further the operating voltage and improves drastically the EL efficiency of OLEDs, which is attributed to a more balanced injection and recombination of holes and electrons.

The results demonstrate that electrochemical treatment is an effective process to optimize the properties of a polymeric anode.

6. Summary and outlook

6.1 Summary

In this work, well-defined and stable thin films based on polythiophene (PT) and its derivative, are employed as a hole-injection contact of organic LEDs. The polymer films are obtained by electropolymerization or electrochemical doping/dedoping of spin-coated layers. Their electrical properties and energy levels are tailored by electrochemical adjustment of their doping levels, in order to improve the hole-injection from the anode as well as the performance of small molecular OLEDs.

The pristine OLED structure is an NPB/Alq_3 bilayer device on a bare ITO anode, which has been prepared by vapor sublimation. The studies on current-luminance-voltage (I-L-V) and electroluminescence (EL) characteristics show that such a device has a high operating voltage (*ca.* 10 V for a luminance of 100 cd/m²) and low luminous efficiency, which is attributed to the very low work function (4.3 eV) of the ITO anode. Moreover, the device displays a strong 'current' instability during the operation due to the existence of a large number of micro-shorts within the organic layer.

A thin polybithiophene (PbT) layer fabricated by electropolymerization, has been used as a hole-injection interlayer in OLED. The morphology, composition, electrochemical properties and energy levels were investigated using different methods (SEM, AFM, XPS and CV). It is found that the film quality of PT can be improved remarkably by using the dimeric thiophene and optimized electrodeposition parameters. The PbT layers produced are well defined and smooth (with a surface roughness of 6-7 nm) up to a thickness of 60 nm. The undoped semiconducting PbT shows a good redox reversibility and chemical stability in air. The layer has a favourable energetic HOMO level of 5.1 eV for hole-injection from ITO into the hole transport layer. Moreover, the semiconducting state can be converted into the conducting oxidized state by electrochemical doping. However, such a p-doped state is less stable compared to the undoped one. Only a low doping level (4.0 %) can be obtained.

For the first time, electrochemically-prepared semiconducting PbT layers have been utilized to prepare the hole-only devices and vapor-deposited bilayer OLEDs. The results from hole-only device show that the hole injection from ITO into the PbT can be described by R-S thermoionic emission mechanism, and PbT has a good hole transport capability. *The introduction of the PbT contact improves remarkably the hole injection between ITO and the hole transport layer NPB*. The NPB/Alq_3 bilayer OLEDs with a thin PbT interlayer show a

remarkable reduction of the operating voltage (by 4V) as well as an enhanced luminous efficiency compared to the devices without PbT. The studies of the influence of the PbT thickness on current efficiency and I-V feature of the OLED, show that an optimum range of the PbT thickness (20-30 nm) exists due to the balance between the requirements of a complete coverage of ITO and the decrease of light absorption by PbT. Within this range, the current efficiency and the principal I-V curves of the devices are unchanged by the introduction of the PbT interlayer compared to the device without PbT. Furthermore, the PbT devices show a remarkable elimination of the leakage current originated from imperfections on bare ITO as well as a higher operating stability, which is attributed to the planarization of anode by PbT. Therefore, *it is demonstrated that the use of an electropolymerization step into the production of vapor deposited molecular OLED is a viable approach to obtain high performance OLEDs.*

The study has been extended to poly(3,4-ethylenedioxythiophene) (PEDT) which has a very low oxidation potential. Highly homogenous poly(styrenesulfonate) (PSS) doped PEDT layers from a spin-coating process have been applied. The doping level of PEDT:PSS was adjusted by an electrochemical redox process using p-tuoluenesulfonic acid as supporting electrolyte to tune the hole injection feature at the polymeric anode/organic interface. Detailed investigations on the variation of morphology, oxidation state and electronic structure of PEDT:PSS during the electrochemical process has shown that *the doping level of PEDT:PSS layers can be controlled quantitatively by an electrochemical doping/dedoping process in spite of its compact morphology.* Moreover the higher oxidation state can remain stable in the dry state. In this redox process, the doping is accompanied by the penetration of tosylate (Tos^-) anions into the polymer or the diffusion of H^+ cations from the PSSH chains of PEDT:PSS into the electrolyte while the dedoping is responsible to an injection of H^+ ions from the electrolyte into the polymer. Notably, such an electrochemical treatment does not affect the surface morphology and homogeneity of the polymer film, even though the reduction leads to a possible degradation of the polymer. The work function of PEDT:PSS is increased further by applying a higher electrode potential than the value of electrochemical equilibrium potential (E_{eq}) of an unmodified film. The value is in line with the change of doping level. This leads to a further reduction of the hole injection barrier at the contact of polymeric anode/hole transport layer. An ideal ohmic behavoir is almost achieved at the anode/NPB interface for a PEDT:PSS anode with a very high doping level (a E_{eq} of up to 0.57 V vs. Ag/AgCl reference), as demonstrated from the hole-only device. It overcomes the limitation related with the PbT interlayer, in which a considerably large barrier for hole injection (0.7-

0.8 eV) at the ITO/PbT interface as well as a voltage drop within the semiconducting layer occurs.

For the first time, molecular OLEDs using an electrochemically adjusted PEDT:PSS/ITO anode have been fabricated. The device performance depends strongly on the doping level of the polymeric anode. The devices on the polymer anode with further oxidation show a reduction of the operating voltage by up to 2V as well as a remarkable enhancement of the luminance. This is attributed to the systematic improvement of hole-injection at the anode/organic interface with the increase of doping level of the polymeric anode. Furthermore, the operating stability of such devices is also improved remarkably especially at the initial stage of the operation. This originates from the removal of mobile ions such as sodium ions inside the PEDT:PSS during electrochemical treatment and thus a hindering of reverse internal field effect, as well as a reduced possibility of microshorts by smoothing the ITO surface. The electron injection is insufficient relative to the excess injection of holes, which leads to an imbalanced number ratio of electrons and holes. Therefore the EL efficiency of the device with heavily oxidized polymer anode is reduced. By utilizing an Al/LiF cathode instead of a Mg:Ag cathode together with the oxidatively modified anode, a balanced injection and recombination of holes and electrons has been achieved successfully. It leads to a further reduction of the operating voltage by 1.5V and a drastic improvement of EL efficiency of the device as high as 5.0 cd/A.

Our results demonstrate unambiguously that the *electrochemical modification of the cast polymer anode is an effective method to improve and optimize the performance of OLEDs*. Its significance lies in the potential of extending the method to other conjugated polymers. The method is valid for the polymers with a closely- packed structure and smooth surface, which is of much importance since well-defined morphology of the organic layer is crucial for device preparation. Besides the use in the fabrication of small molecular OLEDs, the method will be applicable to the fabrication of polymeric OLEDs as well as other devices such as organic transistors and solar cells.

2. Outlook

This work has confirmed the effectiveness of the electrodeposition and the electrochemical adjustment of PT based layers to modify the hole-injection contact in molecular OLEDs. Due to the high structural versatility of PT, various kinds of the derivatives with a thiophene backbone are available by the introduction of different side chains. It is an important task to utilize and develop novel PT- based polymers for the OLED use. PT materials will be

favourable if they have a high chemical and electrochemical stability and a wide range of tunability of the oxidation level by the electrochemical modification. The adhesion and wetting properties of such interlayers with ITO and the hole transport layer have also to be considered. In addition, it will be preferable if solution- processible PT materials are available since the electrochemical tuning of the doping level of a cast interlayer benefits the device performance due to the maintaining of highly homogenous morphology and the achievement of a desirable hole-injection capability of the polymer anode. Soluble PTs can also be used to construct the layer-by-layer films by polyelectrolyte self-assembly. Well-defined nanoscale layers with a good interfacial quality will be obtained. The oxidation level of such layers can be electrochemically adjusted to optimize the charge injection feature.

Since small molecular dopants (Tos$^-$ and PF$_6^-$) have been used for the electrochemical doping process, the dopant diffusion and chemical reaction at the polymer anode/organic interface, together with the operating stability of OLEDs, should be considered due to the relatively high mobility of such a dopant. Utilizing PF$_6^-$ doped PbT as the hole-injection buffer layer in OLEDs, an effort to reduce the injection barrier at the ITO/PbT contact and to enhance the transmission of PbT, has not been successful in the initial investigation. The diffusion of PF$_6^-$ from the doped PbT interlayer into the organic EL layer is expected to be responsible for the quenching of the EL emission. Extensive investigation by UPS/XPS should be performed on the interfacial diffusion of dopants and the doping effect within the hole transport layer near the anode/HTL interface during the deposition of the organic layer. Furthermore, their dependence on the doping level of the polymer anode has to be investigated. These studies will be incorporated with the I-V and impedance spectroscopic characterizations on the electrical properties of the device as a function of the doping state of PbT, in order to clarify the internal mechanism for device failure. For the devices using an oxidatively modified PEDT:PSS/ITO anode, the operating stability for long-time and at enhanced temperature needs to test, in order to investigate the stability of dopant ions retained in the polymer matrix as well as the influence of the dopant's immigration (into the EL layer) on the EL efficiency. It is a subject of further study. Furthermore, larger and even polymeric dopants will be doped in polymeric anodes since they should be more favourable to improve the device stability due to their relative immobility.

In this work, it was demonstrated that p-type doped PT-based polymers can serve as an efficient hole-injection contact in OLEDs. In principle, n-type doping of π-conjugated polymer can also be achieved by an electrochemical reduction of the produced layer. Such layers can be utilized as polymeric cathode to improve electron injection, even though in most

cases the n-doped state is air- and water- sensitive. The reduction level of the polymeric cathode will be adjusted finely by electrochemical process to optimize the electron injection. It is therefore an alternative approach to fabricate highly efficient OLEDs with a reverse layer structure with respect to the 'normal' ones. Such a top-emission OLED will be constructed on a polymer cathode with good electron injection feature by electrochemical reduction. The organic EL layers are deposited consequently by vapor sublimation or spin-cast, and a transparent anode (e.g. ITO) is deposited on top of the organic layer. This type of OLED structure is compatible with the processes for conventional thin transistor circuit, and thus more favourable for most integrated display application.

An other important issue is the further improvement of quantum efficiency of OLEDs. The purification of the organic materials for the carrier transport and emissive layer (such as by train sublimation) is favourable to the improvement of EL efficiency and device stability. However, the more effective approach is at present the introduction of phosphorescent dopants as emitter molecules, which overcomes the spin statistics limiting. Efficient hole injection should be of special importance since the HOMO level of the molecules employed as host matrix for phosphorescent emitter, is generally very low, which will hinder hole injection at the interface of the HTL/ emissive layer. By the insertion of a highly oxidized polymer anode in combination with the utilization of an efficient electron injection and transport layer, a balanced hole-electron recombination and therefore high phosphorescent efficiency and luminance will be achieved at low operating voltage.

References

1. M. Pope, H. Kallman, P. Magnante, J. Chem. Phys. **38**, 2042 (1963).

2. W. Helfrich and W. G. Schneider, Phys. Rev. Lett. **14**, 229 (1965).

3. C. W. Tang and S. A. van Slyke, Appl. Phys. Lett. **51**, 913 (1987).

4. J. H. Burroughes, D. D. C. Bradley, A. R. Brown, R. N. Marks, K. Mackay, R. H. Friend, P. L. Burns, and A. B. Holmes, Nature (London) **347**, 539 (1990).

5. I. D. Park, J. Appl. Phys. **75**, 1656 (1994).

6. D. V. Khramtchenkov, H. Bässler, and V. I. Arkhipov, J. Appl. Phys. **79**, 9283 (1996).

7. Y. Yang and A. J. Heeger, Appl. Phys. Lett. **64**, 1245 (1994).

8. J. C. Scott, P. J. Brock, J. R. Salem, S. Ramos, C. G. Malliaras, S. A. Carter, and L. Bozano, Synth. Met. **111**, 289 (2000).

9. S. Naka, H. Okada, H. Onnagawa, Y. Yamaguchi, T. Tsutsui, Synth. Met. **111-112**, 331 (2000).

10. P. N. Murgatroyd, J. Phys. D: Appl. Phys **3**, 151 (1970).

11. H. Bässler, Phys. Status Solidi B **175**, 15 (1993).

12. J. Staudigel, M. Stößel, F. Steuber and J. Stimmerer, Appl. Phys. Lett. **75**, 217 (1999).

13. J. Staudigel, M. Stößel, F. Steuber, J. Blässing and J. Stimmerer, Synth. Met. **111-112**, 69 (2000).

14. W. Brütting, S. Berleb, A. G. Mückl, Synth. Met. **122**, 99 (2001).

15. P. E. Burrows, Z. Shen, V. Bulovic, D. M. Mccarty, and S. R. Forrest, J. Appl. Phys. **79**, 7991 (1996).

16. M. A. Lampert and P. mark, Current Injection in Solids, Academic Press, New York, 1970.

17. A. Werner, J. Blochwitz, M. Pfeiffer and K. Leo, J. Appl. Phys. **90**, 123 (2001).

18. J. Staudigel, M. Stößel, F. Steuber and J. Stimmerer, J. Appl. Phys. **86**, 3895 (1999).

19. G. G. Malliaras and J. C. Scott, J. Appl. Phys. **85**, 7426 (1999).

20. G. G. Malliaras and J. C. Scott, J. Appl. Phys. **83**, 5399 (1998).

21. P. W. M. Blom, M. J. M. de Jong, and S. Breedijk, Appl. Phys. Lett. **71**, 930 (1997).

22. U. Albrecht and H. Bässler, Chem. Phys. **199**, 207 (1995).

23. U. Albrecht and H. Bässler, Phys. Status Solidi B **191**, 455 (1995).

24. M. Pope and C. E. Swenberg, Electronic processes in organic molecular crystals, Oxford University Press, New York, 1982.

25. C. W. Tang, S. A. van Slyke and C. H. Chen, J. Appl. Phys. **65**, 3610 (1989).

26. J. M. Shi and C. W. Tang, Appl. Phys. Lett. **70**, 1665 (1997).

27. J. C. Scott, S. Karg, and S. A. Carter, J. Appl. Phys. **82**, 1454 (1997).

28. R. H. Parmenter and W. Rupple, J. Appl. Phys. **30**, 1548 (1959).

29. B. K. Crone, I. H. Campbell, P. S. Davids, D. L. Smith, Appl. Phys. Lett. **73**, 3162 (1998).

30. G. G. Malliaras and J. C. Scott, J. Appl. Phys. **84**, 1583 (1998).

31. K. C. Kao and W. Hwang, Electrical Transport in solids, Pergamon Press, Oxford, 1981.

32. S. M. Sze, Physics of Semiconductor Devices, Wiley, New York, 1981.

33. V. I. Arkhipov, E. V. Emelianova, Y. H. Tak, H. Bässler, J. Appl. Phys. **84**, 848 (1998).

34. Y. N. Gartstein and E. M. Conwell, Chem. Phys. Lett. **255**, 93 (1996).

35. U. Wolf, V. I. Arkhipov, H. Bässler, Phys. Rev. B **59**, 7507 (1999).

36. P. S. David, I. H. Campbell, and D. L. Smith, J. Appl. Phys. **82**, 6319 (1997).

37. N. F. Mott and R. W. Gurney, Electronic Processes in Ionic Crystals, Clarendon Press, Oxford, 1940.

38. T. Tsutsui, MRS Bulletin **22**, 39 (1997).

39. M. A. Baldo, D. F. O'Brien, Y. You, A. Shoustikov, S. Sibley, M. E. Thompson, and S. R. Forrest, Nature (London) **395**, 151 (1998).

40. M. A. Baldo, S. Lamansky, P. E. Burrows, M. E. Thompson, and S. R. Forrest, Appl. Phys. Lett. **75**, 4 (1999).

41. N. C. Greenham, R. H. Friend, and D. D. C. Bradley, Adv. Mat. **6**, 491 (1994).

42. A. Kraft, A. C. Grimsdale, and A. B. Holmes, Angew. Chem. Int. Ed. Engl. **37**, 402 (1998).

43. U. Mitschke and P. Bauerle, J. Mater. Chem. **10**, 1471 (2000)

44. M. T. Bernius, M. Inbasekaran, J. O'Brien, and W. Wu, Adv. Met. **12**, 1737 (2000).

45. W. R. Salaneck and J. L. Bredas, Adv. Mat. **8**, 48 (1996).

46. J. L. Bredas, Adv. Mat. **7**, 263 (1995).

47. M. Fahlman, D. Beljonne, M. Lögdlund, A. B. Holmes, R. H. Friend, J. H. Bredas, and W. R. Salaneck, Chem. Phys. Lett. **214**, 327 (1993).

48. P. Dannetum, M. Fahlman, C. Fauquet, K. Kärijama, Y. Sonoda, R. Lazarroni, J. L. Bredas, and W. R. Salaneck, Synth. Met. **67**, 133 (1994).

49. Y. Gao, K. T. Park, and B. R. Hsieh, J. Appl. Phys. **73**, 7894 (1993).

50. P. Bröms, J. Birgersson, N. Johansson, M. Logdlond, and W. R. Salaneck, Synth. Met. **74**, 179 (1995).

51. M. Logdlund and J. L. Bredas, J. Chem.Phys. **101**, 4357 (1994).

52. D. P. Woodruff and T. A. Delchar, Modern Techniques of surface Science, Cambridge

University Press, Cambridge 1986.

53. J. Hölzel, F. K. Schulte, H. Wagner, Solid State Surface Physics, Springer, Berlin, 1979.

54. H. Ishii, K. Sugiyama, D. Yoshimura, E. Ito, Y. Ouchi, and K. Seki, IEEE J. Sel. Top. Quant. Electron. **4**, 24 (1998).

55. H. Ishii, K. Sugiyama, E. Ito, Y. Ouchi, and K. Seki, Adv. Mat. **8**, 605 (1999).

56. S. T. Lee, X. Y. Hou, M. G. Mason, and C. W. Tang, Appl. Phys. Lett. **72**, 1593 (1993).

57. I. H. Campbell, T. W. Hagler, D. L. Smith, and J. P. Ferraris, Phys. Rev. Lett. **76**, 1900 (1996).

58. J. S. Kim, M. Granström, R. H. Friend, N, Johansson, W. R. Salaneck, R. Daik, W. J. Feast, and F. Cacialli, J. Appl. Phys. **84**, 6859 (1998).

59. C. C. Wu, C. I. Wu, J. C. Sturn, and A. Kahn, Appl. Phys. Lett. **70**, 1348 (1997).

60. K. Sugiyama, H. Ishii, Y. Ouchi, and K. Seki, J. Appl. Phys. **87**, 295 (2000).

61. S. A. van Slyke, C. H. Chen, and C. W. Tang, Appl. Phys. Lett. **69**, 2160 (1996).

62. J. Kido and Y. Lizumi, Appl. Phys. Lett. **73**, 2721 (1998).

63. Y. Shirota, Y. Kuwabara, H. Inada, T. Wakimoto, H. Nakada, Y. Yonemoto, S. Kawami, and K. Imai, Appl. Phys. Lett. **65**, 807 (1994).

64. C. Giebeler, H. Antoniadis, D. D. C. Bradley, and Y. Shirota, Appl. Phys. Lett. 72, 2448 (1998).

65. I. G. Hill and A. Kahn, J. Appl. Phys. **86**, 2116 (1999).

66. C. Hosokawa, H. Tokailin, H. Higashi, and T. Kusumoto, Appl. Phys. Lett. **67**, 3853 (1995).

67. S. Karg, J. C: Scott, J. R. Salem, M. Angelopoulos, synth. Met. **80**, 111 (1996).

68. S. A. Carter, M. Angelopoulos, S. Karg, P. J. Brock, and J. C. Scott, Appl. Phys. Lett. **70**, 2067 (1997).

69. Y. Cao, G. Yu, C. Zhang, R. Menon, and A. J. Heeger, Synth. Met. **87**, 171 (1997).

70. A. Elschner, F. Bruder, H. –W. Heuer, F. Jonas, A. Karbach, S. Kirchmeyer, S. Thurm, and R. Wehrmann, Synth. Met. **111-112**, 139 (2000).

71. T. M. Brown, J. S. Kim, R. H. Friend, F. Cacialli, R. Daik, and W. J. Feast, Appl. Phys. Lett. **75**, 1679 (1999).

72. A. J. Mäkinen, I. G. Hill, R. Shashidlar, N. Nikolov, and Z. H. Kafafi, Appl. Phys. Lett. **79**, 557 (2001).

73. J. Cui, Q. Huang, Q. Wang, and T. J. Marks, Langmuir, **17**, 2051 (2001).

74. J. Cui, Q. Huang, J. G. C. Veinot, H. Yan, and T. J. Marks, Adv. Mat. **14**, 565 (2002).

75. Z. B. Deng, X. M. Ding, S. T. Lee, W. A. Gambling, Appl. Phys. Lett. **74**, 2227 (1999).

76. X. M. Ding, L. M. Hung, L. F. Cheng, Z. B. Deng, X. Y. Hou, C. S. Lee, and S. T. Lee, Appl. Phys. Lett. **76**, 2704 (2000).

77. W. Hu, K. Manabe, T. Furukawa, and M. Matsumra, Appl. Phys. Lett. **80**, 2640 (2002).

78. I. M. Chan, T. Y. Hsu, and F. C. Hong, Appl. Phys. Lett. **81**, 1899 (2002).

79. Y. Shen, D. B. Jacobs, G. G. Malliaras, G. Koley, M. G. spencer, and A. Ioannidis, Adv. Mater. **13**, 1234 (2001).

80. D. E. O'Brien, P. E. Burrows, S. R. Forrest, B. E. Koene, D. E. Loy, and M. E. Thompson, Adv. Mat. **10**, 1108 (1998).

81. S. Tokito, H. Tanaka, A. Okada, and Y. Taga, Appl. Phys. Lett. **69**, 878 (1996).

82. A. Yamamori, C. Adachi, T. Koyama, and Y. Taniguchi, Appl. Phys. Lett. **72**, 2147 (1998).

83. F. Huang, A. G. Macdiarmid, and B. R. Hsieh, Appl. Phys. Lett. **71**, 2415 (1997).

84. C. Ganzorig and M. Fujihira, Appl. Phys. Lett. **77**, 4211 (2000).

85. J. Blochwitz, M. Pfeiffer, T. Fritz, and K. Leo, Appl. Phys. Lett. **73**, 729 (1998).

86. J. Huang, M. Pfeiffer, A. Werner, J. Blochwitz, and K. Leo, Appl. Phys. Lett. **80**, 139 (2002).

87. X. Zhou, M. Pfeiffer, J. Blochwitz, A. Werner, A. Nollau, T. Fritz, and K. Leo, Appl. Phys. Lett. **78**, 410 (2001).

88. S. Hung, C. W. Tang and M. G. Mason, Appl. Phys. Lett. **70**. 152 (1997).

89. S. E. Shaheen, G. E. Jabbour, M. M. Moorrell, Y. Kawabe, B. Kippelen, N, Peyghambarian, M. – F. Nabor, R. Schlaf, E. A. Mash and N. R. Armstrong, J. Appl. Phys. **84**, 2324 (1998).

90. P. Piromreun, H. Oh, Y. Shen, G. G. Malliaras, J. C. Scott, and P. J. Brock, Appl. Phys. Lett. **77**, 2403 (2000).

91. Z. Liu, O. V. salata, and N. Male, Synth. Met. **128**, 211 (2002).

92. J. Kido, T. Matsumoto, Appl. Phys. Lett. **73**, 2866 (1998).

93. J. Kang, D. S. Park, S. Y. Kim, C. N. Whang, K. Jeong, and S. Im, Appl. Phys. Lett. **81**, 2581(2002).

94. C. Adachi, T. Tsutsui, and S. Saito, Appl. Phys. Lett. **55**, 1489 (1989).

95. Y. Hamada, IEEE Transactions: Electron Devices **44**, 1208 (1997).

96. B. T. Chen, W. Y. Lai, Z. Q. Gao, C. S. Lee, S. T. Lee, and W. A. Gambling, Appl. Phys. Lett. **75**, 3252 (1999).

97. C. Adachi, M. A. Baldo, S. R. Forrest, and M. E. Thompson, Appl. Phys. Lett. **77**, 904 (2000).

98. M. Ikai, S. Tokito, Y. Sakamoto, T. Suzuki, Y. Taga, Appl. Phys. Lett. **79**, 156 (2001).

99. G. He, S. C. Chang, F. C. Chen, Y. Li, and Y. Yang, Appl. Phys. Lett. **81**, 1509 (2002).

100. C. Adachi, M. A. Baldo, M. E. Thompson, and S. R. Forrest, Appl. Phys. Lett. **90**, 5048 (2001).

101. D. Lacey, 9th International Workshop on Inorganic and Organic Electroluminescence, Oregen, Bend, USA, September, 13-17, 1998.

102. Y. He, S. Gong, R. Hattori, and J. Kanicki, Appl. Phys. Lett. **74**, 2265 (1999).

103. H. Becker, H. Spreitzer, W. Kreuder, E. Kluge. H. Schenk, and Y. Cao, Adv. Mat. **12**, 42 (2002).

104. Cambridge Display technology Homepage, http:// www.cdtltd.co.uk (accessed May 2002).

105. J. Scherbel, P. H. Ngugen, G. Passsch, W. Brütting, and M. Schwoerer, J. Appl. Phys. **83**, 5045 (1998).

106. V. R. Nikitenko, V. I. Arkhipov, Y. –H. Tak, J. Pommerehne, H. Bässler, H. –H, Hörhold, J. Appl. Phys. **81**, 7514 (1997).

107. E. I. Haskal, M. Büchel, P. C. Duineveld, A. Sempel, and P. van de Weijer, MRS bulletin **27**, 864 (2002).

108. H. Ochi, S. Kawami, H. Ohata, K. Nagayama, R. Murayama, Y. Okuda, H. Nakada, T. Tohma, T. Naito, H.Abiko, J. SID 5, 235 (1997

109. Pioneer Electronic Corporation Press Release, Sept. 28, 1998 (www.pioneer.co.jp/press/index-e.html).

110. EDEX2002, Tokey, 2002.

111. Handbook of Conducting Polymers, 1st ed. ed. T. A. Skotheim, MARCEL DEKKER, New York 1986.

112. Q. B. Pei, G. Yu, C. Zhang, Y. Yang, and A. J. Heeger, Science **269**, 1086 (1995).

113. S. Destri, U. Giovanella, A. Fazio, W. Porzio, G. Salerno, G. Zotti, Proceeding of 1st European Conference on Organic Electronics and Related Phenomen, Nov. 2001, Potsdam, Germany, p96.

114. M. Gross, D. C. Müller, H. –G. Nothofer, U. Scherf, D. Neher, C. Bräuche, and K. Meerholz, Nature (London), **405**, 661 (2000).

115. F. Chao, M. Costa, and C. Tian, Synth. Met. **53**, 127 (1993).

116. F.Li and W. J. Albery, Electrochimica Acta **37**, 393 (1992).

117. G. Li, M. Josowicz, and Jiri, Janata, Synth. Met. **125**, 273 (2002).

118. D. B. Romero, M. Schaer, L. Zuppiroli, B. Cesar, B. Francois, Appl. Phys. Lett. 67, 1659

(1995).

119. P. J. Brown, H. Sirringhaus, and R. H. Friend, Synth. Met. **101**, 557 (1999).

120. A. Tsumura, H. Koezuka, and T. Ando, Appl. Phys. Lett. **49**, 1210 (1987).

121. D. M. Taylor, H. L. Gomes, A. E. Underhill, S. Edge, and P. I. Clemenson, J. Phys. D: Appl. Phys. **24**, 2032 (1991).

122. R. Valaski, L. M. Moreira, L. Micaroni, I. A. Hümmelegen, J. Appl. Phys. **92**, 2035 (2002).

123. W. Bantikassegn, O. Inganäs, Thin Solid Films **293**, 138 (1997).

124. A. J. Bard and L. R. Faulkner, Electrochemical Methods: Fundamentals and Applications (2nd Ed.) (Wiley, New York, 2001).

125. D. T. Sawyer, W. R. Heineman and J. M. Beebe, Chemistry Experiments for Instrumental Methods (Wiley, New York, 1984) p.77.

126. J. L. Brédas, R. Silbey, D. S. Boudreux and R. R. Chance, J. Am. Chem. Soc. **105,** 6555 (1983).

127. R. Cervini, X. –C. Li, G. W. C. Spencer, A. B. Holmes, S. C. Moratti and R. H. Friend, Synth. Met. **84**, 359 (1997).

128. E. M. Genies, G. Bidan and A. Diaz, J. Electrochem. Soc. **149**, 101 (1983).

129. G. Tourillon and F. Garnier, J. Electroanal. Chem. **135**, 173 (1982).

130. R. J. Waltman, A. F. Diaz and J. Bargon, J. Electrochem. Soc. **131**, 1452 (1994).

131. M. Dietrich and J. Heinze, J. Electroanal. Chem. **369**, 87 (1994).

132. Q. Pei, G. Zuccarello, M. Ahluskog and O. Inganäs, Polymer **35**, 1347 (1994).

133. G. Zotti, M. C. gallazzi, G. Zerbi, S. V. Meille, Synth. Met. **73**, 217 (1995).

134. H. Randriamahazaka, V. Nöel, C. Chevrot, J. Electroanal. Chem. **103-111**, 472 (1999).

135. R. Schrebler, P. Grez, P. Cury, C. Veas, M. Merino, H. Gomez, R. Cordora, M. A. Der valle, J. Electroanal. Chem. **430**, 77 (1997).

136. S. Z. Xing, M. Fahlman, X. W. Chen, O. Inganäs, W. R. Salaneck, Synth. Met. **89**, 161 (1997).

137. F. Papadimitrakopoulos, X. M. Zhang, D. L. Thomsen, K. A. Higginson, Chem. Mater. **8**, 1363 (1996).

138. T. Mori, K. Miyachi, T. Kichimi and T. Mizutani, Jpn. J. Appl. Phys. Pt. 1 **33**, 6594 (1994).

139. A. Rajagopal, C. I. Wu and A. Kahn, J. Appl. Phys. **83**, 2649 (1998).

140. T. Chasse, C. I. Wu, I. G. Hill and A. Kahn, J. Appl. Phys. **85**, 6589 (1999).

141. C. Hosokawa, H. Tokailin, H. Higashi, T. Kusumoto, Appl. Phys. Lett. **60**, 1220 (1992).

142. K. Seri, E. Ito and H. Ishii, Synth. Met. **91**, 137 (1997).

143. R. G. Kepler, P. M. Beeson, S. J. Jacobs, R. A. Anderson, M. b. Sinclair, V. S. Valencia, P. A Cahill. Appl. Phys. Lett. **668**, 3618 (1995).

144. G. G. Malliaras, Y. Shen, D. H. Dunlap, H. Murata, Z. H. Kafafi, Appl. Phys. Lett. **79**, 2582 (2001).

145. M. G. Mason, L. S. Hung, C. W. Tang, S. T. Lee, K. W. Wong and M. wang, J. Appl. Phys. **86**, 1688 (1999).

146. F. Nüesch, E. W. Forsythe, Q. T. Le, Y. Gao and L. T. Rothherg, J. Appl. Phys. **87**, 7973 (2000).

147. H. Vestweher and W. Rieß, Synth. Met. **91**, 181 (1997).

148. P. E. Burrows and S. R. Forrest, Appl. Phys. Lett. **64**, 2285 (1994).

149. J. C. Scott, J. H. Kaufmann, P. J. Brock, R. Dipietro, J. Salem, J. A. Goitia, J. Appl. Phys. **79**, 2745 (1996).

150. S. Berleb, W. Brütting, M. Schwoerer, Synth. Met. **102**, 1034 (1999).

151. V. Cimrova, D. Neher, synth. Met. **76**, 125 (1996).

152. J. Tarabek, M. Wolter, P. Rapta, W. Plieth, M. Maumy, L. Dunsch, Macromol. Symp. **169**, 219 (2001)

153. A. R. Hillman and E. F. Mallen, J. Electroanal. Chem. **220**, 351 (1987).

154. R. J. Waltman, J. Bargon, and A. F. Diaz, J. Phys. Chem. **87**, 1459 (1983).

155. R. Schrebler, P. Grez, P. Cury, C. Veas, M. Merino, H. Merino, H. Gómez, R. Córdova, M. A. del Valle, J. Electroanal. Chem. **430**, 77 (1997).

156. A. F. Diaz and K. K. Kanazawa, Extended linear chain compound (G. S. Miller Ed.), Plenum, New York, 1982.

157. D. Briggs, M. P. Seah, Practical Surface Analysis, Wiley, New York, 1990.

158. N, C. Greenham and R. H. Friend, Solid State Phys. 1995.

159. Handbook of Chemistry and Physics, CRC, Boca Raton, FL, 1988.

160. M. A. Baldo and S. R. Forrest, Phys. Rev. B **64**, 085201 (2001).

161. C. D. Dimitrakopoulos and P. R. L. Malenfant, Adv. Mater. **14**, 99 (2002).

162. R. Valaski, L. M. Moreira, L. Micaroni, and I.A. Hümmelgen, J. Appl. Phys. **92**, 2035 (2002).

163. L. –B. Lin, R. H. Young, M. G. Mason, S. A. Jenekhe, and P. M. Borsenberger, Appl. Phys. Lett. **72**, 864 (1998).

164. J. R. Macdonald, Impedance Spectroscopy, Wiley, New York, 1987.

165. H. Peisert, M. Knupfer, T. Schwieger, and J. Fink, Appl. Phys. Lett. **80**, 2916 (2002).

166. H. Antoniadis, J. N. Miller, D. B. Roitman, I. H. Campbell, IEEE Trans. Electron Devices **44**, 1289 (1997).

167. B. Rushstaller, S. A. Carter, S. Barth, H. Riel, W. Riess, J. C. Scott, J. Appl. Phys. **89**, 4575 (2001).

168. C. Kvarnström, H. Neugebauer, S. Blomquist, H. J. Ahonen, J. Kankare, and A. Ivaska, Electrochimica Acta **46**, 871 (2001).

169. F. Zhang, A. Petr, L. Dunsch, unpublished results.

170. Bayer AG, Eur. Patent 440957, 1991.

171. F. Jonas, W. Krafft, B. Muys, macromol. Symp. **100**, 169 (1995).

172. T. Grandlund, L. A. A. Pettersson, and O. Inganäs, J. Appl. Phys. **89**, 5897 (2001).

173. W. H. Kim, A. J. Mäkinen, N. Nikolov, R. Shashidhar, H. Kim, and Z. H. Kafai, Appl. Phys. Lett. **80**, 3844 (2002).

174. T. A. Skotheim, Handbook of Conducting Polymers, Dekker, New York 1998.

175. Bayer, Baytron P, Product information, http:// www.bayer-echemicals.com/products/electronic.

176. M. Lapkowski, E. Vieil, Synth. Met. **109**, 199 (2000).

177. D. W. Hatchett, M. Josowicz, J. Janata, J. Phys, Chem. B **146**, 10992 (1999).

178. P. K. H. Ho, J. S. Kim, J. H. Burroughes, H. Becker, S. F. Y. Li, T. M. Brown, F. Cacialli and R. H. Friend, Nature (London) **404**, 481 (2000).

179. J. L. Bredas, F. Wudl, A. J. Heeger, Solid State Commun. **59**, 415 (1989).

180. S. Garreau, J. L. Duvail, G. Louarn, Synth. Met. **125**, 325 (2002).

181. G. Grezynski, Th. Kugler and W. R. Salaneck, Thin Solid Films **354,** 129 (1999).

182. G. Grezynski, Th. Kugler, M. Keil, W. Osikowicz, M. Fahlman and W. R. Salaneck, J. Electron Spectrosco. Relat. Phenom. **121**, 1 (2001).

183. G. Ert and J. Küppers, Low Energy Electrons and Surface Chemistry, VCH, Weinheim 1985.

184. Y. Park, V. Choong, Y. Gao, B. R. Hsieh, C. W. Tang, Appl. Phys. Lett. **68**, 2699 (1996).

185. Th. Kugler, W. R. Salaneck, H. Rost and A. B. Holmes, Chem. Phys. Lett. **310**, 391(1999).

186. D. Zou, T. Tsutsui, J. Appl. Phys. **87**, 1951 (2001).

187. H. Heil, J. Steiger, S. Karg, M. Gastel, H. Ortner, H. V. Seggern, J. Appl. Phys. **89**, 1103 (2001).

188. M. G. Mason, C. W. Tang, L. Hung, P. Raychaudhuri, J. Madathil, D. J. Giesen, L.Yan,

Q. Le, Y. Gao, S. T. Lee, L. S. Liao, L. F. Cheng, W. R. Salaneck, D. A. dos Santos, J. L. Bredas, J. Appl. Phys. **89**, 2756 (2001).

189. T. Tsutsui, M. Yang, M. Yahrio, K. Nakamura, T. Watanabe, T. Tsuiji, Y. Fukuda, T. Wakimoto, S. Miyaguchi, Jpn. J. Appl. Phys. Pt. 2, **38** L1502 (1999).

190. E. Naudin, P. Dabo, D. Guay, D. Belanger, Synth. Met. **132**, 71 (2002).

List of some important abbreviations in this thesis

AFM   atomic force microscopy
Ag/AgCl   silver-silver chloride electrode
Alq_3 tri(8-hydroxyquinolinato) aluminium
BE   binding energy
bT   2,2'-bithiophene
C   capacitance
CuPc   copper phthalocynanine
CV   cyclic voltammogram
d   thickness of sample
EA   electron affinity
E_{eq} electrochemical equilibrium potential
E^0 standard potential of the redox couple
$E^{0'}$ formal potential of the redox couple
E_F Fermi level
E_g energy gap
EL   electroluminescence
E_{onset}^{ox} onset potential of oxidation
E_{onset}^{red} onset potential of reduction
E_{pa} anodic peak potential
E_{pc} cathodic peak potential
E_t characteristic trap energy
ETL   electron transport layer
F   electric field
F_c/F_c^+ ferrocene/ferrocenium
FN   Fowler-Nordheim model
HOMO   highest occupied molecular orbital
HTL   hole transport layer
Im (Z)   image part of impedance
IP   ionization potential
ITO   indium-tin oxide
I-V   current-voltage feature of OLED
J   current density
L   luminance
L-V   luminance-voltage feature of OLED
LED   light emitting diode
LiF/Al   lithium fluoride/Aluminium
LUMO   lowest unoccupied molecular orbital
$\mu_{(h, e)}$ mobility of (hole, electron)
$N(Bu)_4PF_6$ tetrabutylammonium hexafluorophosphate

NHE	normal hydrogen electrode
n(p)	number density of holes (electrons)
NPB	N, N'-bis(naphthalen-1-yl)-N, N'-diphenyl-benzidine
N_t	density of trap
δ	doping level
η_c	current efficiency of OLED (cd/A)
η_P	luminous efficiency of OLED (lm/W)
η_Q	quantum efficiency (%)
ϕ	work function
ψ_e	radiant flux
ψ_V	luminous flux
Δ	energy barrier for charge carrier injection
OCP	open circuit potential
OLED	organic light-emitting diode
PbT	polybithiophene
PEDT	poly(3,4-ethylenedioxythiophene)
PL	photoluminescence
PSS	poly(styrensulfonate)
PT	polythiophene
Q	charge amount
Re (Z)	real part of impedance
R-S	Richardson-Schottky (injection)
SCE	saturated calomel electrode
SCLC	space charge limited current
SEM	scanning electron microscope
TCL	trap charge limited
TFSCL	trap-free space charge limited
T_g	glass transition temperature
Tos^-	tosylate anion
TPD	N, N'-bis(3-methylphenyl)-N, N'-bis-(phenyl)-benzidine
TSC	thermally stimulated current
UPS	ultraviolet photoelectron spectroscopy
UV-vis	ultraviolet-visible
V_{bi}	built-in-potential
$V(\lambda)$	photopic function
XPS	x-ray photoelectron spectroscopy
$Z(\omega)$	impedance at frequency ω

Acknowledgement

First of all, I want to thank my supervisors, Prof. Jörg Fink for his clear advice and financial support and Prof. Lothar Dunsch for a lot of instruction in the scientific method and critical discussions with me. Their advice as well as earnest and strict attitude towards to the scientific work will benefit me forever.

I want to thank Dr. Andreas Petr, who taught me how to use the necessary equipments and made many helpful discussions with me about the experimental work.

My thanks are also due to other former and present collaborators in our group: Frank Ziegs, Heide Zöller, Uwe Kirbach, Uwe Büttner, Pavel Janda, Brunhild Schaudert, Matthias Krause, Christine Malbrich, Petra Georgi, Cunru Wang and Jan Tarabek for their friendly assistance in the experimental work.

I acknowledge Dr. Heiko Peisert and Dr Steffen Oswald (in IFW) for the XPS/UPS measurement and Sieglinde Pichl for SEM observation. To Prof. Gernot Paasch, I am thankful for many stimulating discussions.

Thank all my friends and relatives for their personal support during my Ph.D work.

List of publications for the work:

1. F. Zhang, A. Petr, and L. Dunsch, Electrochemically-doped polymeric anode for improving the performance of molecular organic light-emitting diodes, *Applied Physics Letter*, **82**, 4587 (2003).

2. F. Zhang, A. Petr, U. Kirbach, and L. Dunsch, Improved hole injection and performance of multilayer OLED devices by electrochemically prepared- polybithiophene layers, *Journal of Materials Chemistry*, **13**, 265 (2003).

3. F. Zhang, A. Petr, H. Peisert, M. Knupfer, and L. Dunsch, Electrochemical variation of energy levels of poly(3,4-ethylenedioxythiophene):poly(styrenesulfonate), *Chemistry of Materials* (submitted)

4. H. Peisert, M. Knupfer, F. Zhang, A. Petr, L. Dunsch, and J. Fink, Charge transfer and doping at technically relevant organic/organic interfaces, *Applied Physics Letter*, **83**, 3930 (2003)

5. A. Petr, F. Zhang, H. Persert, M. Knupfer, L. Dunsch and J. Fink, Electrochemical adjustment of the work function of a conducting polymer, *Chemical Physics Letter*, **385**, 140 (2004).

6. H. Peisert, M. Knupfer, F. Zhang, A. Petr, L. Dunsch, and J. Fink, The interface between phthalocyanines and PEDOT:PSS: evidence for charge transfer and doping, *Surface Science* (submitted).

7. F. Zhang, A. Petr, U. Kirbach, and L. Dunsch, Effect of electrochemically prepared-polybithiophene layers on hole injection and performance of mutilayer OLED devices, Proceedings of 1st European Conference on organic electronics and related phenomena 2001 (ECOER'01) Nov. 2001, Potsdam, Germany, p.137.

8. F. Zhang, A. Petr, and L. Dunsch, Polymeric PEDT:PSS anode for improving hole-injection and performance of multilayer OLEDs, Proceedings of annual meeting of German Physics Society (DPG 2002), Mar. 2002, Regensburg, Germany, p. 492.

Curriculum vitae

Fapei Zhang

Personal information

Date of birth: Jul. 24, 1969
Place of birth: Anhui, P. R. China
Nationality: P. R. China

Education

- February 2000 to present   Ph.D student in physics at Leibniz-Institut für Festkörper- und Werkstoffforschung Dresden (enrolled in Technischen Universität of Dresden), Dresden.

- September 1991 - August 1994   Graduate student at Institute of Solid State Physics, Chinese Academy of Science, Hefei, P. R. China
M. S. in Physics, August 1994

- September 1987 - July 1991   Undergraduate student at Department of Physics, Anhui University, Hefei, P. R. China
B. S. in physics, July 1991

Work experience

- February 2000 - February 2003   A scientific researcher (Doktorand, BAT) at Leibniz-Institut für Festkörper- und Werkstoffforschung Dresden, Dresden.

- September 1994-December 1999   A scientific researcher at National Synchrotron Radiation Laboratory, University of Science and Technology of China, Hefei, P. R. China

Eidesstattliche Erklärung

Ich erkläre an Eides statt, dass ich die vorliegende Dissertation selbständig und ohne fremde Hilfe verfasst, andere als die angegebenen Quellen und Hilfsmittel nicht benutzt bzw. die wörtlich oder sinngemäß entnommenen Stellen als solche kenntlich gemacht habe.

Dresden, August 2003   M.S. Fapei Zhang